UNIVERSITY OF CALIFORNIA SAN DIEGO

Experiments on Cross-Magnetic-Field Heat Transport in Magnetized, Pure Electron Plasmas

A dissertation submitted in partial satisfaction of the
requirements for the degree
Doctor of Philosophy

in

Physics

by

Kurt Anthony Thompson

Committee in charge:

Professor C. Fred Driscoll, Chair
Professor Daniel H. E. Dubin, Co-Chair
Professor Robert E. Continetti
Professor Thomas M. O'Neil
Professor Kevin B. Quest
Professor Clifford M. Surko

2020

The dissertation of Kurt Anthony Thompson is approved, and it is acceptable in quality and form for publication on microfilm and electronically:

_____

_____

_____

_____

_____
Co-Chair

_____
Chair

University of California San Diego

2020

DEDICATION

This dissertation is dedicated to

Anita, Lance and Kyle,

for their many years of encouragement;

and to

Alyssa,

for her unwavering support

EPIGRAPH

The beginning of knowledge is the discovery of something we do not understand

— Frank Herbert

TABLE OF CONTENTS

LIST OF FIGURES

LIST OF TABLES

ACKNOWLEDGEMENTS

I would like to thank my advisors Professor Fred Driscoll and Professor Dan Dubin for their guidance and for subjecting me to a high standard of scientific research. I was truly fortunate to study under Fred and Dan who are top-class physicists and I have benefited immensely from emulating their methods and practices. Fred taught me the importance of focusing on the physics, the big questions, and to avoid getting mired in the irrelevant details. Dan has an immense knowledge of plasma physics and I greatly appreciate his excellent explanations of theory concepts and the time he took to answer my questions.

Special thanks goes to Dr. Andrey Kabantsev who educated me on the ins-and-outs of nonneutral plasmas and who patiently taught me how to conduct experiments. Dr. Francois Anderegg was a valuable resource and colleague through out my years in the Nonneutral plasma group and I greatly appreciate his assistance, expertise and willingness to help. My fellow CamV graduate student, Nicola Panzeri, provided significant contributions to my research and I enjoyed all of our discussions both inside and outside of physics. I wish to thank Professor Tom O'Neil for his incisive discussion and analysis of my research and for his insight which lead to key improvements in the temperature profile measurement technique that forms the backbone of this dissertation. I also wish to thank my fellow students for their camaraderie and collaboration; in particular I would like to thank Richard Chim, Matt Affolter, Daniel Walsh, Noah Hurst, Jacob Saret and Santino Desopo.

Outside of my research group, I wish to thank Dr. James Danielson for taking an interest in my work and for his excellent analysis and commentary regarding my research. I also wish to thank James for supplying me with a rotating wall driver after I fried my first one. I would like to thank Professor Patrick Diamond who taught nearly every classical physics and plasma physics course that I took at UCSD; I am very grateful for his commitment to education and for encouraging me when I was just starting out in plasma physics. Additionally, I greatly appreciate the time that the members of my dissertation committee have spent reviewing and editing this

dissertation.

Outside of physics, I wish to thank my family, Anita, Lance and Kyle and well as my godparents, Roger and Sherry Hitchcock, for all of their assistance over my life. Finally, I would like to thank Alyssa Quam, who agreed to join me on our crazy adventure and who inspires me every day.

This research was supported financially by the National Science Foundation Grant No PHY-1805764 and the Department of Energy Grant No. DE-SC0018236.

Chapter 3, in part, is currently being prepared for submission for publication. K. A. Thompson, A. A. Kabantsev, N. Panzeri and C. F. Driscoll. The dissertation author was the primary investigator and author of this material.

Chapter 4, in part, is currently being prepared for submission for publication. K. A. Thompson, A. A. Kabantsev, N. Panzeri and C. F. Driscoll. The dissertation author was the primary investigator and author of this material.

Chapter 5, in part, is currently being prepared for submission for publication. K. A. Thompson, A. A. Kabantsev, N. Panzeri and C. F. Driscoll. The dissertation author was the primary investigator and author of this material.

VITA

2011	B. S. Physics, B. S. Mathematics Saint Mary's College of California
2014-2016	Teaching Assistant, Department of Physics University of California San Diego
2016	M. S. in Physics, University of California San Diego
2016-2020	Research Assistant, Department of Physics University of California San Diego
2020	Ph. D. in Physics, University of California San Diego

PUBLICATIONS

K. A. Thompson, A. A. Kabantsev, N. Panzeri and C. F. Driscoll. "Measurements of Cross-Magnetic-Field Heat Transport in Pure Electron Plasmas" in preparation.

K. A. Thompson, A. A. Kabantsev, N. Panzeri and C. F. Driscoll. "Measurements of the parallel temperature profile in Nonneutral Plasmas" in preparation for *Physics of Plasmas*.

A. A. Kabantsev, K. A. Thompson and C. F. Driscoll. "First experiments with e^-/H^- plasmas: Enhanced centrifugal separation from diocotron mode damping". *Non-Neutral Plasma Physics X*. AIP Conference Proceedings **1928**, 020008 (2018).

ABSTRACT OF THE DISSERTATION

Experiments on Cross-Magnetic-Field Heat Transport in Magnetized, Pure Electron Plasmas

by

Kurt Anthony Thompson

Doctor of Philosophy in Physics

University of California San Diego, 2020

Professor C. Fred Driscoll, Chair
Professor Daniel H. E. Dubin, Co-Chair

In this dissertation we present measurements of cross-magnetic-field heat transport in pure electron plasmas confined within a cylindrical Penning-Malmberg Trap. The measured heat transport is dominated by "long-range collisions", which are not included in classical transport theory. Most significantly, long-range collisions are observed to cause heat transport which is *independent of the magnetic field*, as opposed to classical theory which scales as B^{-2}. Modern theory predicts that long-range collisions are effective up to a Debye length, and thereby predicts transport rates which agree with the present measurements to within 50%.

Experimentally, the electron plasma temperature is obtained versus radius and time by a newly-developed technique which measures the charge which escapes past controlled end-trapping barriers. We describe the technique in detail including the data collection, analysis and calibration. The method is validated via several experiments of the temporal evolution of the radial temperature profile including heating due to asymmetry-induced radial expansion, cooling due to cyclotron radiation and heating due to separatrix-crossing dissipation. The temperature diagnostic is shown to be robust and capable of obtaining spatial temperature resolution on the order of the Debye length. The technique is applicable to a variety of nonneutral plasma traps enabling temperature diagnostics for previously inaccessible experiments.

From the measured density $n(r,t)$ and temperature $T(r,t)$ data, heat transport is analyzed as diffusion due to random particle collisions, convection due to bulk plasma flow, plus source terms consisting of Joule heating and cyclotron cooling. From these experiments we determine the cross-field thermal diffusivity, which we measure over a range of axial magnetic fields from $1 < B < 13$ kG; the measured diffusivity is compared with the predictions from the classical and modern transport theories. Classical theory considers collisions with collision impact parameters up to the cyclotron radius whereas modern theory considers long-range collisions with impact parameters up to the Debye length. Over the range of magnetic fields studied, the predicted transport rates from the modern theory are $10^3 - 10^5$ times larger than transport rates predicted by classical theory. The measured diffusivity is within 50% agreement with the modern theory prediction and the measurements verify the magnetic-field-independence of the heat transport.

Chapter 1

Introduction and Summary

1.1 Collisional Transport in Nonneutral Plasmas

Transport in plasma is one of the most widely studied topics within plasma physics and has important applications in many fields such as low-temperature, fusion, and astrophysical plasmas [1, 2, 3, 4]. Specifically, heat transport has garnered much attention since a clear understanding of heat transport is necessary for the development of a functioning fusion reactor [5, 6, 7, 8].

In general, transport in plasmas can be grouped into two categories: turbulent and collisional transport. Turbulent transport arises from fluctuations due to microinstabilites and unstable collective modes. Neutral plasmas, especially fusion plasmas, are often dominated by turbulent transport because of the numerous instabilities that exist for these plasmas [9]. Collisional transport on the other hand is driven by random fluctuations due to inter-particle collisions. In this dissertation we will be concerned with collisional heat transport arising from inter-particle collisions rather than heat transport arising from turbulence. Nonneutral plasmas are excellent candidates for studies of collisional transport because these plasmas can be confined in a quiescent stable state with minimal turbulence so that inter-particle collisions are the dominant transport mechanism.

Research regarding collisional transport properties in nonneutral plasmas has been very successful over the past 30 years. Nonneutral plasmas are typically confined in a cylindrical Penning-Malmberg trap where radial confinement is provided by an axial magnetic field and axial confinement is created by electrostatic confinement barriers. Due to their excellent confinement properties, nonneutral plasmas can rapidly relax to a state of local thermal equilibrium. When the confinement is exceptional, internal interations cause the plasma to relax to a rotating global thermal equilibrium state [10]. Plasma parameters, such as density and temperature, are controlled with great precision and measured using incisive diagnostics which enables detailed studies of collisional transport in nonneutral plasmas.

The earliest experiments in nonneutral plasma transport were measurements of the confinement time which is limited by interactions with the external (non-rotating) world. In these early experiments, the confinement time was short due to rapid radial expansion of the plasma which was caused by external interactions such as collisions with background gas and asymmetry-induced transport. Collisional transport measurements could not be performed on these poorly confined plasmas since inter-particle transport was dominated by externally-induced transport. Experiments showed that at high neutral background pressures ($P_{bg} > 10^{-5}$ torr), the confinement time was proportional to the neutral background pressure and therefore longer confinement times could be achieved by improving the vacuum conditions [11]. With the introduction of ultra-high vacuum environments ($P_{bg} \sim 10^{-10}$ torr) the confinement time was found to increase as the background pressure decreased; but eventually the confinement time would "plateau" and further reduction of the neutral background pressure would not yield better confinement [12, 13, 14]. It was concluded that the confinement time was being limited by electrostatic and magnetic trap asymmetries that torque on the plasma, causing it to expand radially and be lost to the cylindrical wall. Despite the inability to improve confinement with improved vacuum, the confinement times that were achieved were sufficiently long so that inter-particle collisions could achieve local thermal equilibrium along each field line; and in some cases where the confinement was

exceptional, global thermal equilibrium could be achieved.

With the ability to trap nonneutral plasmas for long times such that the plasma achieves a stable quiescent state, the experiments reached a level of sophistication where incisive experiments could be performed to measure fundamental collisional transport coefficients: particle diffusion, viscosity and thermal conductivity. A close collaboration between theoretical and experimental research discovered and studied the importance of long-range collisions in the transport properties of nonneutral plasmas [15].

Classically, transport coefficients are calculated by considering "short-range" collisions with impact parameter ρ between the distance of closest approach and the cyclotron radius, that is $b < \rho < r_c$. Classical collisions predominate when $\lambda_D < r_c$ which is typical for many laboratory plasmas, with nonneutral plasmas being a notable exception. In contrast, nonnenutral plasmas require $r_c < \lambda_D$, in which case "long-range" collisions up to the Debye length can occur, $r_c < \rho < \lambda_D$, with surprising implications for collisional transport processes, e.g. collisional heat transport due to long-range collisions is independent of magnetic field. The extensive research in long-range collisional transport, as shown in Table (1.1), has demonstrated that transport due to long-range collisions can be many orders of magnitudes larger than transport due to classical short-range collisions, when $r_c < \lambda_D$.

Furthermore, theory and experiments have discovered the enhancement of particle diffusion and viscosity in the "2D bounce-average" regime also called the "high-rigidity" regime. Here, the rigidity is defined as, $\mathcal{R} = f_b/f_E$, where the axial bounce frequency f_b is the rate at which particles oscillate axially along the trap axis, and the $E \times B$ drift frequency f_E is the rate at which particles orbit around the trap axis. When $\mathcal{R} \gg 1$, particles can undergo multiple correlated axial collisions before being sheared away from each other due to θ-rotation. The multiple correlation collisions strongly enhance the particle diffusion and viscosity; the experiments and theory regarding the enhancement is summarized in Table (1.1).

Table 1.1: Transport Coefficients for three regimes; classical collisions, 3D long-range collisions and 2D long-range collisions. Based on table from Reference [15].

$\nu_c = n\bar{v}b^2$	Diffusion D	Kinetic Viscosity η/nm	Thermal Diffusivity $\chi = 2\kappa/5n$
$\rho < r_c$ Classical Short-Range Collisions	$\frac{4\sqrt{\pi}}{3}\nu_c r_c^2 ln\left(\frac{r_c}{b}\right)$ Longmire & Rosenbluth [16]	$\frac{2\sqrt{\pi}}{5}\nu_c r_c^2 ln\left(\frac{r_c}{b}\right)$ Longmire & Rosenbluth [16] Simon [18]	$\frac{16}{15}\sqrt{\pi}\nu_c r_c^2 ln\left(\frac{r_c}{b}\right)$ Rosenbluth & Kaufman [17]
$\rho > r_c$ 3D Long-Range Collisions $\mathcal{R} \lesssim 1$	$2\alpha\sqrt{\pi}\nu_c r_c^2 ln\left(\frac{\bar{v}}{\Delta v_m}\right) ln\left(\frac{\lambda_D}{r_c}\right)$ (Lifshitz & Pitaevskii [19]) O'Neil [20], Dubin [22] Anderegg [25]	$0.59\alpha\nu_c\lambda_D^2 ln\left(\frac{\bar{v}}{\Delta v_m}\right)$ (+ wave) O'Neil [20] Dubin & O'Neil [23] Driscoll [10]	$.49\nu_c\lambda_D^2$ (+ wave) (Rosenbluth & Liu [21]) Dubin & O'Neil [24] Hollmann [26, 27]
2D z-averaged Long-Range Collisions $\mathcal{R} \gg 1$	$8\pi^2\frac{f_b}{r\lvert w_E'\rvert}\nu_c r_c^2 ln\left(\frac{r}{d}\right)$ Dubin & Jin [28] Anderegg [30]	$16\pi^2\frac{f_b}{rw_E'}\nu_c d^2 g(2d/r)$ Dubin & O'Neil [29] Kriesel [31]	Theory Not Applicable

1.2 Heat Transport in Pure Electron Plasmas

In this dissertation we present the first measurements of cross-magnetic-heat transport in a pure electron plasma and thereby add to the body of experimental research regarding collisional transport in nonneutral plasmas that was presented in the previous section. Our heat transport measurements are made possible by the development of a new technique for measuring the radial profile of the parallel temperature of a nonneutral plasma. The new temperature measurement technique enables unprecedented accuracy and spatial resolution for radial temperature profile measurements of electron plasmas. The technique is shown to be robust and gives spatial resolution on the order of the Debye length. With this new temperature measurement technique we have done a systematic study of heat transport in pure electron plasmas for a large range of magnetic fields.

Prior to the research presented in this thesis, heat transport measurements in nonneutral plasma had been performed on $^{24}Mg^{+}$ plasmas. Heat transport experiments could be performed on $^{24}Mg^{+}$ because the velocity-space distribution function (and hence the temperature for Maxwellian distributions) can be diagnosed using laser-induced flourescence techniques [26, 32]. In the $^{24}Mg^{+}$ experiments, heat transport was characterized by measuring the thermal diffusivity and measurements were performed for a range of parameters include a factor of 4 change in the magnetic field, 10^3 change in the temperature and factor of 50 change in density. All of the experiments with ion plasmas were performed in the low rigidity regime, $\mathcal{R} < 1$.

In pure electron plasmas, the separation between classical thermal diffusivity and long-range thermal diffusivity is ~ 1000 times larger than ion plasmas as seen in Table (1.2). Therefore, heat transport in pure electron plasmas is expected to be completely dominated by long-range collisions. Our measurements over a range of magnetic fields from $1 < B_z < 13$ kG are in good (50%) agreement with the prediction from long-range collisions and our results demonstrate the magnetic-field-independence of the thermal diffusivity. Furthermore, we perform measurements

Table 1.2: Comparison between ion and electron heat transport experiments in nonneutral plasmas.

Parameter	Previous Study on $^{24}Mg^{+}$ Ion Plasma	Current Study on Electron Plasma
λ_D/r_c	~ 10	$\sim 10^3$
χ_L/χ_C	~ 100	$\sim 10^5$
$\mathcal{R} = f_b/f_E$	~ 1	~ 60

of the thermal diffusivity over a range of plasma rigidities, $1 < \mathcal{R} < 60$, which are the first measurements of heat transport in the highly rigid regime. We observe that the thermal diffusivity does not depend on the plasma rigidity which is consistent with the theoretical perspective.

Chapter 2

Background

2.1 Introduction

Nonneutral plasmas are routinely confined in a Penning trap or Penning-Malmberg trap where radial confinement is provided by an externally-applied axial magnetic field and axial confinement is achieved through electrostatic potentials applied to a set of cylindrical electrodes. The cylindrical symmetry of the confinement geometry guarantees that the canonical angular momentum is a constant of the motion, which in turn places a constraint on the radial positions of the particles by requiring that the mean-squared radius of the plasma be conserved [33]. The constraint on the mean-squared radius is an important confinement property that enables the long-time confinement of a nonneutral plasma and the achievement of thermal equilibrium.

The excellent confinement properties of nonneutral plasmas have allowed for detailed studies of cross-field transport [25, 26, 31], wave-particle interactions [34, 35], vortex dynamics [36, 37, 38] and antimatter properties [39, 40]. In this chapter we provide a brief discussion of the confinement proprieties of electron plasmas in Penning-Malmberg traps and we specify the plasma parameters and geometry of the electron plasmas studied in this dissertation.

2.2 Experimental Device - CamV

Experiments are performed on an electron plasma confined in a Penning-Malmberg trap called, "CamV", which is shown schematically in Fig. 2.1. The trap consists of an array of hollow concentric cylindrical electrodes that are enclosed within a cylindrical vacuum vessel. Ultra-high vacuum is maintained using an ion pump and the neutral background gas pressure is typically $P_{bg} < 10^{-10}$ torr. The electrodes are made of oxygen-free high-thermal-conductivity copper and are electroplated with a layer of gold to prevent oxidation and reduce undesirable electrostatic patch effects that degrade plasma confinement.

Surrounding the vacuum vessel is a superconducting electromagnet that creates a uniform axial magnetic field, $\mathbf{B} = B_z\hat{z}$, along the electrode axis. The maximum magnetic field that can be achieved is $B_z \approx 16$ kG and experiments are performed in the range $1 < B_z < 13$ kG. Saddle coils are used to apply small correction magnetic fields in the perpendicular directions, B_x and B_y, so that the axial magnetic field is precisely aligned with the electrode axis. The magnetic field provides radial confinement of the electrons by inducing an $E \times B$ drift of the electrons around the center of charge which is nominally aligned with the electrode axis when the plasma is quiescent.

The electrons are confined axially by negative potentials, $V_c = -100$ V, that are applied to two of the electrodes which are referred to as the confinement electrodes. The upstream confinement electrode is referred to as the inject electrode and the downstream confinement electrode is referred to as the eject electrode. In the configuration shown in Fig 2.1, electrode 1 is the inject electrode and electrode 10 is the eject electrode. The cylindrical geometry of the electrodes necessitates the use of a cylindrical coordinate system (r, θ, z) which we use throughout this dissertation.

Electrons are produced from a heated spiral tungsten filament that is negatively biased to accelerate electrons into the trap. The filament has an outer radius of $R_f = 1.8$ cm and is heated with an alternating current $I_f = 15.5$ Amps (pk) with a voltage of $V_f = 11.3$ Volts (pk) giving

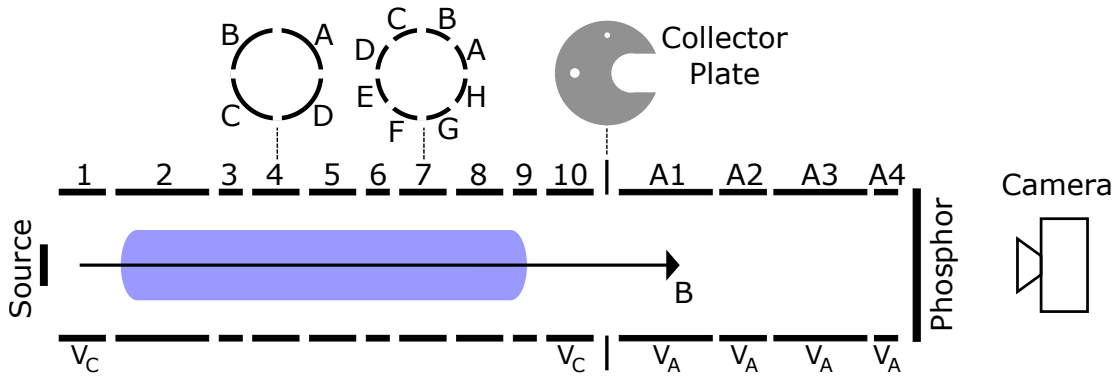

Figure 2.1: Schematic of the experiment. In this configuration, the confinement voltages are applied to electrodes 1 and 10. Electrodes 2-9 are grounded and a positive potential V_A is applied to electrodes A1-A4 to accelerate electrons towards the phosphor screen which is biased to +15 kV. Electrodes 4 and 7 are divided into electrically-isolated azimuthal sectors and are used to apply asymmetric perturbations.

a power of $P \approx 180$ Watts (pk). The bias voltage is typically set to $V_b = -30$ V and is chosen to match the on-axis plasma potential produced by the unneutralized plasma [41]. The voltage across the spiral filament is then given by

$$V(r) = V_b + V_f \frac{r^2}{R_f^2} \tag{2.1}$$

which matches the radial potential profile of an idealized cylindrical column with constant density.

Normally, the filament can be heated using a direct current power source. However, because the filament in CamV is located in the high-field region of the trap, the resulting stress from the $\mathbf{I} \times \mathbf{B}$ force would cause a distortion of the filament and possible damage over long periods of usage [42]. Therefore, instead of direct current we use a 16.25 kHz alternating current so that the net force applied to the filament is zero when averaged over a cycle.

The device is operated in an inject-hold-eject cycle. To inject electrons into the trapping region, the voltage of the inject electrode is ramped to ground and held for $\sim 100\ \mu s$, allowing the electrons from the filament to stream into the trap. The electrons are trapped by ramping the inject electrode back to V_c. During the injection period, the power amplifier controlling the filament current is triggered to briefly hold the filament current at a predetermined fixed level, so

that the potential profile across the filament is given by Eq. (2.1).

The axial distance between the two confinement electrodes defines the confinement length L_c. By appropriate choice of electrodes we can vary the confinement length from $7 \leq L_c \leq 52.5$ cm. The actual length L_p of the plasma column is less than L_c with L_p 3-5 cm shorter than L_c (see Sec. 2.4). The inner wall radius $R_w = 3.5$ cm, defines the maximum radial extent of any plasma but radial loss to the wall is negligible in all experiments described here.

Once the electrons are trapped, selected electrodes can be used to monitor/excite wave activity and apply perturbations to the plasma. Two of the electrodes are divided azimuthally into electrically isolated sectors that can be individually biased to apply azimuthally dependent perturbations or excitations. Electrode 4 is divided into 4 azimuthal sectors that have arc sizes of 60° and the sectors are separated by 30° sections of the frame of electrode 4. Electrode 7 is divided into 8 azimuthal sectors that have arc sizes of 25° and the sectors are separated by 20° sections of the frame of electrode 7. Electrodes 4 and 7 are routinely used to excited low frequency drift modes known as Diocotron modes and high frequency Trivelpiece-Gould modes which are standing Langmuir waves for the finite cylindrical geometry of the plasma column [43, 44, 45, 46].

After a confinement time, t_c, the plasma density profile is destructively measured by ejecting the plasma onto a phosphor screen by ramping the eject electrode to ground. Typically, a positive accelerating voltage, $50 \leq V_A \leq 100$ V, is applied to electrodes A1-A4 to accelerate the ejected electrons towards the phosphor screen, which is further biased to $+15$ kV. Since the plasma column is destructively measured during the ejection process, to obtain the time evolution of the dynamics we are required to reproduce the exact initial conditions over many hundreds of experiments cycles. We typically find that the shot-to-shot reproducibilty is $\delta n/n < 1\%$ at low magnetic fields, $B_z < 2$ kG, and varies in the range of $3 < \delta n/n < 5\%$ at higher magnetic fields, $B_z > 2$ kG. The difference in the shot-to-shot reproducibility at high magnetic field versus low magnetic fields is not entirely understood, but is attributed to the small $E \times B$ rotation

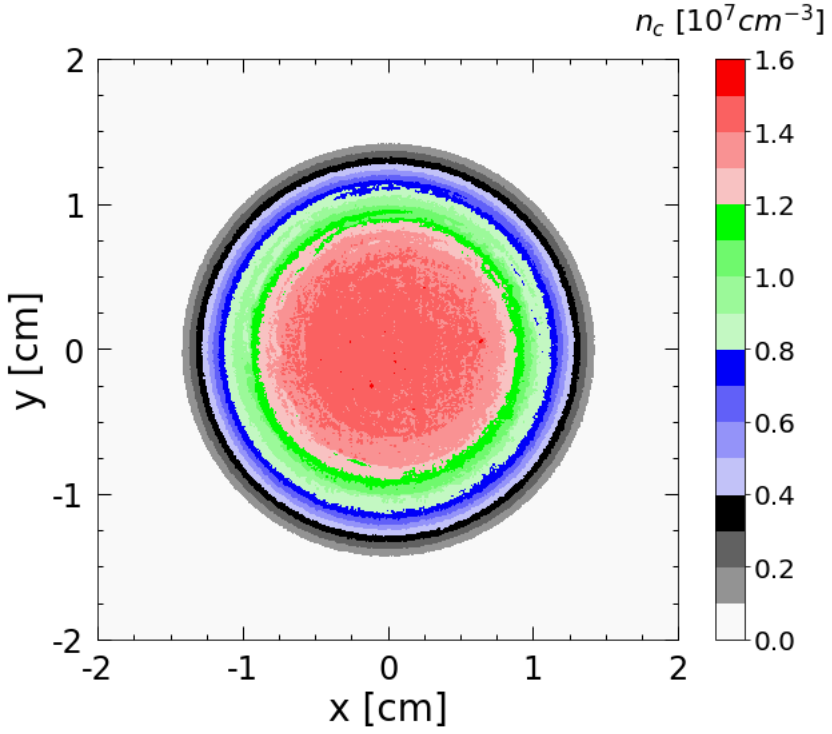

Figure 2.2: CCD camera image of a typical electron plasma.

frequency at high magnetic field, as well as variations in the turbulent decay of the injected plasma profile. Various techniques can be used to shape the plasma profile and improve the shot-to-shot reproducibility.

2.3 Destructive Diagnostics

The primary diagnostic on CamV is a destructive measurement of the z-integrated density profile of the plasma column. When the plasma is ejected from the trap and impacts the phosphor screen, the resulting flourescent light from the phosphor is imaged by a charge-coupled device (CCD) camera that has 1024×1024 pixels. The flourescence is proportional to the number of electrons that impact the phosphor screen, and calibration of a full ejection determines the z-integrated plasma density,

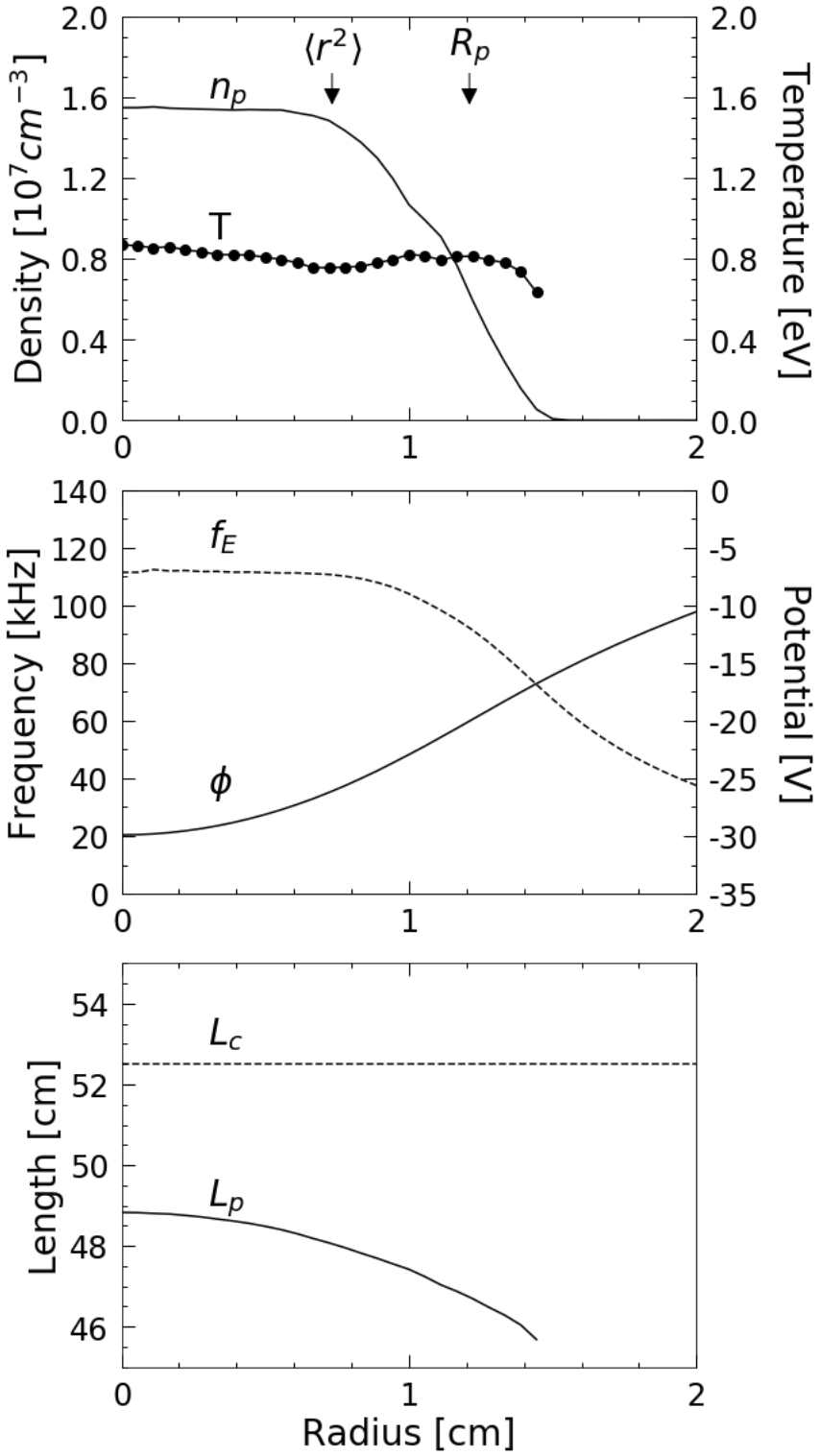

Figure 2.3: Typial radial profiles of the density, temperature, potential, $E \times B$ rotation frequency and plasma length at a magnetic field of $B_z = 2$ kG

$$Q_2(r,\theta) = \int dz\, n(r,\theta,z) \tag{2.2}$$

where $n(r,\theta,z)$ is the volume density of electrons before the ejection process commenced. In many cases we can assume azimuthal symmetry of the plasma column around its center of charge and therefore we average over θ to obtain the θ-averaged z-integrated density $Q(r)$

$$Q(r) \equiv \langle Q(r,\theta)\rangle_\theta \equiv \frac{1}{2\pi}\int_0^{2\pi} d\theta\; Q_2(r,\theta). \tag{2.3}$$

The total number of particles, N, is calculated by a radial integral of $Q(r)$,

$$N = 2\pi \int r dr Q(r) \tag{2.4}$$

The fundamental measured quantity, $Q(r)$, is an area density but in plasma physics it is more useful and intuitive to consider the volume density, $n(r,z)$. Here, $n(r,z)$ is the volume density of the plasma in the confinement region before it was dumped on to the phosphor screen. The most accurate method to obtain the volume density is to numerically calculate an (r,z) equilibrium solution to the Poisson equation, with the electron density at each radius given by the Boltzmann relation (Sec. (2.6)). From the equilibrium solution we obtain the spatial dependence of $n(r,z)$ and we obtain more general characteristics of the shape of the plasma column such as the amount of curvature of the axial ends of the plasma column. In addition, the equilibrium solver is used to calculate the effective length of the plasma, $L_p(r)$, which varies as a function of radius due to the curvature of the column ends (The definition of $L_p(r)$ is given in Sec.(2.4)).

In this dissertation, when studying heat and particle transport, we will only be concerned with radial transport and therefore it is beneficial to remove the z-dependence of the density by defining an averaged volume density, n_p, referred to as the plasma density and is given by

$$n_p(r) = \frac{Q(r)}{L_p(r)} \tag{2.5}$$

Calculating the plasma density in this manner requires an (r,z) Poisson solution to determine $L_p(r)$, which is time consuming and not necessary when the axial dependence of the plasma is irrelevant. A zeroth-order estimate of the plasma length ignoring radial dependence often suffices, so we approximate $L_p^* = L_c - 4.5$ cm where L_p^* is the estimated length. The volume density defined using this estimate for the plasma length is referred to as the confinement density, n_c, and is calculated as

$$n_c(r) = \frac{Q(r)}{L_p^*} \tag{2.6}$$

For the long plasma studied in this dissertation the difference between n_c and n_p is less than 5% so that n_c gives a good estimate for the plasma density.

For calibration, direct measurement of the ejected charge can be obtained by rotating the collector plate to collect all of the ejected electrons (See Fig. 2.1). A charge collection circuit is connected to the collector plate as shown schematically in Fig. 2.4. To accelerate the electrons to the collector plate, the plate is biased with a positive voltage $V_A = +100$ V. The collected electrons accumulate on capacitor, C, and then decay through resistor, R, with a time constant τ_{RC}. The time constant is chosen to be long compared to the time required to eject the plasma but short compared to an experimental cycle. The voltage signal $V_c(t)$ signal developed across C is amplified and recorded by a digitizer. A DC blocking capacitor, C_b, is inserted between the charge collector capacitor and the amplifier to protect the amplifier from V_A and remove DC offset. With a fast ejection, $V_c(t)$ gives the total number of particles N which is used to calibrate the phosphor/CCD diagnostic. With a slow ejection, the first electrons escaping at $r = 0$ give an estimate of the on-axis parallel temperature $T_\parallel$.

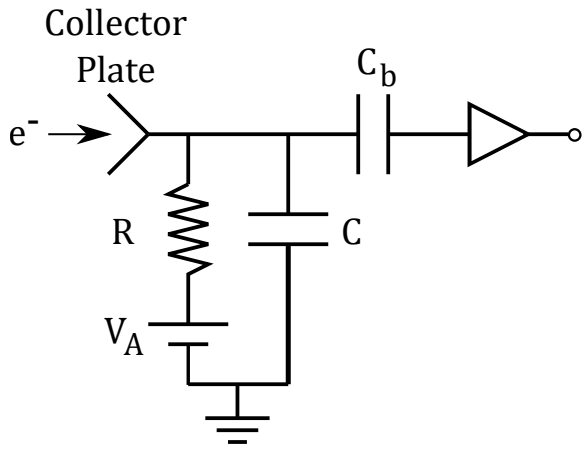

Figure 2.4: Schematic of the charge collection circuit used with the collector plate. The electrons are collected on capacitor C and the charge on the capacitor decays through resistor R. The voltage across C is amplified and recorded by a digitizer.

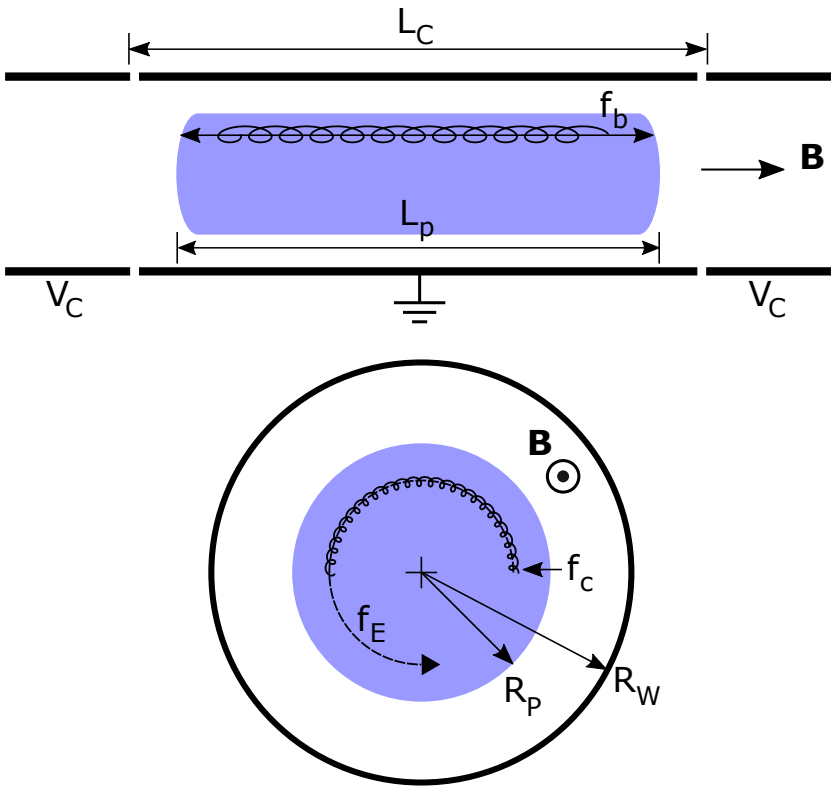

Figure 2.5: Single particle motion in a Penning-Malmberg trap. Showing the cyclotron motion with frequency f_c, the bounce motion with frequency f_b, and the $E \times B$ drift rotation at frequency f_E.

2.4 Length Scales

Several lengths scales characterize the dynamics of electrons in Penning-Malmberg traps. The smallest length scale is the distance of closest approach

$$\begin{aligned} b &= \frac{e^2}{T} \\ &\approx (1.44\ \text{nm})\left(\frac{T}{1\text{eV}}\right)^{-1} \end{aligned} \tag{2.7}$$

Due to the axial magnetic field, electrons execute, with perpendicular velocity $v_\perp$, cyclotron orbits around their guiding centers with a cyclotron radius given by

$$\begin{aligned} r_c = \frac{v_\perp}{w_c} &= \frac{m_e c v_\perp}{eB_z} \\ &\approx (23.8\ \mu\text{m})\left(\frac{T}{1\ \text{eV}}\right)^{1/2}\left(\frac{B_z}{1\ \text{kG}}\right)^{-1} \end{aligned} \tag{2.8}$$

Due to the small cyclotron radius, the (r,θ) dynamics of a nonneutral plasma can often be described using guiding-center drift theory.

The next length scale is the Debye length given by

$$\begin{aligned} \lambda_D &= \sqrt{\frac{T}{4\pi n e^2}} \\ &\approx (0.235\ \text{cm})\left(\frac{T}{1\ \text{eV}}\right)^{1/2}\left(\frac{n}{10^7\ \text{cm}^{-3}}\right)^{-1/2} \end{aligned} \tag{2.9}$$

where T is the temperature. The Debye length sets the typical distance over which particles respond to shield potential perturbations.

The next set of lengths are associated with the spatial geometry of the plasma columns which is inherited from the cylindrical confinement geometry. The mean-square radius of the plasma is calculated as

$$\langle r^2 \rangle = \frac{\int r dr\, r^2 dr Q(r)}{\int r dr\, Q(r)} \tag{2.10}$$

The mean-square radius is a useful measurement due to its proportional relationship to the canonical angular momentum. Changes in the measured $\langle r^2 \rangle$ give a direct measurement of changes in the canonical angular momentum. Therefore the time rate of change of $\langle r^2 \rangle$ is useful as a measurement of the strength of the torque applied to the plasma due to perturbations or trap asymmetries.

The next two lengths are not uniquely defined within the nonneutral plasma community. Several definitions exist for the length of the plasma and several definitions exist for the plasma radius. We derive our definition of the plasma radius, R_p, from the definition of $\langle r^2 \rangle$ by considering a "top-hat" density profile where the density is a step function with $n(r) = n_0$ for $r \leq R_p$ and $n(r) = 0$ for $r > R_p$. Top-hat profiles are theoretical idealizations of the experimental density profile which always has a radial density gradient. Calculating $\langle r^2 \rangle$ for the top-hat profile gives $\langle r^2 \rangle = R_p^2/2$. We therefore define the plasma radius as

$$R_p = \sqrt{2\langle r^2 \rangle} \tag{2.11}$$

where $\langle r^2 \rangle$ can be calculated for any density profile. R_p is used sparringly in this dissertation since $\langle r^2 \rangle$ is a more fundamental quantity given its proportional relationship with the canonical angular momentum. However, R_p gives an intuitive measurement of the radial edge of the plasma column which is useful when comparing the radial extent of the plasma to R_w.

The length of the plasma is a more difficult quantity to define, in part because the definitions depends on the importance of the (r,z) variation of the potentials at the axial ends of

the plasma near the confinement electrodes. Furthermore, the length of the plasma varies radially where the end shape of the plasma column is typically convex with an approximately parabolic dependence on the radius [47]. Due to Debye shielding, the potential at any given radius within the plasma column is uniform along the axis except in Debye sheath regions at the ends of the plasma where the confinement electrodes create electrostatic barriers that reflect the electrons back towards the center of the confinement region. In the Debye sheath regions, the potential rises rapidly with a scale length of λ_D.

The axial position at which any given electron is reflected depends on the maximal axial velocity v_{z0} of the electron. By v_{z0} we mean the velocity of the electron when it is near the axial center of the plasma, where the confinement potential is minimal and axially relatively constant. The electron velocity decreases as the electron approaches the confinement potential barriers until ultimately the electron is stopped, changes direction and then is accelerated back into the containment region. Electrons with larger v_{z0} will travel closer to the confinement electrodes before being turned around than electrons with lower v_{z0}. The difference in the length traversed by electrons with different v_{z0} depends on the size of the Debye sheath region which is a few λ_D in extent. For a long plasma or a cold plasma, λ_D is much less than the length of the plasma and therefore we can reasonably neglect the difference in length for electrons with different v_{z0}.

For a velocity-independent definition of plasma length, L_p, we use a density weighted average given by

$$L_p(r) = \frac{\left[\int dz\, n(r,z)\right]^2}{\int dz\, \left[n(r,z)\right]^2} \tag{2.12}$$

where $n(r,z)$ is the volume density that is determined from the measured $Q(r)$ profiles by solving an equilibrium solution to the Poisson equation which will be presented in Sec. 2.6. Eq. (2.12) ignores any single particle behavior in favor of an averaging that is achieved using $n(r,z)$ and is a useful representation for the plasma length when $\lambda_D \ll L_p$.

With the length definitions presented in this section, we can present the typical length scale ordering for a nonneutral plasma confined in a Penning-Malmberg trap as

$$r_c \ll \lambda_D < R_p < L_p \tag{2.13}$$

2.5 Rates

In this section we discuss the various rates relevant to nonneutral plasmas which include basic collision rates as well as frequencies of the electron drift and bounce dynamics. The fastest frequency consists of the cyclotron frequency, f_c, given by

$$\begin{aligned} f_c = \frac{\omega_c}{2\pi} &= \frac{1}{2\pi}\frac{eB_z}{m_e c} \\ &\approx (2.80\times 10^9\ \mathrm{s}^{-1})\left(\frac{B_z}{1\ \mathrm{kG}}\right) \end{aligned} \tag{2.14}$$

Along the magnetic field, electrons rapidly relax to a Maxwellian energy distribution due to collisions. The electron-electron collision rate for 90° velocity-scattering collisions is given by

$$\begin{aligned} \nu_{ee} &= \frac{16\sqrt{\pi}}{15} n\bar{v} b^2 \ln\left(\frac{r_c}{b}\right) \\ &\approx (160\ \mathrm{s}^{-1})\left(\frac{n}{10^7\ \mathrm{cm}^{-3}}\right)\left(\frac{T}{1\ \mathrm{eV}}\right)^{-3/2} \\ &\quad \times\left(1+0.10\ln\left[\left(\frac{T}{1\ \mathrm{eV}}\right)^{3/2}\left(\frac{B_z}{1\ \mathrm{kG}}\right)^{-1}\right]\right) \end{aligned} \tag{2.15}$$

where $\bar{v} = \sqrt{T/m_e}$ is the thermal velocity. The Coulomb logarithm, $\ln(r_c/b)$, assumes that the maximum impact parameter ρ for velocity-scattering (Boltzmann) collisions is r_c [48, 49]. For un-magnetized plasmas, this maximum impact parameter is $\rho \sim \lambda_D$.

Since $f_c \gg \nu_{ee}$, at any given radius the plasma can have a temperature anisotrophy between the perpendicular temperature $T_\perp$, characterizing the degrees of freedom perpendicular to the magnetic field, and the parallel temperature $T_\parallel$, characterizing the axial degrees of freedom. When there are no external sources or sinks of thermal energy, we can express the time evolution of weak anisotrophy, $T_\parallel - T_\perp$, as [50]

$$\frac{d(T_\parallel - T_\perp)}{dt} = -3\nu_{\perp\parallel}(T_\parallel - T_\perp) \tag{2.16}$$

Where $\nu_{\perp\parallel}$ is the perpendicular-parallel collision rate given by

$$\nu_{\perp\parallel} = \frac{3}{2}\nu_{ee} \tag{2.17}$$

Collisions with impact parameters $\rho < r_c$, will cause $T_\perp$ and $T_\parallel$ to relax to an equilibrium temperature T which is given by

$$T = \frac{1}{3}T_\parallel + \frac{2}{3}T_\perp \tag{2.18}$$

The factor of 2 in front of $T_\perp$ arises from the two degrees of freedom associated with the perpendicular motion. For time scales long compared to $\nu_{\perp\parallel}^{-1}$ we can assume that $T_\perp = T_\parallel = T$, and use T as the temperature variable.

Cyclotron radiation is the dominant cooling mechanism for electrons in strong magnetic fields. Here the energy of the plasma is emitted as electromagnetic radiation due to the cyclotron motion of the electron around its guiding center [51, 52]. At high magnetic fields, typically $B_z > 5$ kG, cyclotron radiation is significant and can rapidly bring the electrons into temperature equilibrium with the electrode walls. The cyclotron radiation time, τ_r, for electrons is given by

$$\begin{aligned} \tau_r &= \frac{9m_e c^3}{8e^2\omega_c^2} \\ &\approx (380\text{ s})\left(\frac{B_z}{1\text{ kG}}\right)^{-2} \end{aligned} \tag{2.19}$$

where $\omega_c = 2\pi f_c$ is the cyclotron frequency. Cyclotron radiation reduces only the perpendicular energy of the particle; however, for the plasmas studied in this dissertation, the parallel equilibriation time is short compared to the cyclotron cooling rate, i.e. $\nu_{\perp\|}^{-1} \ll \tau_r$, so that $T_\perp = T_\| = T$ is maintained. The temperature of the plasma then decays exponentially as

$$\frac{dT}{dt} = \frac{-T}{\tau_r} \tag{2.20}$$

In the axial direction the electrons bounce between the two confinement potentials. The frequency at which any given electron executes this oscillatory motion depends on the axial velocity of the electron as well as the distance between the turning points for that electron. A representative frequency for this motion is given by the oscillation of a thermal electron

$$\begin{aligned} f_b(r) &= \frac{\overline{v}}{2L_p(r)} \\ &\approx (2.10\times 10^6\text{ s}^{-1})\left(\frac{T(r)}{1\text{ eV}}\right)\left(\frac{L_p(r)}{10\text{ cm}}\right)^{-1} \end{aligned} \tag{2.21}$$

The unneutralized space charge of a nonneutral plasma creates a radial electric field E_r that causes the plasma columns to execute an $E\times B$ drift rotation around its center of charge. The frequency at which this motions occurs is the $E\times B$ rotation frequency given by

$$f_E(r) = -\frac{c}{2\pi r B_z} E_r \approx (1.44\times 10^5\ \mathrm{s}^{-1})\left(\frac{n}{10^7 \mathrm{cm}^{-3}}\right)\left(\frac{B_z}{1\ \mathrm{kG}}\right)^{-1} \tag{2.22}$$

In deriving this equation for f_E we have ignored the axial dependence of the potentials, and in calculating the numerical approximation in the second line we have assumed a constant density (i.e. top hat profile). With these frequencies defined we can give the typical frequency ordering for electron plasmas confined in a Penning-Malmberg trap as

$$f_c \gg f_b > f_E \tag{2.23}$$

Fig. 2.5 gives a conceptual depiction of the single particle motion which is described by a fast oscillation of the electron around its cyclotron orbit while the particle bounces axially between the confinement electrodes, and finally the electron executes a slow drift motion around the center of charge of the plasma column. For a 1eV electron in a plasma with density $n = 10^7$ cm^{-3} that is immersed in a magnetic field of $B_z = 1$ kG, the ratio of the three frequencies is given by $f_c : f_b : f_E = 10000 : 10 : 1$. That is, an electron completes 1000 cyclotron orbits during one bounce orbit and completes 10 bounce orbits during one drift orbit.

There are always residual electrostatic and magnetic asymmetries that couple the rotating plasma to the external world, despite "grounding" of the electrodes and precise (10^{-4} radian) alignment of the magnetic field with the electrode axis. These asymmetries torque on the plasma, reducing the canonical angular momentum P_θ, which is given by

$$
\begin{aligned}
P_\theta &= \sum_i \left(m_e v_{\theta,i} r_i + \frac{qB_z}{2c} r_i^2 \right) \\
&\backsimeq -\left(\frac{eB_z}{2c} \right) \langle r^2 \rangle
\end{aligned}
\tag{2.24}
$$

Here $q = -e$ is the signed charge and the summation is over the N total number of electrons. For nonneutral plasmas in strong magnetic fields, the kinetic contribution to the angular momentum is small compared to the magnetic term. Neglecting the kinetic term results in a proportional relationship between P_θ and the mean-square radius of the plasma $\langle r^2 \rangle$. Therefore, changes in $\langle r^2 \rangle$ give a direct measurement of changes in P_θ. The drag torque exerted by the intrinsic static trap asymmetries causes a decrease in P_θ, an increase in $\langle r^2 \rangle$, and a radial expansion of the plasma column. The expansion rate of the plasma is characterized in terms of the mean-square radius and is given by

$$
\nu_{\langle r^2 \rangle} = \frac{1}{\langle r^2 \rangle} \frac{d\langle r^2 \rangle}{dt}
\tag{2.25}
$$

An empirical expression for the "well-tuned" expansion rate is given by [53]

$$
\nu_{\langle r^2 \rangle} = (7 \text{ s}^{-1}) \left(\frac{V_a}{1V} \right) \mathcal{R}^{-2}
\tag{2.26}
$$

where V_a is the wall potential of any intrinsic or externally applied electrostatic asymmetry and $\mathcal{R}$ is the plasma rigidity. For CamV, the strength of the intrinsic trap asymmetries has been previously estimated to be $V_a = 1$ V [54]. The plasma rigidity is a useful metric for characterizing the behavior of an electron plasma and is defined as the ratio of the bounce frequency to the rotation frequency [53]

$$\begin{aligned}\mathcal{R}(r) &= \frac{f_b}{f_E} \\ &\approx 14.6\left(\frac{B_z}{1\text{ kG}}\right)\left(\frac{T(r)}{1\text{ eV}}\right)^{1/2}\left(\frac{n(r)}{10^7\text{ cm}^{-3}}\right)^{-1}\left(\frac{L_p(r)}{10\text{ cm}}\right)^{-1}\end{aligned} \tag{2.27}$$

The empirical results given by Eq. (2.26) is valid for electron plasmas with rigidities of $1 \leq \mathcal{R} \leq 10$. For electron plasmas with rigidities of $10 \leq \mathcal{R} \leq 20$ the expansion rate decreases sharply by two orders of magnitudes. For highly rigid electron plasmas where $\mathcal{R} > 20$ the expansion rate is independent of $\mathcal{R}$. The change in the dependence of $\nu_{\langle r^2\rangle}$ on $\mathcal{R}$ over the rigidity range from $1 \leq \mathcal{R} \leq 100$ is not understood and remains an open question.

2.6 Local Thermal Equilibrium

Velocity-scattering collisions between electrons at each radius cause the plasma to relax to a Maxwellian distribution function at each radial position where the distribution function is given by

$$f(r,z,v_z) = n_0(r)\left(\frac{m_e}{2\pi T(r)}\right)^{1/2} exp\left(-\frac{\frac{1}{2}m_e v_z^2 + q\phi}{T(r)}\right) \tag{2.28}$$

where $n_0(r)$ is a normalization factor. Integration of the distribution function over the axial velocity gives the Boltzmann equation for the axial density dependence

$$n(r,z) = n_0(r) exp\left(-\frac{q\phi}{T(r)}\right) \tag{2.29}$$

To calculate the potential we use the Poisson equation with appropriate boundary conditions

$$\nabla^2\phi(r,z) = -4\pi q n(r,z) \tag{2.30}$$

where the boundary conditions are

$$\frac{d\phi}{dz} = 0 \qquad (r, z = z_{ends}) \tag{2.31}$$

$$\frac{d\phi}{dr} = 0 \qquad (r = 0, z) \tag{2.32}$$

where z_{ends} are the axial boundaries of the numerical grid and the potential is specified at the wall radius which is zero throughout the confinement region and is V_c on the inject and eject electrodes.

We routinely calculate numerical solutions to the Boltzmann-Poisson equations in order to determined the density and shape of the plasma. It is worth noting at this point that solving the Boltzmann-Poisson equations requires specification of the radial temperature profile $T(r)$ and the normalization $Q(r) = \int dz\, n(r,z)$. The normalization is easily obtained by ejecting the plasma column and measuring $Q(r)$. For the temperature, the standard temperature measurement technique utilized in the nonneutral plasma community only measures the temperature near $r = 0$ [55]. In order to use the Boltzmann-Poisson system of equations to determine the (r,z) distribution of the density, the assumption is made that the radial temperature gradient is small so that the temperature is approximately uniform and equal to the measured temperature at $r = 0$. In Chapter 3 we will develop a technique for measuring the full radial temperature profile $T(r)$ thereby improving the accuracy at which the (r,z) distribution of the density can be determined.

2.7 Adiabatic Invariants

Adiabatic invariants play an important role in plasma physics in general as well as the dynamics of nonneutral plasmas; this is especially true of the research presented in this dissertation. The preservation of adiabatic invariants places constraints on collisional transport processes as

well as constraints on the distribution function when the plasma is axially expanded or compressed. We briefly discuss three adiabatic invariants that are relevant to nonneutral plasmas.

In general, when a system has periodic motion, the action integral is a constant of the motion when the parameters of the system are varied slowly compared to the periodicity of the oscillatory motion [56]. The action integral is defined as $\oint pdq$ where q is a generalized coordinate, p is the conjugate momentum and the integral is taken over one period of the motion. The first adiabatic invariant is associated with the rapid cyclotron motion of the particles in the magnetic field

$$\mu' = \oint p_\perp ds = m_e \oint v_\perp r_c d\theta \tag{2.33}$$

where $p_\perp$ and $v_\perp$ are the momentum and velocity associated with the cyclotron motion of the particle. We define the electron magnetic moment as $\mu = m_e v_\perp^2/2B$ and we solve for μ'

$$\mu' = \frac{4\pi m_e c}{q}\mu \tag{2.34}$$

Therefore we see that preservation of the cyclotron adiabatic invariant is equivalent to preservation of the magnetic moment.

The second adiabatic invariant is the bounce adiabatic invariant which is associated with the axial oscillatory motion of the particles between the two confinement electrodes and is given by

$$J = \oint p_z dz = m_e \oint v_z dz \tag{2.35}$$

The bounce adiabatic invariant is often conserved when the voltage on the confinement electrodes are manipulated slowly compared to the bounce period of the electrons.

The third adiabatic invariant is the conservation of the magnetic flux enclosed by the guiding center drift orbit of an electron. This drift-orbit adiabatic invariant is calculated as the

cyclic integral of the angular momentum along the drift orbit

$$\Phi = \oint p_\theta ds \approx \frac{e}{c} \oint A_\theta r d\theta \tag{2.36}$$

where we have neglected the small drift velocity term in the single particle angular momentum. When the magnetic field is uniform in the plane of the drift-motion the adiabatic invariant becomes

$$\Phi = \frac{e\pi r^2 B_z}{c} \tag{2.37}$$

This adiabatic invariant is usually unimportant when the plasma is within the trapping region since, by design, Penning-Malmberg traps have uniform magnetic field in the trapping region. However, in most electron Penning-Malmberg traps the electron source is located in a low-field region and therefore the drift orbit adiabatic invariant plays a significant role when injecting the plasma into the trapping region. In CamV, the filament, confinement electrodes and phosphor screen are all located within a region of uniform magnetic field and therefore the drift orbit adiabatic invariant is irrelevant. However, it should be noted that the placement of the filament inside of the high-field region results in a lower density, $10^6 - 10^7$ cm^{-3}, than is often found in other electron plasmas confined in Penning-Malmberg traps which typically have densities in the range of $10^8 - 10^9$ cm^{-3}. In most Penning-Malmberg traps, the electron source is located in a low field region and when the electrons are injected into the trapping region they transition from the low field region to the high field region. During the injection, Φ is conserved which yields the relationship

$$r_H = r_L \sqrt{\frac{B_{z,L}}{B_{z,H}}} \tag{2.38}$$

where r_L (r_H) and $B_{z,L}$ ($B_{z,H}$) are the drift orbit radius and magnetic field in the low (high) field region. The preservation of the drift-orbit adiabatic invariant causes the radius of the drift orbit to decrease as the particle transits from the low field region to the high field region resulting in a

higher density in the trapping region. The higher density results in markedly different behavior such as increased rotation frequencies, equilibriation rates and transport properties.

2.8 Diocotron Modes

We now discuss the (r,θ) drift modes called the Diocotron modes which are ubiqutous in pure electron plasmas confined in Penning-Malmberg traps. These modes are characterized by their azimuthal mode number, m, and have no axial dependence, that is, $k_z = 0$, where k_z is the axial mode number. Diocotron modes are readily excited using sectored electrodes and the amplitudes and frequencies of the modes can be manipulated and measured while the plasma is confined. The density perturbation created by the mode are given by

$$\delta n(r,\theta) \propto A(r)\cos(m\theta - 2\pi f_m t) \tag{2.39}$$

where $A(r)$ is the radial eigenfunction and f_m is the mode frequency. In this dissertation, changes in the frequency of the $m = 1$ Diocotron mode are used to diagnose changes in the length of the plasma and changes in the temperature. For an infinite-length plasma column with a constant density profile the frequencies are given by [57]

$$f_m = \frac{nec}{B_z}\left(m - 1 + \left(\frac{R_p}{R_w}\right)^{2m}\right) \tag{2.40}$$

In reality the finite-length of the plasma column introduces shifts in the mode frequencies which are nontrivial. For the $m = 1$ mode, a detailed study of the mode frequency has been performed by Fine [58] and a more accurate equation for the mode frequency has been derived [59, 60]. The improved model for the $m = 1$ Diocotron mode includes corrections to the mode frequency due to finite-length of the plasma column as well as the effect from the image charges at the electrode wall. Notably, Fine's improved model does not include the curvature of the ends of the

plasma column and treats the columns as having flat ends. The shifts in the frequency due to the curvature of the ends of the plasma column are small and the mode frequency calculated by Fine's model agrees within 5% with the experimentally measured mode frequency. We denote the $m = 1$ Dioctron frequency as, f_d, and the finite-length representation of the frequency is given by

$$f_d = \frac{ceN_L}{\pi B_z R_w^2}\left(1 + \frac{R_w}{L_p^*}\left[\frac{j_{01}}{2}\left(\frac{1}{4} + \ln\left(\frac{R_w}{R_p}\right) + \frac{T}{e^2 N_L}\right) - 0.671\right]\right)\left\{1 + \sigma\frac{D^2}{R_w^2}\right\} \tag{2.41}$$

where $j_{01} = 2.405$ is the first zero of the J_0 Bessel function, $N_L = N/L_p^*$ is the line density and σ is a dimensionless geometric factor given by

$$\sigma = \frac{1 - 2(R_p/R_w)^2}{[1 - (R_p/R_w)^2]^2} \tag{2.42}$$

The term in braces in Eq. (2.41) is the nonlinear shift to f_d when the model amplitude D is large. For the $m = 1$ Dioctron modes utilitzed in this research, $D \ll R_w$ and the nonlinear shift is small. Note that the equation for the finite-length Diocotron mode has a temperature dependence which does not occur in the infinite-length frequency equation, Eq. (2.40).

Some of the Diocotron modes are negative energy modes which means that the dissipation of energy results in the growth of the mode [61]. A well known example is the destabilization and growth of the $m = 1$ Diocotron mode due to resistance in the confinement electrodes [62]. In our experiment, the $m = 1$ Diocotron mode is almost always excited during the injection process, so the first step in the experimental cycle is generally to damp the mode with negative feedback. That is, the mode is detected on one sector of a sectored electrode, and then an amplified signal is applied to the diametrically opposite sector, thereby resonantly damping the mode and bringing the plasma column back to a quiescent state.

Chapter 3

Measuring the Radial profile of the Parallel Temperature

3.1 Introduction

In this chapter we present a technique for measuring the radial parallel temperature profile of a nonneutral plasma. Similar to previous techniques, [55, 63, 64] we measure the number of particles that escape from the confinement region as the magnitude of the electrostatic confinement barrier is reduced by ramping the trapping potential to ground. However, we specifically require that the trapping potential be varied slowly compared to the axial bounce frequency of the particles, thereby preserving the bounce adiabatic invariant. The distribution function of the still-confined particles can then be modeled as a truncated Maxwellian, with an effective temperature determined by preservation of the bounce adiabatic invariant. With this distribution function, we are able to accurately calculate the plasma potential to enable quantitative interpretation of the escaped charge data. Use of this model differentiates the temperature measurement technique discussed in this paper from previous techniques, and the model enables accurate predictions of the number of escaping particles at all trapping potentials as well as accurate temperature profiles

with spatial resolution on the order of the Debye length.

A perpetual challenge in the study of nonneutral plasmas has been accurate measurement of the plasma temperature and, more difficult still, measurement of the temperature as a function of radius in the case of a nonuniform temperature profile. Techniques utilized in the study of neutral plasmas are unfeasible for nonneutral plasmas; the requirement of cylindrical symmetry precludes the insertion of Langmuir probes and the low density ($\sim 10^6 - 10^9$ cm^{-3}) prevents the use of optical techniques such as Thomson scattering. For a select subset of nonneutral plasmas consisting of ions, notably $^{24}Mg^+$ and $^9Be^+$, the velocity distribution function, and hence the temperature, can be diagnosed using laser-induced fluorescence [32, 65]. However, laser-induced fluorescence techniques are not applicable to electron, positron or antiproton plasmas which are areas of considerable research efforts. The temperature measurement technique discussed in this Chapter is intended for use with nonneutral plasma species that are not amenable to measurement with laser-induced florescence.

For plasmas where laser-induced flourescence techniques are not available, the most commonly used temperature measurement method is to ramp down the magnitude of the electrostatic confinement barrier and measure the number of particles that initially escape from the radial center of the trap [55]. The distribution function is assumed to be Maxwellian, and the temperature is determined from an exponential fit to the number of escaping particles as a function of the confinement barrier magnitude. Since the temperature is only measured at the radial center of the plasma, this method is necessarily used in tandem with the assumption that the temperature profile is uniform or that radial temperature gradients are negligible.

The benefits of a robust method for measuring the radial temperature profile are numerous; a few of which are highlighted. Accurate measurements of the radial temperature profile are required for studies of cross-magnetic-field heat transport [26] such as convective and conductive heat transport as well as heat transport due to Cherenkov emission of plasma waves [21, 24]. Additionally, a detailed study of the temperature dependence of viscosity in nonneutral plasmas

may aid in resolving the current discrepancies between experiment and theory [31]. Furthermore, it has been demonstrated that the widely studied two-dimensional $E \times B$ Diocotron modes have a radial temperature dependence that has yet to be fully characterized.

3.2 Overview of Temperature Measurement Technique

Determining the parallel kinetic energy distribution function (or equivalently, the parallel temperature profile for a Maxwellian plasma) consists of reducing the confinement barrier and measuring the radial profile of the number of escaping electrons. The magnitude of the confinement barrier is controlled by the "hold" voltage, V_H on the eject electrode; and the experimental data set consists of many measurements of the number of escaping electrons at different V_H. The kinetic energy distribution function can be determined by analyzing the relationship between the number of escaping electrons and the magnitude of the confinement barrier at each V_H. The number of escaping electrons per unit area is given by

$$Q_{exp}(r,V_H) = \int dz \int_{E_c}^{\infty} dE_{\|} \left(\frac{2}{m_e E_{\|}} \right)^{1/2} f(r,z,E_{\|}) \tag{3.1}$$

where $E_{\|} = (1/2)m_e v_z^2$ is the parallel (axial) kinetic energy, f is the energy distribution function and $E_c(r,z,V_H)$ is the confinement energy. E_c is the magnitude of the confinement barrier due to the hold voltage applied to the eject electrode. Alternatively, E_c can be described as the minimum kinetic energy required for an electron at $z = 0$ to escape out the end ($z = 0$ is the axial midpoint between the ineject and eject electrodes). The voltage of the inject electrode is maintained at V_c throughout the ejection process, and therefore no electrons can escape past the inject electrode.

In general, E_c varies radially and axially due to the spatial variation in the confinement potential, $\phi_c(r,z,V_H)$, and due to the spatial variation in the electron space charge potential, $\phi_p(r,z,V_H)$. The confinement energy at an (r,z) point is calculated as the difference between the maximum potential energy for the specified r and the potential energy, $q\phi(r,z,V_H)$, where

$\phi = \phi_p + \phi_c$ is the total potential and q is the signed particle charge (i.e. $q = -e$ for electrons). The equation for the confinement energy is given by

$$E_c(r,z,V_H) = q\phi(r,z_{max},V_H) - q\phi(r,z,V_H) \tag{3.2}$$

where the first term on the right hand side is the maximum potential energy (due to V_H) at each radius and is located at the axial point $z_{max}(r,V_H)$. Note that the dependence of z_{max} on V_H is due to the increasing importance of the $q\phi_p$ component of $q\phi$ as $q\phi_c$ decreases.

Fig 3.1(a) shows the potential energy and confinement energy along the $r = 0$ axis when the eject electrode voltage is at the full confinement potential, V_c. In Fig 3.1(a), the plasma is well confined such that $E_c \gg T \sim$ 1eV and therefore the electrons are trapped axially between the inject and eject electrodes. Fig 3.1(b) shows the energies when the eject electrode has been changed to $V_H = -40$ V in which case $E_c \sim E_\parallel$ for high energy electrons and some of the electrons will be able to escape from the confinement region.

The previous discussion outlines a general methodology of analyzing the escaping charge to determine the distribution function for nonneutral plasmas, and this was first introduced by Eggleston et. al [55] (referred to as E92). The underlying difficulty with this class of methods is that electrons escape from the trap when $q\phi_c \sim q\phi_p \gg E_\parallel$ meaning that the plasma potential plays a significant role in determining the confinement energy, and therefore in determining the number of escaping electrons at each V_H. This is in contrast to most uses of a retarding potential analyzer [66] where $q\phi_c \sim E_\parallel \gg q\phi_p$, in which case analysis of the escaping charge is simplified since the effects due to the electron space charge can be neglected. Determining the distribution function requires accurate calculation of E_c which in turn requires a model for calculating $q\phi$ at each V_H. We can easily solve for $q\phi_c$ using a Laplace equation solver, but solving for $q\phi_p$ is more difficult since it requires a self-consistent solution to the Poisson equation.

In order to deal with the difficulty arising from the calculation of $q\phi$, the E92 method requires that the confinement geometry satisfies the condition that $L_c \gg R_w$, in which case finite-

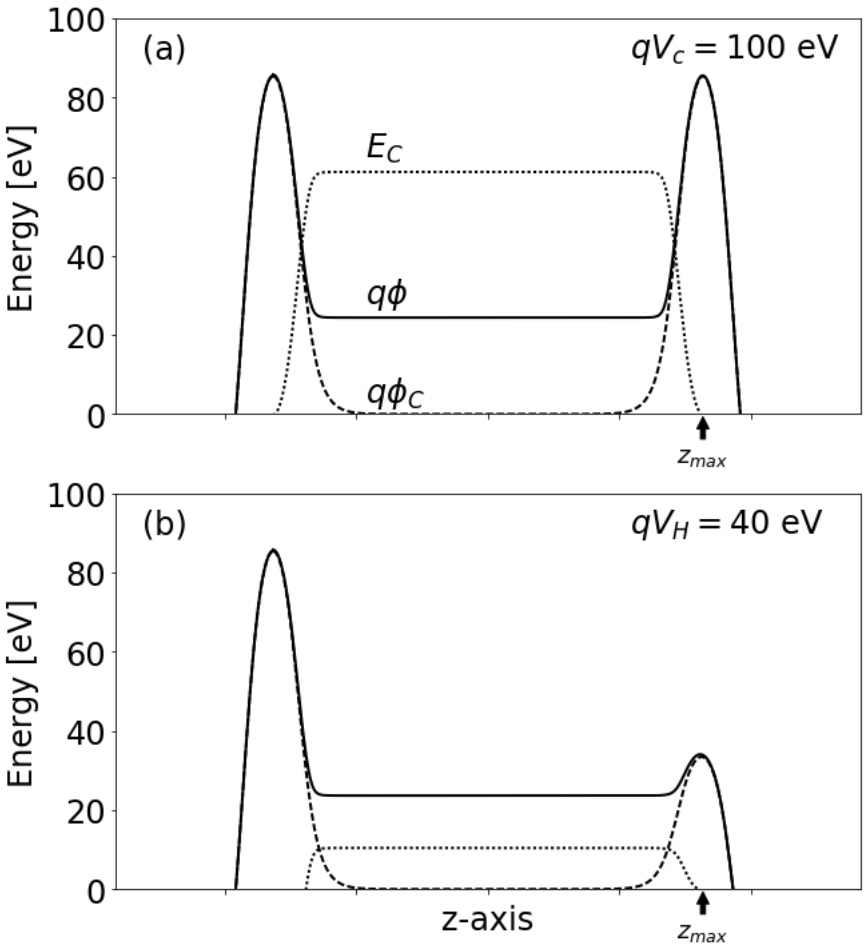

Figure 3.1: Plots of the potential energy and confinement energy along the trap axis at $r = 0$ cm. Plot (a) corresponds to the case in which both confinement electrodes are at the full confinement potential, $V_c = -100$ V. In Plot (b), the eject electrode voltage is set to $V_H = -40$ V while the inject electrode voltage remains at $V_c = -100$ V. z_{max} denotes the axial position of the peak confinement barrier due to the eject electrode voltage.

length effects are assumed negligible. The neglected finite length effects include curvature of the ends of the plasma column, effects due to axial expansion during the ejection process, and the axial dependence of E_c and ϕ.

The justification for neglecting finite-length effects is discussed using Fig. 3.1 which shows the potential energy and confinement energy of a plasma where $L_c/R_w = 15$. Due to Debye shielding, the potential is constant throughout the axial length of the plasma except in short regions at the axial ends where ϕ changes rapidly in a distance of a few Debye lengths. Therefore, the axial variation of $q\phi$ and E_c is significant only in the Debye sheaths at the ends of the plasma. For long plasma columns satisfying $L_c \gg R_w$, the Debye sheaths are a small fraction of the overall plasma length, and the associated finite-length effects are assumed to be negligible.

With the axial dependence neglected, the potentials can be calculated as functions of radius only. E_c is then given by the difference between ϕ_c, which is obtained from a radial Laplace equation, and ϕ_p which is obtained from a radial Poisson equation thereby obviating the need for a representation of the axial dependence of the potential. A benefit of the E92 method is that no restrictions are placed on the form of f, which can either be Maxwellian or non-Maxweillian and therefore the E92 method applies equally well to non-equilibrium plasmas [67, 68].

A simplified version of the E92 technique assumes that f is Maxwellian and then analyzes the initial $1-2\%$ of the escaping electrons. The initial electrons escape from the radial center of the trap since the minimum of E_c is located at the radial center; and therefore this simplified E92 technique can only measure the temperature near $r = 0$. ϕ_p is not significantly changed as the initial electrons escape, since these electrons are only a small fraction of the total charge; and therefore the relationship between Q_{exp} and E_c is simplified. The temperature can be found by a fit of the measured Q_{exp} to the equation $d(\ln N_{esc})/dE_c = -1.05/T$ where $N_{esc}(V_H) = \int 2\pi r dr\, Q_{exp}$ is the total number of escaping electrons. The simplified E92 technique is the standard method for measuring the temperature of nonneutral plasmas. However, several researchers [52, 69, 70, 71] have noted the need for finite-length corrections when the plasma is cold, or the plasma length is

short or when non-negligible axial expansion occurs during the ejection process.

In order to extend the E92 method to include finite-length effects, we require a model for calculating the (r,z) dependence of the potential and density. The typical method for solving for the (r,z) dependence is to allow for a sufficient number of inter-particle collisions such that the distribution function is Maxwellian along each r. Integration of the Maxwellian over the kinetic energy gives the Boltzmann equation for the density. Then the density and potential can be determined by iteratively solving the Boltzmann-Poisson system of equations

$$\nabla^2\phi(r,z) = -4\pi q n(r,z) \tag{3.3}$$

$$n(r,z) = n_0(r) exp\left(-\frac{q\phi(r,z)}{T(r)}\right) \tag{3.4}$$

where n_0 is a normalization factor that is determined by the constraint $Q(r) = \int dz\, n(r,z)$.

Unfortunately, the Boltzmann equation is not a valid representation for the density of trapped particles after some have escaped. That is, electrons escape in order from highest energy to lowest energy, and therefore the trapped electron distribution function is no longer a simple Maxwellian as electrons escape from the trap. Furthermore, the distribution function changes due to the axial expansion of the electron plasma as the hold voltage V_H is changed.

To account for changes in the distribution function during the ejection process, Hart et. al. [63] (referred to as H06), use a model where the distribution function is a truncated Maxwellian with a radial temperature profile $T(r)$. Using a truncated Maxwellian accounts for changes to the distribution function due to the ejection of electrons, but it does not account for changes due to axial expansion. The temperature profile is found by iterating $T(r)$ and comparing the number of escaping electrons predicted by the model with Q_{exp}. After iterating and converging to a final result for $T(r)$, H06 found that the truncated Maxwellian model can accurately predict Q_{exp} for the initial $10-25\%$ of the total escaping charge. The H06 method improves the calculation of E_c and ϕ by including some of the previously neglected finite-length effects, but at the loss of

applicability of the method to non-equilibrium plasmas since it requires that the initial unperturbed distribution function be Maxwellian.

The method presented in the next sections builds upon the H06 method by including changes to the distribution function due to axial expansion. We require that the hold voltage V_H be changed slowly, so that the length of the plasma changes slowly compared to the axial bounce motion of the electrons. Changing the eject electrode voltage in this manner preserves the bounce adiabatic invariant and allows for an accurate description of the electron distribution function at each V_H during the ejection process. The distribution function of the trapped electrons is modeled as a truncated Maxwellian but with an effective temperature $T'(r,V_H)$ that is determined by preservation of the bounce adiabatic invariant. T' is calculated using the initial unperturbed temperature profile $T(r)$, modified to account for expansion cooling as the length of the plasma expands as V_H is raised. Then, $T(r)$ is iterated until the number of escaping electrons predicted by the model matches Q_{exp}. We find that our model, which includes changes to the distribution function due to axial expansion and the ejection of electrons, can accurately predict Q_{exp} at all radii and all V_H.

3.3 Measurement of Escape Charge

We now discuss the experimental method for measuring the number of escaping electrons, Q_{exp}. Measurement of the radial temperature profile begins by performing manipulations of the plasma that result in a temperature profile, $T(r)$, that we intend to measure and that can be repeated with shot-to-shot variations $\leq 5\%$. We reduce the confinement barrier by raising the voltage on the eject electrode from the full confinement voltage, $V_c = -100$ V, to a higher voltage V_H. When the eject electrode voltage is at V_H, some electrons will have sufficient energy to overcome the confinement barrier and escape from the trap. The electrons which escape are recorded by the CCD camera giving us $Q_{exp}(r,V_H)$ for the specified V_H. After holding the eject

electrode voltage at V_H for a sufficiently long time, we dump the remaining electrons (which are not measured) and repeat the entire inject/manipulate/measure sequence but now at a different value for V_H.

An important criteria that must be satisfied during the ejection process is that the eject electrode voltage must be ramped sufficiently slowly such that the axial bounce adiabatic invariant of the electrons is conserved. The preservation of the bounce adiabatic invariant is necessary in order to accurately model the ejection process so that we can calculate ϕ and E_c which will be performed in the next section. The bounce adiabatic invariant is defined as $J = \oint dz\ p_z$ where the integral is over the axial length that the electron transits. J will be conserved when the plasma length, $L_p(r)$, is varied slowly compared to the axial bounce period $\tau_b = 1/f_b$. Therefore we are required to change the eject electrode voltage such that $((1/L_p)dL_p/dt)^{-1} \ll \tau_b$ to preserve the bounce adiabatic invariant. We typically use ramp rates ζ in the range of $\zeta = 1 - 4\ V/\mu s$ and for the experiment in this chapter we use a ramp rate of $\zeta = 1\ V/\mu s$.

In order to avoid overshooting the desired V_H by approaching V_H too rapidly, we ramp the eject electrode voltage to an intermediate trimming voltage given by $V_{trim} = V_H - 3$. The eject process beings with a ramp of the eject electrode voltage from V_c to V_{trim} at a rate of $1\ V/\mu s$. Then the voltage is ramped from V_{trim} to V_H at a rate of $0.3\ V/\mu s$. We hold the eject electrode voltage at V_H for $10\ \mu s$, which is several bounce periods in duration to ensure that all electrons with sufficient energy to escape from the trap are given enough time to do so. The voltage is then ramped back to V_{trim} with a ramp rate of $0.3\ V/\mu s$. The final ramp is from V_{trim} back to V_c at a rate of $10\ V/\mu s$ and is done to prevent the remaining trapped electrons from escaping. Fig 3.2 shows the ramp profile of the eject electrode voltage for $V_H = -40\ V, -20\ V$ and $+2\ V$. Note that because the ramp rates are fixed, the total duration of the ejection process increases as V_H increases.

After the CCD camera has finished recording the signal from the escaping electrons we discard the remaining trapped electrons by ramping the eject electrode voltage to ground. The

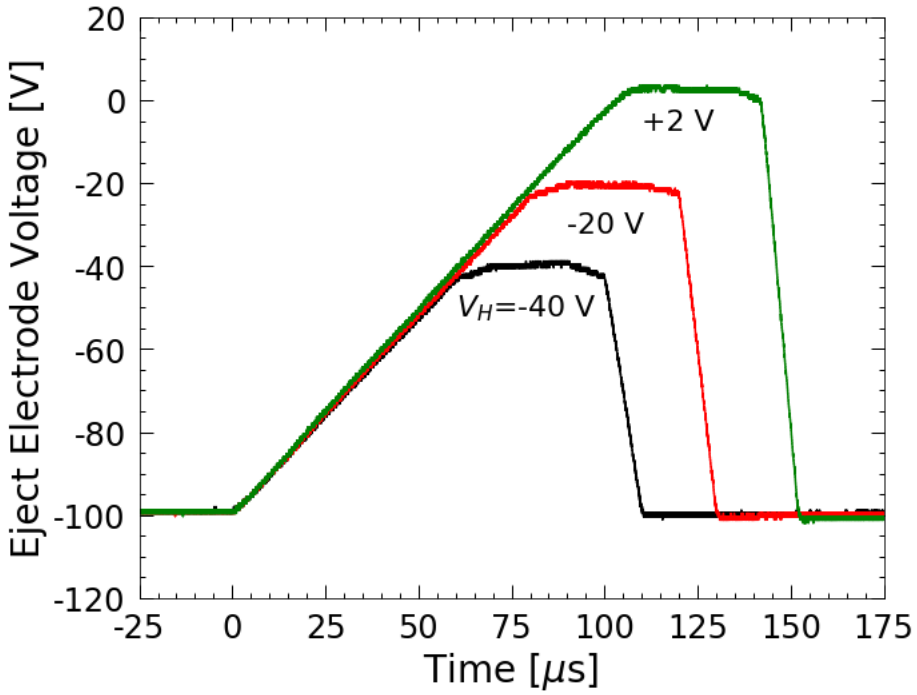

Figure 3.2: Oscilloscope traces showing the ramping of the eject electrode voltage for three settings of V_H. The ramps begin at $t = 0\ \mu s$ with an initial ramp rate of $\zeta = 1\ V/\mu s$ and the eject electrode voltage is held at $V_c = -100$ V when not ramping.

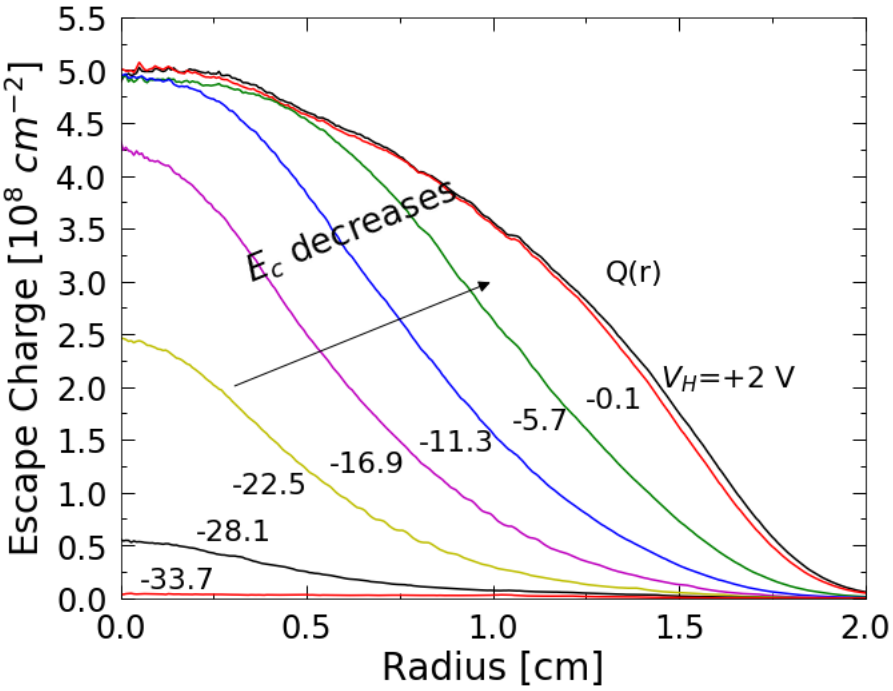

Figure 3.3: Radial profiles of measured escape charge at several hold voltages. $Q(r)$ is the total z-integrated density profile that is obtained by ejecting the entire plasma.

experiment is repeated and the same ejection procedure is used except this time we ramp the eject electrode to a different V_H. Typically, we repeat the experiment ≈ 70 times and vary V_H in 0.7 V steps starting from $V_H = -40$, i.e. $V_H = -40, -39.3, -38.6, ..., -0.1, +0.6, +1.3, +2$ V. The range of V_H values depends on the temperature and density of the plasma. The lowest voltage is chosen such that electrons are just beginning to escape from the trap. Higher temperature or higher density plasmas require a lower starting voltage for V_H since electrons will be able to escape at larger values of E_c.

For positive values of V_H, the entire plasma escapes and no electrons remain in the trap. We perform an additional six cycles with $V_H = +2$ and then we average all of the $Q_{exp}(r, V_H)$ profiles with $V_H > 0$ to give us the fully ejected z-integrated density profile $Q(r)$. The averaging is done to reduce error associated with shot-to-shot variations. Fig. 3.3 shows Q as well as Q_{exp} for several V_H voltages.

For cold plasmas ($T < 0.01$ eV), the ramping process must complete in less time than the

$\nu_{\perp\|}^{-1}$ re-thermalization time. Collisions between particles during the ejection process can cause an up-scattering of a particle's energy such that the particle may escape from the trap at a larger value of E_c than it would have if there had been no collisions. The model we use for calculating ϕ and E_c necessarily assumes that the plasma is collisionless during the ejection process, and therefore any collisional processes would confuse the measurements.

3.4 Model for Ejection Process

We now discuss the model used to calculate $\phi(r,z)$ and thereby the confinement barrier E_c at each hold voltage V_H. We assume that the initial unperturbed distribution function is Maxwellian along each field line (i.e. at each r),

$$f(r,z,E_\|,V_c,T) = n_0(r)\left(\frac{m_e}{2\pi T}\right)^{1/2} exp\left(-\frac{E_\| + q\phi}{T}\right) \tag{3.5}$$

By unperturbed we mean that the the eject electrode voltage is at V_c and the ejection process has not begun. As the voltage on the eject electrode is changed from V_c to V_H, the distribution function will deviate from its initial unperturbed form.

There are two effects responsible for the change in the distribution function. Firstly, the plasma expands axially as the eject electrode voltage is raised toward ground, and this will adiabatically cool the electrons. The changes in the temperature can be accounted for by using an effective temperature $T'(r,V_H)$ that is calculated using the relation for 1D adiabatic expansion

$$T'(r,V_H) = T(r)\left(\frac{L_p(r)}{L'_p(r,V_H)}\right)^2 \tag{3.6}$$

Here $T(r)$ is the temperature profile of the unperturbed plasma, $L_p(r)$ is the length of the unperturbed plasma, and $L'_p(r,V_H)$ is the length at each V_H. The length at each V_H is calculated as a density weighted average using

$$L'_p(r,V_H) = \frac{\left[\int dz\, n_{tr}(r,z,V_H)\right]^2}{\int dz\, [n_{tr}(r,z,V_H)]^2} \tag{3.7}$$

where n_{tr} is the trapped particle density. Eq. (3.7) is also used to calculate $L_p(r)$ when the model is solved with the eject electrode voltage at V_c and in this case it is equivalent to Eq. (2.12). Using Eq. (3.6) for the temperature due to adiabatic expansion, the general form of the distribution function due to expansion is then given by

$$f(r,z,E_\parallel,V_H,T) = n_0(r,V_H)\left(\frac{m_e}{2\pi T'}\right)^{1/2} exp\left(-\frac{E_\parallel + q\phi}{T'}\right) \tag{3.8}$$

which is a Maxwellian with a variable temperature.

The second change to the distribution function is that electrons will escape from the trap in order from highest to lowest kinetic energy and therefore the trapped electron distribution function is truncated at E_c. The trapped electron density is found by integrating the distribution function

$$\begin{aligned} n_{tr}(r,z,V_H,T) &= \int_0^{E_c} dE_\parallel \left(\frac{2}{m_e E_\parallel}\right)^{1/2} f(r,z,E_\parallel,V_H,T) \\ &= n_0\, exp\left(-\frac{q\phi}{T'}\right) erf\left(\sqrt{\frac{E_c}{T'}}\right) \end{aligned} \tag{3.9}$$

Electrons with $E_\parallel > E_c$ will escape from the trap and we define n_{esc} to represent the number density of electrons that escape from an (r,z) point within the trap

$$\begin{aligned} n_{esc}(r,z,V_H,T) &= \int_{E_c}^{\infty} dE_\parallel \left(\frac{2}{m_e E_\parallel}\right)^{1/2} f(r,z,E_\parallel,V_H,T) \\ &= n_0\, exp\left(-\frac{q\phi}{T'}\right) erfc\left(\sqrt{\frac{E_c}{T'}}\right) \end{aligned} \tag{3.10}$$

We can now use Eq (3.9) to solve for the potentials using Poisson's equation

$$\nabla^2\phi(r,z) = -4\pi q n_{tr} \tag{3.11}$$

In order to conserve the total number of particles along each r, we normalize n_{esc} and n_{tr} at each V_H such that

$$Q(r) = \int dz\, n_{tr}(r,z,V_H,T) + \int dz\, n_{esc}(r,z,V_H,T) \tag{3.12}$$

where $Q(r)$ is the fully ejected z-integrated density.

We now have a system of self-consistent equations that can be numerically iterated to solve for $q\phi$ and E_c at each V_H. The model requires a temperature profile $T(r)$, a fully ejected z-integrated density profile $Q(r)$ and specification of the boundary conditions. A solution to the model is found by numerically iterating the self-consistent equations on a 64×256 (r,z) grid until convergence is achieved. We first solve the model with the electron distribution function given by Eq. (3.5) and with the eject electrode voltage set to V_c ; this is equivalent to solving the Boltzmann-Poisson equations. From the solution with the eject electrode at V_c we use Eq. (3.7) to calculate $L_p(r)$. With $L_p(r)$ we can now solve the model with the eject electrode voltage at different values of V_H to determine $q\phi(r,V_H)$ and $E_c(r,V_H)$.

For a given V_H we calculate the trapped and escaping electron densities using Eq. (3.9) and Eq. (3.10) where the confinement energy is given by Eq. (3.2). The effective temperature is calculated using Eq. (3.6), where the plasma length is calculated using Eq. (3.7). We then calculate the potential using Eq. (3.11) and require the normalization from Eq. (3.12). We typically solve the model at 160 values for V_H in 0.25 V steps. For the data under consideration in Fig.3.3 we begin at $V_H = -40$ V and the model is solved at eject voltages of $V_H = -40, -39.75, ..., -0.25, 0$ V.

The results of the model are shown in Fig. 3.4 for three eject electrode voltages. The

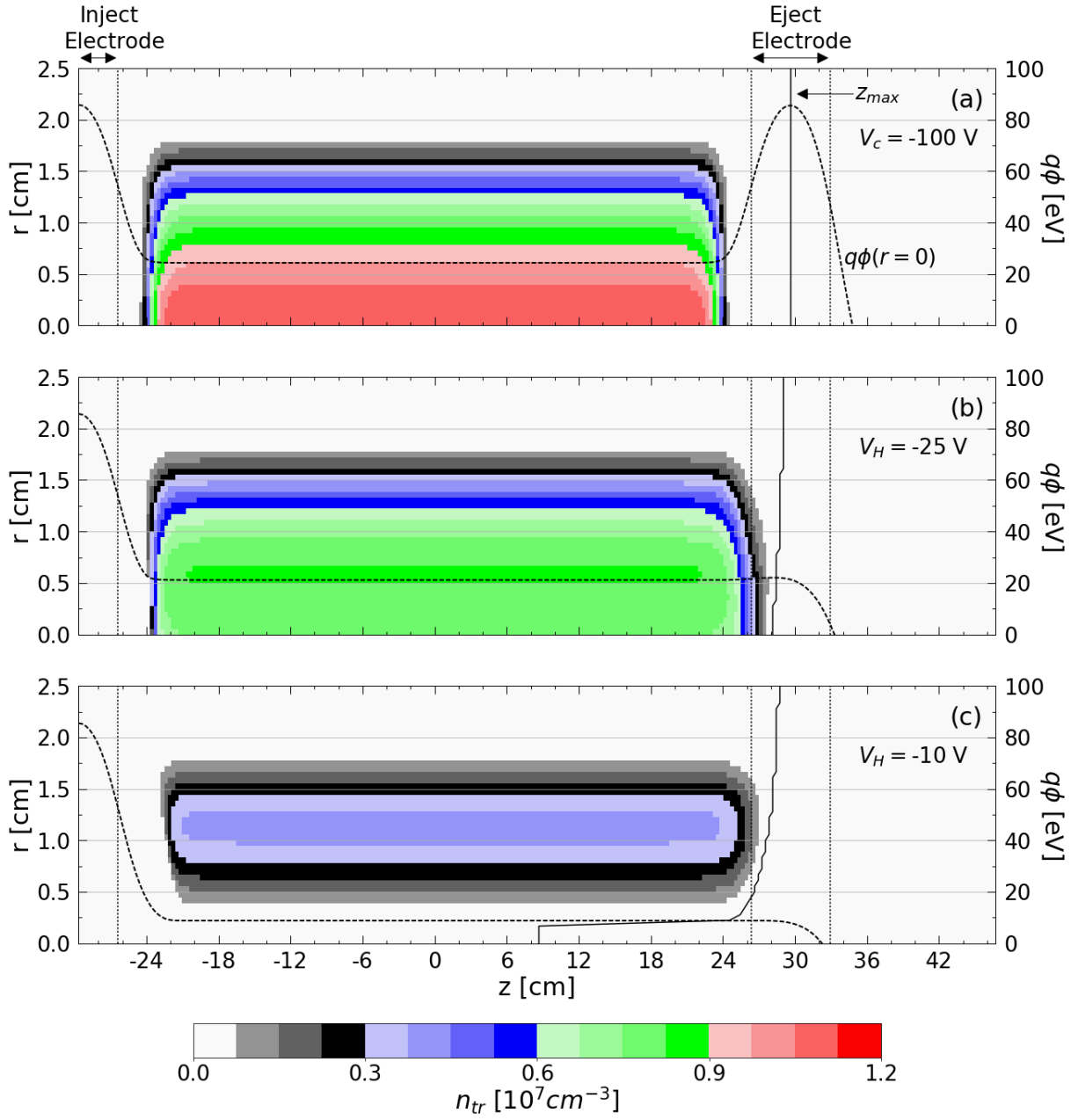

Figure 3.4: Model results when the eject electrode voltage is at (a) $V_c = -100$ V, (b) $V_H = -25$ V and (c) $V_H = -10$ V. The trapped particle density n_{tr} is overlaid with the on-axis potential energy $q\phi(r=0)$ (dashed line). The three vertical dotted lines represent the axial boundaries of the inject electrode (leftmost dotted line) and eject electrode (middle and right dotted lines). The solid line shows the barrier location z_{max} which is the position of the maximum potential energy due to the eject electrode.

three vertical dotted lines represent the axial boundaries of the inject electrode (left dotted line) and the eject electrode (middle and right dotted lines). The dashed line represents the on-axis potential energy $q\phi(r=0)$. We only model half of the full length of the inject electrode because of the reflected symmetry of the boundary condition and because the inject electrode voltage is always maintained at V_c. Therefore any electrodes upstream of the inject electrode do not affect the plasma. In contrast, the potentials on the electrodes downstream of the eject electrode become important as V_H gets closer to ground therefore we include the region beyond the eject electrode as shown in Fig. 3.4.

Fig. 3.4(a) shows the model solution when the eject electrode voltage is at $V_c = -100$ V and represents the full confinement scenario. In the full confinement scenario we have $L(r) < L_c$ as shown in Fig 3.4(a) where we see that the density of the plasma ends ≈ 2 cm before reaching the confinement electrodes. Fig 3.4(b) shows the model solution when $V_H = -25$ V where the plasma has expanded in length such that the end of the plasma is located within the boundary of the eject electrode. At an eject voltage of $V_H = -25$ V approximately 20% of the electrons have escaped from the trap with the majority escaping from the radial center. Fig 3.4(c) shows the model solution when $V_H = -10$ V where we see that the center of the plasma column has become hollow and electrons are confined only at larger radii.

The solid line in Fig 3.4 shows the location of $z_{max}(r, V_H)$ which is the location of the peak of the confinement barrier. When the eject electrode voltage is at V_c as in Fig 3.4(a) then z_{max} is located at the same axial position for at all radii. Furthermore, z_{max} is located at the axial midpoint of the eject electrode which indicates that the position of z_{max} is entirely determined by the potential from the eject electrode. As the eject electrode voltage is raised towards ground the self-potential of the plasma shifts the position of z_{max} closer to the plasma as seen in Fig3.4(b,c). In other words, the position of the peak of the confinement barrier moves closer to the plasma as the plasma potential becomes comparable to the confinement potential.

3.5 Temperature Iteration

The model presented in the previous section requires as input an estimate for the radial temperature profile, $T(r)$, which is the profile that we are attempting to determine. Given a $T(r)$ profile, the model predicts $Q_{mod}(r,V_H)$ as the number of escaping electrons at each hold voltage. In order to determine the correct $T(r)$ that represents the actual temperature profile of the experiment we must iterate the $T(r)$ supplied to the model until Q_{mod} is equal to Q_{exp} at all r and V_H. To begin the process we make an initial guess for $T(r)$ and solve the model at all values of V_H. The model prediction for the number of escaping electrons is given by

$$Q_{mod}(r,V_H,T) = \int dz\, n_{esc}(r,z,V_H,T) \tag{3.13}$$

Since the initial $T(r)$ supplied to the model is a guess we do not expect the model prediction will accurately represent the experiment. That is, we do not expect there to be good agreement between Q_{exp} and Q_{mod} with our initial guess for $T(r)$. To make a new guess for $T(r)$ we use a non-linear least square solver that utilizes the Levenberg-Marquardt (LM) algorithm to iterate $T(r)$. We use the LM solver to minimize the residuals

$$\chi^2 = \sum_{r,V_H} \Big[log\big(Q_{exp}(r,V_H)\big) - log\big(Q_{mod}(r,V_H,T)\big) \Big] \tag{3.14}$$

We use the logarithm of Q_{exp} and Q_{mod} in order to give equal weight to low and high densities. The LM solver attempts to minimize χ^2 by iterating $T(r)$. For each iteration the solver must recalculate Q_{mod} using Eq. (3.13) where n_{esc} is calculated using Eq. (3.10). To calculate n_{esc} we need to know $q\phi$, E_c and T'. We use the previous model solution for $q\phi$ and E_c where the model was solved using the initial $T(r)$ guess. We calculate T' using Eq. (3.6) where L'_p and L_p are given by the previous model results based on the initial $T(r)$ guess but the $T(r)$ used in Eq. (3.6) is the most recent iteration from the LM solver.

Once the LM solver has converged to a new $T(r)$ profile we average the previous $T(r)$

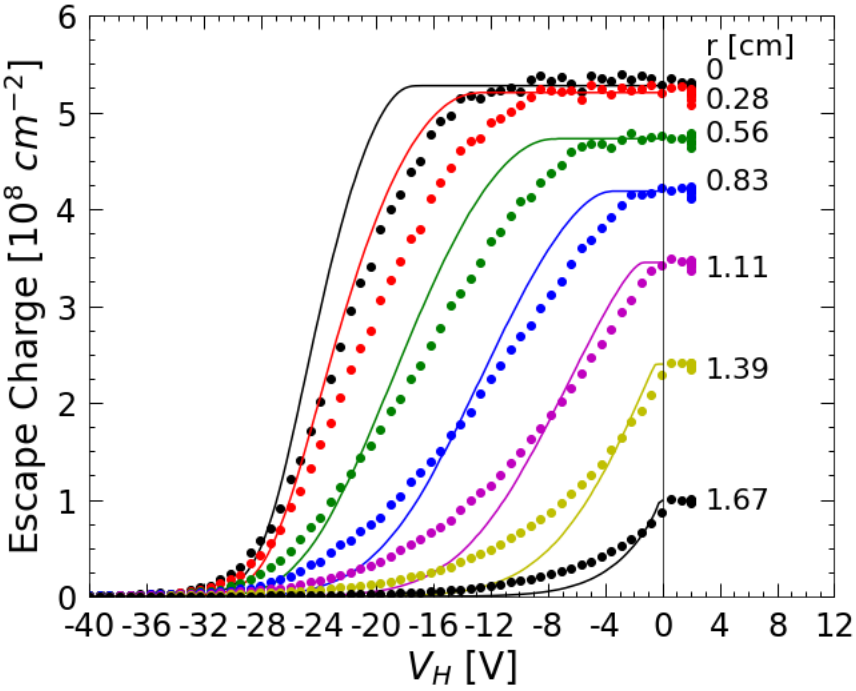

Figure 3.5: Comparison between the measured escape charge, $Q_{exp}(r,V_H)$, (circles) and the model predicted escape charge, $Q_{mod}(r,V_H)$, (lines) using an initial guess for the temperature profile which is $T(r) = 1$ eV.

profile with the new $T(r)$ profile and then we rerun the Poisson solver with the averaged $T(r)$ profile. Running the model with the averaged $T(r)$ profile generates new results for $q\phi$, E_c, L_p and L_p'. We then run the LM solver again to obtain a new guess for $T(r)$. We cycle through the Poisson and LM solvers until there is negligible change in the newest $T(r)$ profile found from the LM solver and the previous $T(r)$ iteration. We typically require 5-10 cycles through the Poisson and LM solvers in order to converge to a final $T(r)$ profile.

Fig 3.5 shows the first step in the temperature iteration process. In Fig 3.5 we plot the comparison between Q_{exp} and Q_{mod} when the temperature profile used to calculate Q_{mod} is the initial guess for $T(r)$. In this particular case, the initial temperature profile guess was set to be a uniform temperature profile at 1 eV, that is, $T(r) = 1$ eV. The circles represent the measured data and the solid lines represent the model prediction. The results are plotted at several radii that span the full radial extent of the plasma. Clearly, there is poor agreement between the model prediction

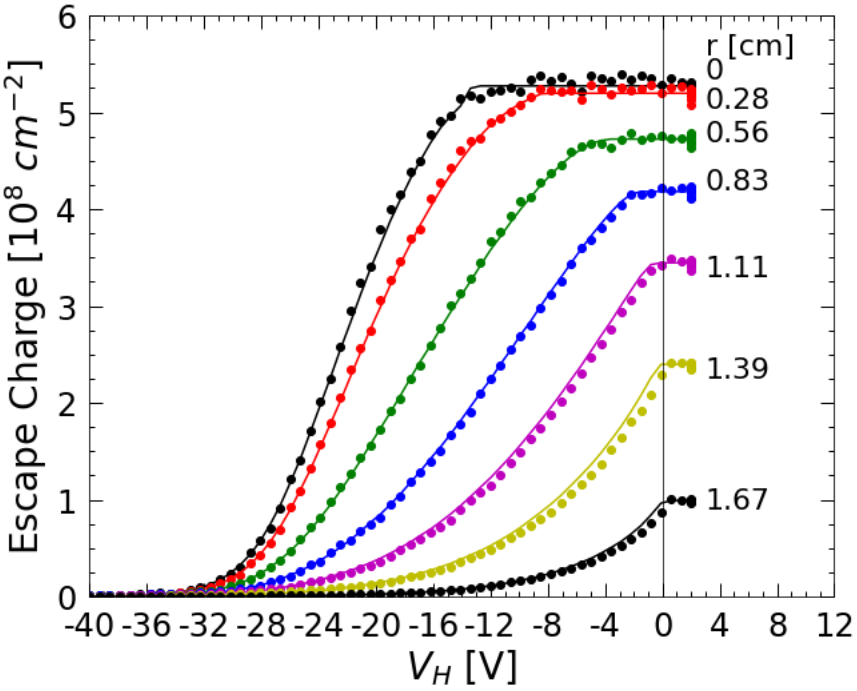

Figure 3.6: Comparison between the measured escape charge, $Q_{exp}(r,V_H)$, (circles) and the model predicted escape charge, $Q_{mod}(r,V_H)$, (lines) using the final converged temperature profile.

and the experiment which is to be expected from our initial guess which is a rough approximation to the actual temperature profile. We then iterate though the LM and Poisson solvers about seven time until we converge to the final temperature profile which represents the actual temperature profile of the plasma in the experiment. Fig. 3.6 shows the comparison between Q_{exp} and Q_{mod} using the final converged $T(r)$ profile. We see that there is excellent agreement between Q_{exp} and Q_{mod} at all r and V_H. The converged temperature profile corresponding to the data and model results shown in Figs. 3.3-3.6 is the $T(r)$ profile shown in Fig. 4.3(a) with an asymmetry tilt duration of 300 ms (blue curve). The asymmetry tilt and the creation of the temperature profile will be discussed in Chapter 4. We note that the temperature profile has a large radial temperature gradient where the plasma is 1.5 eV near $r = 0$ and 3 eV at the radial edge of the plasma.

As a concluding remark, some caution should be employed when using Eq. (3.6) to represent the temperature due to changes in the calculated length of the plasma. Typically, as V_H is raised towards ground the electrons at each radius cool due to the adiabatic expansion that arises

from the lowering of the confinement barrier. However, Eq. (3.6) would indicate heating of the electrons if $L'_p(r,V_H) < L_p(r)$ at a particular radius and V_H. In practice, we observe that initially $L'_p(r,V_H)$ increases as V_H is raised to ground but when the density at a given radius becomes very small then we observe that the calculated $L'_p(r,V_H)$ actually begins to decrease and eventually it becomes smaller than $L_p(r)$ which, according to Eq. (3.6), would indicate heating of the electrons that remain in the trap. It is unclear whether the heating predicted by direct usage of Eq. (3.6) actually occurs in the experiment.

The observed decrease in $L'_p(r,V_H)$ only occurs at a given radius when the density at that radius has becomes very small (typically 1% of the initial value) in which case these electrons have negligible effect on the temperature analysis, i.e. the heating predicted by Eq. (3.6) does not affect the final temperature profiles. Therefore I conclude that direct usage of Eq. (3.6) is acceptable even though it allows for compression heating of the last electrons to escape from the trap for a given radii. To verify this conclusion, I have calculated the final temperature profiles for a variety of experimental configurations using the method presenting in this chapter but I have tried two different methods for the calculation of $T'(r,V_H)$. In the first, I have used Eq. (3.6) exactly which allows for some compression heating of the last electrons to escape from the trap at a given radii. In the second method, I have used Eq. (3.6) but I only allow for cooling of the electrons; compression heating is prevented. I find that there is negligible difference between the temperature profiles obtained using the two different methods for calculating T'.

3.6 Hollow Diocotron Instability

Ideally when allowing electrons to escape from the trap we would like to ramp the eject electrode voltages as slowly as possible in order to conserve the bounce adiabatic invariant. However, the V_H ramp rate ζ has a lower limit which is set by the growth of the hollow Dioctron instability [72]. The instability arises when the rotation profile of the plasma becomes nonmono-

tonic due to the hollowing of the density profile caused by electrons escaping from the axial center of the trap (c.f. Fig 3.4(c)).

Since an axially centered hollow profile is an unstable equilibrium, the instability grows from noise fluctuations and therefore the onset of the hollow Diocotron instability must be determined experimentally. Measurement of the onset of the dioctron instabilty can be made by using the collector plate to determine the time at which point there is significant radial transport from the instability [55]. Since the instability grows from noise there will be noticeable shot-to-shot variation, nevertheless we can determine a minimum time when the instability begins and then ensure that the ramp rates are chosen such that the measurement of Q_{exp} is completed before the instability has grown to a non-negligible amplitude.

We measure the onset of the hollow Diocotron instability by ramping the eject electrode voltage to V_H and holding at V_H for a time duration of $\Delta t = 2500\ \mu s$ which is long compared to the rotation period, $\Delta t \gg \tau_E$. When the hollow Diocotron instability arises it will cause radial transport of electrons, some of which will move towards the radial center of the trap where they may have sufficient energy to overcome the confinement barrier and escape from the trap. Therefore we can determine the onset of the hollow Dioctron instability by observing sharp transitions in the measured voltage signal of the RC circuit. We have measured the time for the onset of the hollow Dioctron instability for two magnetic fields, $B = 13$ kG and $B = 9$ kG, and two confinement lengths $L_c = 38.5$ cm and $L_c = 17.5$ cm , the results of which are shown in Fig 3.7. We observe no correlation between the time for the onset of the hollow Diocotron instability and V_H. Fig 3.7 also shows the total time required to measure Q_{exp} when using ramp rates of $\zeta = 1$ V/μs (solid line) and $\zeta = 0.5$ V/μs (dashed). The time for the onset of the hollow Diocotron instability occurs at least 200 μs after the time required to measure Q_{exp} and therefore we conclude that the hollow Dioctron instability is not interfering with the measurement of Q_{exp}.

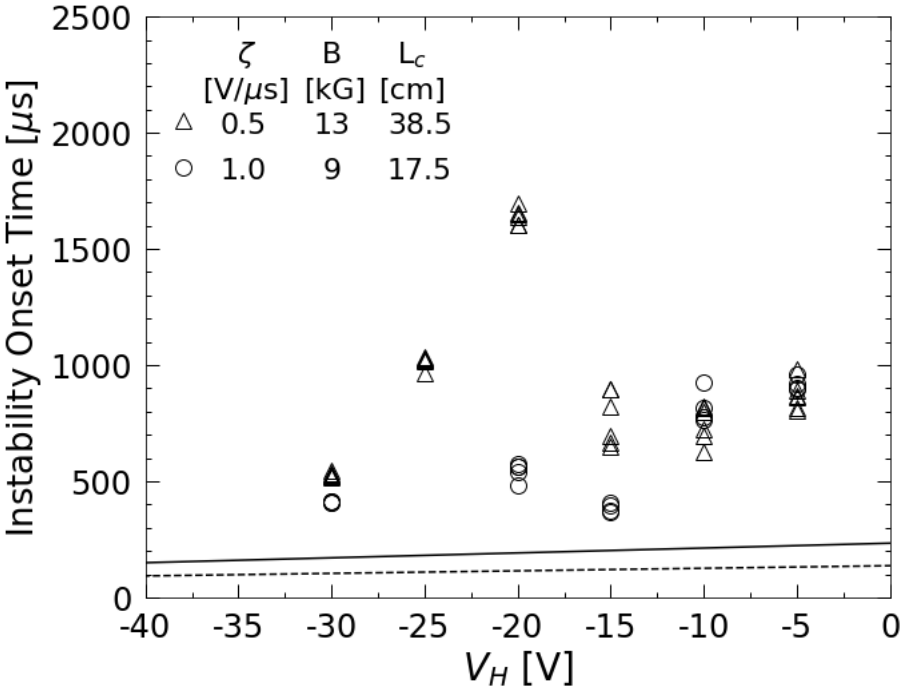

Figure 3.7: Measurements of the time for the onset of the hollow Diocotron Instability. The lines indicate the total time required to measure the escaping electrons when the ramp rate is $\zeta = 1$ V/μs (solid) and $\zeta = 0.5$ V/μs (dashed). The onset of the hollow Diocotron instability begins at least 200 μs after the time required for the escaping electrons to be measured.

3.7 Comparison with on-axis Temperature Measurement Technique

In order to give additional validation of the temperature measurement technique presented in this chapter, we compare the new technique with the widely-used and established on-axis temperature measurement technique [55]. The measurement is made by rotating the collector plate to block the axial path of the escaping electrons and then analyzing the first 1% of electrons that escape. We refer to on-axis temperature measurements made using the collector plate as, T_{CP}.

Approximately 200 temperature profiles have been measured using the temperature measurements technique presented in this chapter. The measured temperatures range from $0.1 \leq T \leq 4$ eV and confinement lengths range from $17.5 \leq L_c \leq 52.5$ cm. For a subset of those 200 temperature profiles, the temperature gradient is small and we have also made measurements of the temperature at $r = 0$ using the on-axis temperature measurements technique yielding T_{CP} (See Appendix A). The T_{CP} measurements are then compared with the radial temperature profile at $r = 0$, that is, we compare T_{CP} with $T(r = 0)$ and we expect the two measurements to agree since the radial temperature gradients are small. The comparison between T_{CP} and $T(r = 0)$ are shown in Fig. 3.8 and we see that there is generally good agreement between the two measurement techniques.

3.8 Summary

We have presented a technique for measuring the radial profile of the parallel temperature of a nonneutral plasma. The temperature measurement technique consists of measuring the radial profile of the number of escaping electrons as the confinement barrier is reduced. We then use a model that takes as input a radial temperature profile and gives a prediction for the number of escaping electrons. We iterate the temperature profile until the number of escaping

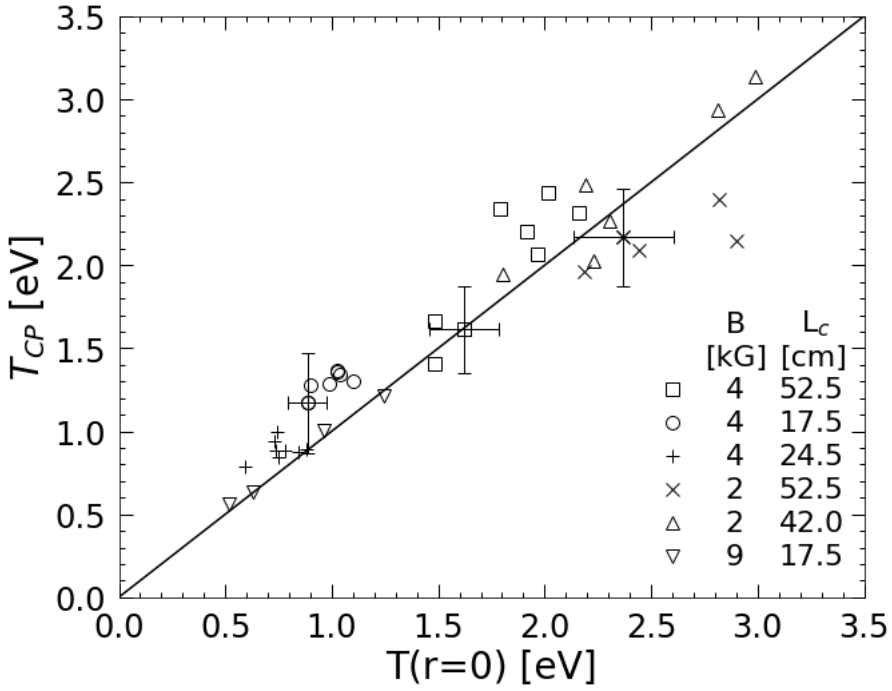

Figure 3.8: Comparison of T_{cp} using the collector plate and the temperature at $T(r=0)$ using the method presented in this chapter. Error bars for $T(r=0)$ represent 10% systematic error and error bars for T_{cp} are from 10% systematic error combined in quadrature with standard deviation from multiple trials.

electrons predicted by the model matches the experimentally measured number of escaping electrons. The model includes finite-length effects such as the curvature of the ends of the plasma column, cooling due to adiabatic expansion and truncation of the distribution function during the ejection process. The temperature measurement technique presented enables the determination of the temperature profile with excellent spatial resolution as well as accurate predictions of the number of escaping electrons at all radii and all eject voltages. In the next section we will study measurements of the temporal evolution of $T(r,t)$ when the plasma is subject to different manipulations.

In consideration of future research efforts, the temperature measurement method presented in this chapter has broader applications beyond determining the radial temperature profile. The method demonstrates that by ramping the eject electrode voltage adiabatically, the trapped particle distribution function is known at any point in the ejection process. A modification to the eject electrode ramp profiles used for measuring the temperature profile will result in a fully confined plasma that has a truncated Maxwellian distribution function which can then be used as an initial condition for experiments utilizing a non-equilibrium distribution function. The modification would be to use a symmetric ramp profile where the final ramp from V_{trim} back to V_c has the same ramp rate as the initial ramp from V_c to V_{trim}. A symmetric ramp profile with a sufficiently slow ramp rate would ensure that the bounce adiabatic invariant is preserved at all times.

When measuring the radial temperature profile, we are not interested in the trapped particles after we have held the eject electrode voltage at V_H and have measured Q_{exp}. Therefore, we use a fast ramp of the eject electrode voltage back to V_c such that the bounce adiabatic invariant is not preserved. However, if the final ramp from V_{trim} back to V_H is done adiabatically, then the trapped particle distribution function can be determined from preservation of the bounce adiabatic invariant. Using a symmetric ramp profile with adiabatic ramp rates would then result in a fully confined plasma with a truncated Maxwellian distribution function that can be accurately calculated. An experiment that utilizes a truncated Maxwellian distribution would be to measure

the rate at which the truncated Maxwellain distribution collisionally relaxes back to a Maxwellian. In addition, truncating the distribution function can be used to remove Landau damping of Trivelpiece-Gould waves when the truncation removes particles with velocities that are equal to the wave phase velocity [73].

3.9 Acknowledgments

This chapter, in part, is currently being prepared for submission for publication. K. A. Thompson, A. A. Kabantsev, N. Panzeri and C. F. Driscoll. The dissertation author was the primary investigator and author of this material.

Chapter 4

Temperature Measurement Experiments

4.1 Introduction

In this chapter we consider the temporal evolution of $T(r,t)$ for different experimental configurations. The purpose of these experiments is two-fold; the first is to demonstrate and test the multi-shot radial temperature profile measurement technique, and when available compare the results with the established single-shot $r = 0$ T_{CP} measurement technique. The second purpose is to determine plasma manipulation techniques that create radial temperature gradients optimized for studying radial heat transport. The experiments are presented in order from low magnetic field to high magnetic field. Interpretation of the results requires a discussion of some expected heating and cooling mechanisms for electron plasmas.

At low magnetic field, the plasma expands rapidly due to asymmetry-induced transport from intrinsic external trap asymmetries, that are assumed to to be time independent in the lab frame. Here, external asymmetries cause asymmetric (but reversible) particle orbits, which are made irreversible by random eletron-electron collisions. If there are no other time-dependent heating or cooling mechanisms, then the Hamiltonian of the system is time independent; in which case the total energy of the plasma is conserved. As the plasma expands, the self-potential ϕ_p of

the plasma is reduced, decreasing the total electrostatic energy. The decrease in the electrostatic energy is compensated for by an increase in the plasma thermal energy through Joule heating. Therefore the radial expansion converts electrostatic energy H_ϕ into thermal energy H_T, but the total energy H_{Tot} will remain constant. These terms are calculated as energy per electron and are given by

$$H_{Tot} = H_\phi + H_T \tag{4.1}$$

$$H_\phi = \frac{1}{N}\int dV \frac{|\mathbf{E}^2|}{8\pi} = \frac{1}{2N}\int 2\pi r dr dz\, n(r,z) e\phi(r,z) \tag{4.2}$$

$$H_T = \frac{1}{N}\int dV \frac{3}{2} nT = \frac{1}{N}\int 2\pi r dr dz \frac{3}{2} n(r,z) T(r) \tag{4.3}$$

where $\mathbf{E}$ is the electric field. Experimentally, $n(r,z)$ and $\phi(r,z)$ are numerical solutions to the Boltzmann-Poisson equations (Eq. (3.3) and Eq. (3.4)) given the measured $Q(r)$ and $T(r)$. Here, $T(r)$ is determined using the technique presented in Chapter 3.

Internal electron-electron interactions also cause measurable inward and outward particle fluxes, although these conserve the total angular momentum $P_\theta \sim \langle r^2 \rangle$. Radial fluxes are transport due to particle diffusion and this is macroscopically described as viscosity acting on shears in the rotation profile. The global thermal equilibrium is a constant temperature, shear-free state [74]. When there is shear in the rotation profile, viscous drag between the shear layers results in forces in the θ-direction which in turn causes radial drift-velocity fluxes that reduce the shear. These viscosity driven fluxes also result in local Joule heating and cooling.

Conservation of P_θ by viscous transport is in contrast to transport due to external asymmetries which can torque on the plasma and cause changes in P_θ. In practice, the observed radial fluxes are a combination of asymmetry-driven transport plus viscous fluxes. However, the strength of asymmetry-driven transport can be unambiguously identified by tracking changes in $\langle r^2 \rangle$.

Finally we consider temperature changes due to axial compression and expansion. For

Table 4.1: Integrals for radial expansion due to intrinsic external asymmetries showing thermal energy H_T, electrostatic energy H_ϕ and total energy H_{Tot} per particle at $B_z = 2$ kG, $L_p^* = 48$ cm.

Confinement Time $[s]$	$\langle r^2 \rangle$ $[cm^2]$	H_T $[eV]$	H_ϕ $[eV]$	H_{Tot} $[eV]$
0.5	0.713	0.81	12.03	12.84
1.0	0.724	0.94	11.86	12.80
1.5	0.735	1.19	11.73	12.92

the experiments reported in this chapter we do not actively compress or expand the plasma, but, the plasma can be compressed by the confinement potentials when the self-potential of the plasma decreases due to radial expansion [75]. The length of the plasma is determined by an equilibrium between the outwardly directed electrostatic pressure from the plasma self-potential, the outwardly directed plasma thermal pressure, and the inwardly directed electrostatic pressure from the confinement potentials. As the plasma expands radially, the self-potential of the plasma decreases and a new, shorter equilibrium length is achieved as the power supplies maintaining the confinement potentials do work to compress the plasma to the new equilibrium length. For the experiments reported in this section the change in the length during radial expansion is of the order $\delta L_p / L_p < 2\%$, and so the work done by the power supplies is taken to be negligible.

4.2 Radial Expansion from Intrinsic External Asymmetries

As a first example of the temporal evolution of $T(r,t)$, we present measurements at three confinement times, $t_c = 0.5$ s, 1.0 s and 1.5 s, where no external perturbations are applied and the magnetic field is $B = 2$ kG. For these measurements, the plasma is confined between electrodes 1 and 10 giving a confinement length of $L_c = 52.5$ cm and an effective plasma length of $L_p^* = 48$ cm. Electrodes 2-9 and all of the sectors of electrodes 4 and 7 are grounded. Fig. 4.1 shows the measured $Q(r,t)$ and $T(r,t)$ profiles from which H_ϕ, H_T and $\langle r^2 \rangle$ are calculated and given in Table 4.1.

During the evolution from 0.5 s to 1.5 s, H_ϕ decreases by $\approx 3\%$ and H_T increases by

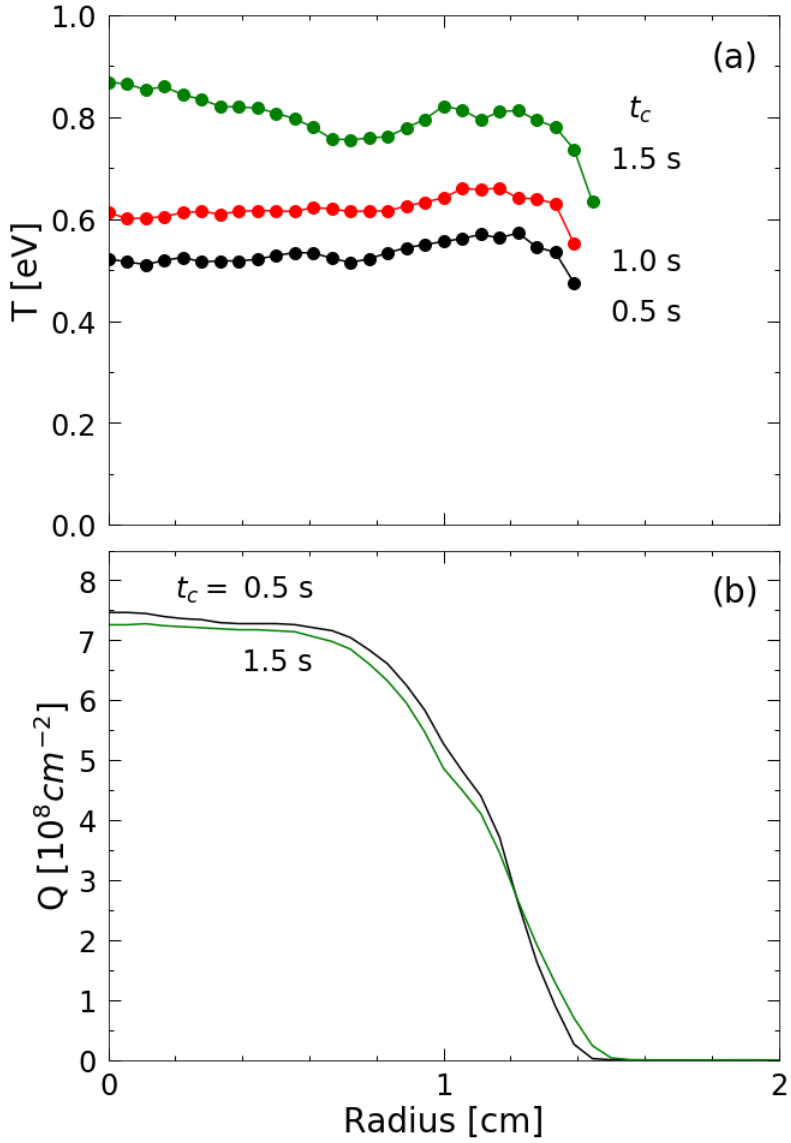

Figure 4.1: Temperature (a) and z-integrated density (b) profiles taken at confinement times of 0.5 seconds (black), 1 second (red) and 1.5 seconds (green). For visual clarity, the density profile at 1 second is omitted but would reside between the density profiles at 0.5 and 1.5 seconds. The radial temperature profile fit is obtained at each dot, and the the solid lines are visual guides. Here $B_z = 2$ kG and $L_p^* = 48$ cm.

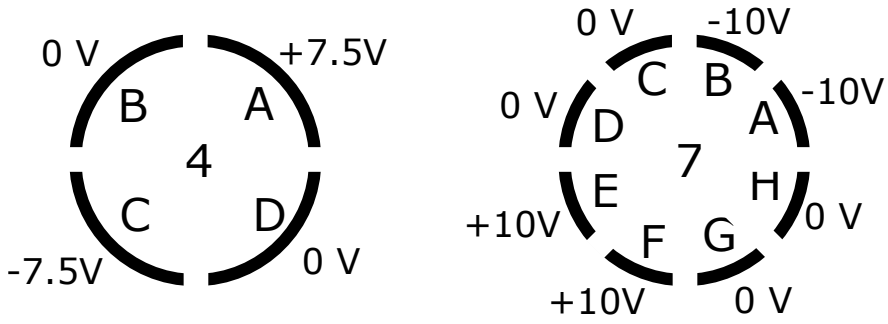

Figure 4.2: Voltages applied to sectored electrodes 4 and 7 to create an electrostatic tilt asymmetry.

$\approx 50\%$ while H_{Tot} remains constant within 1%. This experiment highlights a characteristic feature of nonneutral plasmas which is that the electrostatic energy is much larger than the thermal energy and therefore small fractional changes in the potential energy can result in large fractional changes in temperature.

During the expansion H_{Tot} is conserved within the measurement accuracy of the experiment, indicating that external heating and cooling mechanisms are negligible for early times with $B_z = 2$ kG. The conservation of energy shows that there is a clear conversion of electrostatic energy into thermal energy during the expansion. Furthermore, the increase in $\langle r^2 \rangle$ indicates that there is plasma expansion caused by intrinsic external asymmetries.

The Joule heating from expansion is largest at the radial edge of the plasma where the radial electric field is largest. The relatively uniform $T(r)$ at 1.5 s indicates that the local heating is small compared to the radial heat transport rate, such that the temperature increase at the edge of the plasma is spread throughout the plasma.

4.3 Radial Expansion from Applied Asymmetries

Now we apply asymmetric perturbations in the form of an "electrostatic tilt" to enhance the radial expansion rate, which in turn increases the amount of Joule heating. The plasma is confined between electrodes 1 and 10 with all other electrodes grounded. Initially all of the

Table 4.2: Integrals for radial expansion due to a $sin(\theta)$ asymmetry applied for a variable time. The total confinement time is 0.5 seconds and $B_z = 2$ kG, $L_p^* = 48$ cm.

Tilt Duration $[s]$	$\langle r^2 \rangle$ $[cm^2]$	H_T $[eV]$	H_ϕ $[eV]$	H_{Tot} $[eV]$
0.15	0.976	2.75	10.51	13.26
0.20	1.052	3.10	10.25	13.35
0.25	1.123	3.39	9.91	13.30
0.30	1.212	3.73	9.60	13.33

sectors of electrodes 4 and 7 are grounded, but 30 ms after the plasma is injected into the trap we apply voltages to some of the sectors, as shown in Fig. 4.2. These are calculated so as to best approximate $sin(\theta)$, given the individual sector areas. The electrostatic tilt is applied for a specific duration between 150-300 ms, and then all of the sectors are returned to ground. The plasma is further held until $t_c = 0.5$ s, at which time we measure $Q(r)$ and $T(r)$.

Fig. 4.3 shows the measured $Q(r)$ and $T(r)$ profiles from which H_ϕ, H_T and $\langle r^2 \rangle$ are calculated and given in Table 4.2. The tilt asymmetry results in a large temperature gradient across the plasma which indicates that the rate of expansion is fast compared to the radial heat transport time scale. Furthermore we observe that the thermal energy per particle H_T increases with increased tilt duration but the total energy of the plasma remains constant within 1% throughout the experiment indicating that the total energy is conserved while the electrostatic potential energy is converted into thermal energy. We note that at low magnetic fields, rapid expansion from asymmetry-induced transport can create large temperature gradients which are optimal for heat transport studies.

4.4 Cooling due to Cyclotron Radiation

For the next set of temperature measurements we increase the magnetic field to $B = 9$ kG and we measure the temperature profile at four confinement times, $t_c = 3.5$ s, 4.5 s, 6 s and 7.5 s. The plasma is confined between electrodes 4 and 8 giving a confinement length of $L_c = 17.5$ cm

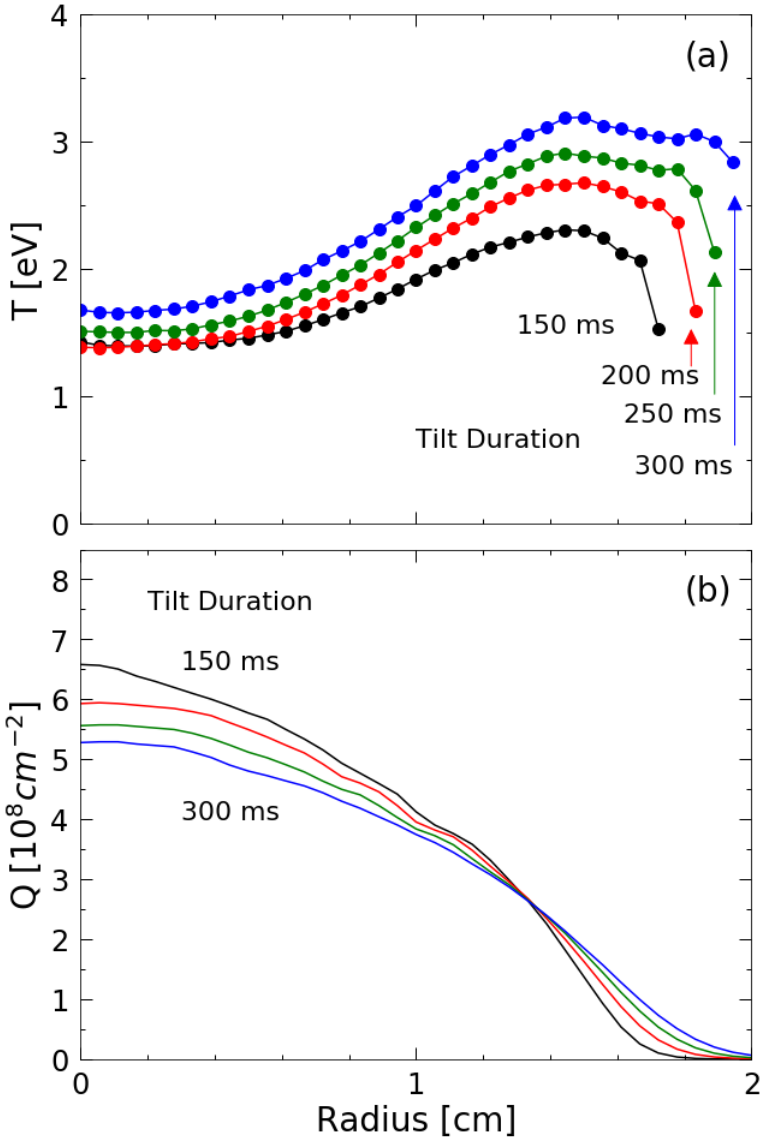

Figure 4.3: Temperature (a) and z-integrated density (b) profiles taken at a confinement time of 0.5 seconds with a $sin(\theta)$ electrostatic asymmetry applied for 150 ms (black), 200 ms (red), 250 ms (green), 300 ms (blue). Joule heating is strongest at the edge of the plasma and the large temperature gradient persists because the plasma is expanding fast compared to the heat transport time scale. Here $B_z = 2$ kG and $L_p^* = 48$ cm.

Table 4.3: Integrals for cooling due to cyclotron radiation. Here $B_z = 9$ kG and $L_p^* = 13$ cm.

Confinement Time $[s]$	$\langle r^2 \rangle$ $[cm^2]$	H_T $[eV]$	H_ϕ $[eV]$	H_{Tot} $[eV]$
3.5	0.768	1.98	13.57	15.55
4.5	0.763	1.63	13.66	15.29
6.0	0.762	1.21	13.61	14.82
7.5	0.766	0.90	13.76	14.66

and an effective plasma length of $L_p^* = 13$ cm. Electrodes 1-3, 5-7, 9-10 and all of the sectors of electrode 7 are grounded and no external asymmetries are applied. Fig. 4.4 shows the measured $T(r)$ as well as the time dependence of H_T. At a magnetic field of $B = 9$ kG the expansion rate is dramatically reduced which reduces the rate at which electrostatic energy is converted into thermal energy from Joule heating. The reduction of the expansion rate is evident in the constancy of $\langle r^2 \rangle$ over time and the lack of change in the $Q(r,t)$ profiles over time (not shown).

The dominant effect is a significant cooling of the plasma due to cyclotron radiation. The predicted cyclotron cooling time at this magnetic field is $\tau_r = 4.78$ s. An exponential fit (shown in Fig 4.4(b)) to H_T as a function of t_c gives a measured cyclotron cooling time of $\tau_r = 4.96$ s which is within 5% of the predicted value. During the evolution, H_ϕ remains constant within the measurement accuracy of the experiment and therefore H_{Tot} decreases due to the drop in H_T from cyclotron radiation.

In addition to measuring $T(r,t)$ we have also measured the temperature at $r = 0$ using the collector plate to obtain $T_{CP}(t)$. The $T_{CP}(t)$ measurement is performed by rotating the collector plate to block the axial path of the ejected electrons and then measuring the voltage induced across an RC circuit connected to the collector plate. The on-axis temperature is determined from the escaping charge signal using the simplified E92 technique with finite-length corrections that include modifications discussed by H06 and corrections due to adiabatic axial expansion. The results of the on-axis temperature measurement method are denoted by the square symbols in Fig 4.4(a). The error bars represent the standard deviation calculated from approximately 10

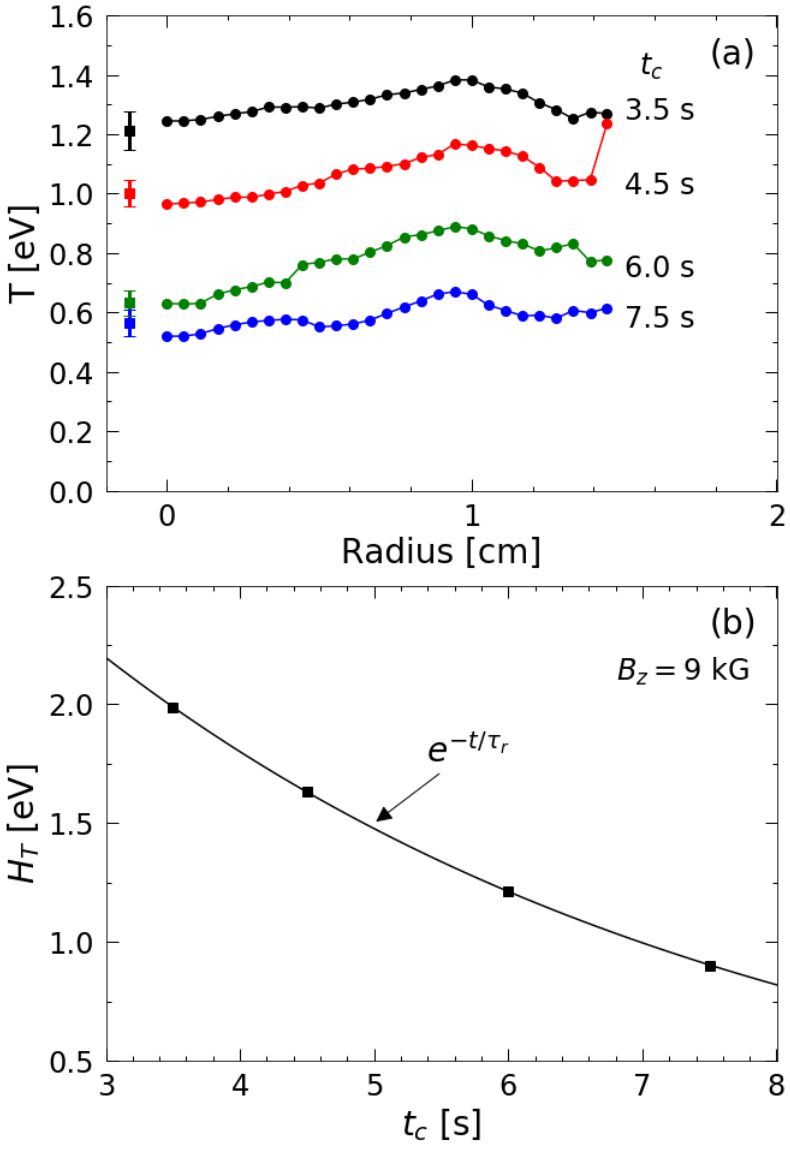

Figure 4.4: (a) Radial temperature profiles $T(r,t_c)$ (circles) and $T_{CP}(t_c)$ (square) measurements taken at confinement times of 3.5-7.5 sec with a magnetic field $B = 9$ kG. (b) $H_T(t_c)$ (squares) with an exponential fit yielding a cyclotron cooling time of $\tau_r = 4.96$ s.

repeated measurements. Comparison of the $T_{CP}(t)$ results with the $T(r)(t)$ profile in the vicinity of $r = 0$ cm show that there is good agreement between the two techniques.

4.5 Separatrix-Crossing Dissipation

In this section we present an example of separatrix-crossing dissipation which causes radially localized heating within the plasma column and is therefore an excellent candidate for creating temperature gradients to study radial heat transport. Generally speaking a separatrix is a division in two regions of phase space where the behavior in the two regions can be markedly different. The classic example in plasma physics is the separatrix between trapped and passing particles that occurs in the potential of a large ampitude plasma wave [76]. In many plasma physics devices, separatrices can arise from electric and magnetic fields produced either by the plasma or by external sources. In nonneutral plasmas, trap separatrices are created by applying external electric and magnetic perturbation that create locally trapped populations of particles. Experiments on nonneutral plasmas utilizing trapping separatrices have resulted in studies of chaotic particle transport [77, 78] and novel trapped particle modes [79, 80].

Here we demonstrate collisional heating that arises from the application of an electrostatic squeeze to the center of the plasma column while simultaneously oscillating the plasma column axially through the squeeze potential. Recent theory [81] and experiments [82] have characterized the heating that arises from separatrix-crossing dissipation when the plasma column is repeatedly forced through the squeeze potential. This type of heating is colloquially referred to as "sloshing through a squeeze" and some of the experimental parameters have inherited names from this colloquialism which are useful descriptors.

The conceptual model of sloshing through a squeeze is shown in Fig. 4.5. We begin with a quiescent plasma confined between two electrodes with the rest of the electrodes grounded. We then apply a squeeze potential to the axial midpoint of the plasma with a voltage of, V_{sq}, which is a

negative potential for electrons but would be positive for positive nonneutral plasmas. Depending on the strength of V_{sq}, the axial velocity space distribution function at any given radius will be divided into trapped and passing particles. The passing particles have sufficient kinetic energy that they can surmount the electrostatic barrier created by V_{sq} whereas the trapped particles do not have sufficient energy to overcome the barrier and are therefore trapped on either side of the squeeze. We then force the plasma column through the squeeze potential by synchronously increasing the confinement potential on one confinement electrode while decreasing the confinement potential on the other confinement electrode. Oscillating the confinement potentials in this manner causes the plasma to shift axially.

The oscillation of the end confinement potentials is calibrated in such a way so that the overall length of the plasma columns remains unchanged (See Appendix B). For the passing particles, the length of their bounce orbit remains unchanged during the sloshing; however the bounce orbits of the trapped particles experience compression and expansion during the sloshing of the plasma column as conceptually shown in Fig. 4.5. The result is a discontinuity in the particle distribution function which is relaxed by collisions as particles go from trapped to untrapped. The collisions result in irreversible heating of the plasma column that is largest where the thermal energy of the plasma is approximately equal to the energy barrier created by the squeeze separatrix. Therefore by increasing the voltage of the squeeze potential we can move the peak of the heating profile closer towards the radial center of the plasma. The sloshing is characterized by a frequency of the axial sloshing, f_{sl}, a voltage amplitude of the sloshing, V_{sl}, and a duration for the sloshing oscillations, t_{sl}. The squeeze potential is applied synchronously with the start of the axial sloshing and the squeeze is applied for the same duration as the sloshing.

The experiment is conducted at $B_z = 12$ kG and the plasma is confined between electrodes 2 and 10 giving a confinement length of $L_c = 38.5$ cm and an effective plasma length of $L_p^* = 34$ cm. Electrodes 3-9 are grounded for the duration of the experiment except for electrode 6. Electrode 6 is initially grounded but then at the appropriate time, V_{sq} is applied to this electrode.

Before applying the squeeze and sloshing we measure the radial density and temperature profile which are shown as the black curves in Fig. 4.6. We then apply separatrix-crossing dissipation to heat the plasma by applying a squeeze to electrode 6 and then we slosh the plasma through the squeeze with a sloshing frequency of $f_{sl} = 100$ kHz, a sloshing amplitude of $V_{sl} = 40$ V and we slosh the plasma for a duration of $t_{sl} = 125$ ms (12,500 cycles). After the sloshing cycles are complete we remove the squeeze potential and measure the radial temperature profile. We perform the experiment three times at squeeze voltage of V_{sq} =-10, -25 and -35 V.

Fig. 4.6 shows the measured $Q(r)$ and $T(r)$ profiles at each V_{sq}. We observe that for the smallest squeeze potential V_{sq} =-10 V, the heating is largest at the radial edge of the plasma which is expected since the electrostatic barrier does not penetrate deep into the plasma. For an intermediate voltage of V_{sq} =-25 V, the heating is localized to an intermediate radius in the plasma column. For a large squeeze voltage of V_{sq} =-35 V, the squeeze potential is approximately equal to the on-axis plasma potential and the plasma is almost cut in half. The heating from the separatrix-crossing dissipation at V_{sq} =-35 V is largest at the radial center of the plasma and we observe that a large temperature gradient has been created. The temperature gradient from the large squeeze is an ideal initial condition for studying radial heat transport. Although, studies of separatrix-crossing dissipation are interesting in of themselves, in the next chapter on heat transport experiments we use separatrix-crossing dissipation as a method for creating large temperature gradients at high magnetic field.

4.6 Acknowledgments

This chapter, in part, is currently being prepared for submission for publication. K. A. Thompson, A. A. Kabantsev, N. Panzeri and C. F. Driscoll. The dissertation author was the primary investigator and author of this material.

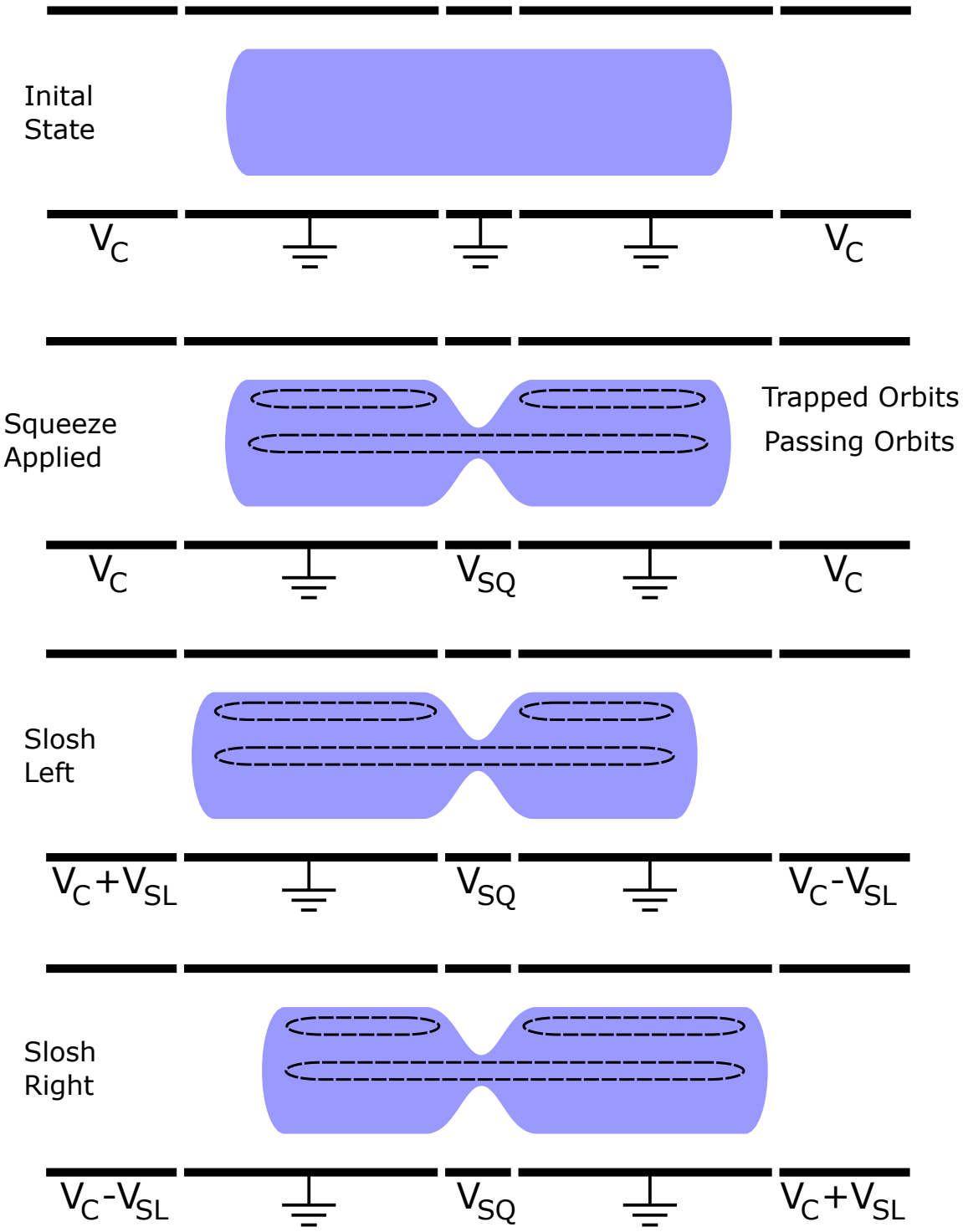

Figure 4.5: Conceptual model of manipulations performed to apply radially localized heating due to separatrix-crossing dissipation.Typical voltages are $V_c = -100$ V, $V_{sl} \approx 40$ V, and $V_{sq} \approx -30$ V.

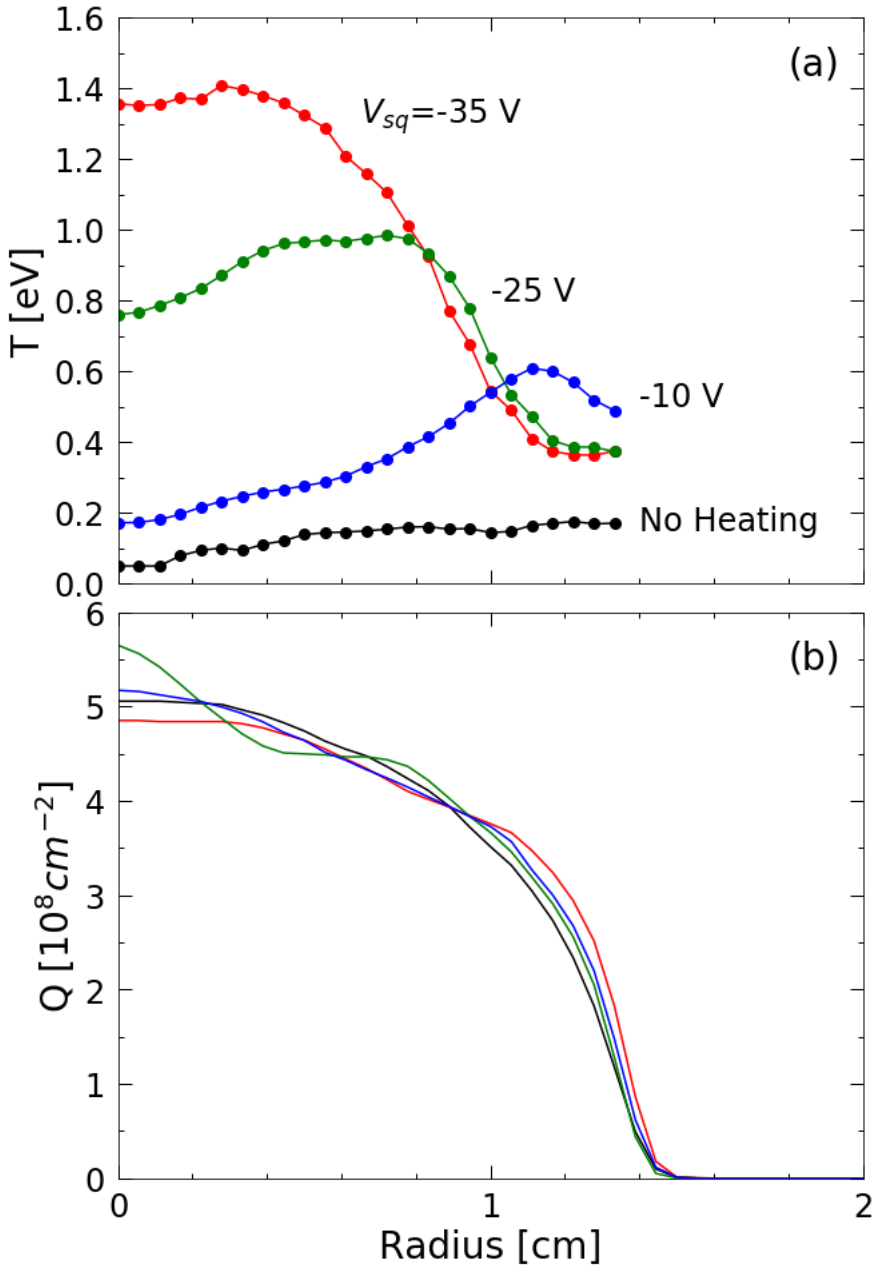

Figure 4.6: Heating from separatrix-crossing dissipation. Temperature (a) and z-integrated density (b) profiles for three different squeeze voltages. The "No Heating" data is the initial condition before the squeeze and sloshing is applied. The sloshing amplitude and frequency are the same for all cases.

Chapter 5

Measurement of Cross-Magnetic Field Thermal Diffusivity

5.1 Overview

In this chapter we present measurements and analysis of radial heat transport in a pure electron plasma. Measurement of radial heat transport is made possible by the development of the method presented in Chapter 3 for obtaining accurate radial temperature profiles. Furthermore, the exploration of possible heating and cooling mechanisms in Chapter 4 has identified asymmetry-induced expansion as a mechanism for creating large radial temperature gradients at low magnetic field and separatrix-crossing dissipation for creating temperature gradients at high magnetic field. The formation of these temperature gradients are necessary for studying diffusive heat transport.

Our measurements show that the heat transport is governed by a convection-diffusion equation that includes source terms consisting of Joule heating and cyclotron cooling. The diffusive component of the heat transport is shown to be well described by a local Fick's law equation and analysis of the diffusive heat flux allows for an accurate calculation of the thermal diffusivity which is then compared to two theoretical predictions for the thermal diffusivity.

The first prediction of the diffusivity is calculated from considering classical short-range collisions, which are defined by an impact parameter up to the cyclotron radius, $b < \rho < r_c$. The second prediction for the thermal diffusivity is calculated from including long-range collisions with impact parameter up to the Debye length, $r_c < \rho < \lambda_D$. The relative importance of classical short-range collisions versus long-range collisions depends on the relative sizes of r_c and λ_D. For neutral plasmas, we must consider the relative sizes of both the ion cyclotron radius r_{ci} and the electron cyclotron radius r_{ce} compared to the electron Debye length λ_{De}.

The significant majority of neutral laboratory plasmas, astrophysical plasmas and fusions plasmas are in the regime where $\lambda_{De} < r_{ci}, r_{ce}$ in which case short-range collisions dominate. Long-range collisions are important when the length scale ordering is reversed, i.e. $r_c < \lambda_D$. Regions of the interstellar medium and well as some neutral laboratory and fusion plasmas can be in the regime where $r_{ce} < \lambda_{De} < r_{ci}$ in which case long-range collisions are important in the collisional transport properties of the "electron channel". Long-range collisions may become increasingly important in fusion studies as future tokamaks strive for larger magnetic fields and higher temperatures. Nonneutral plasmas, including electron, positron and ion plasmas, are naturally in the regime where $r_c < \lambda_D$, and this makes these systems ideal for studying long-range collisional transport.

The prediction for the classical thermal diffusivity scales as $\chi_c \propto nB^{-2}T^{-1/2}$ whereas the long-range thermal diffusivity scales as $\chi_L \propto T^{-1/2}$ (See Table (1.1)). A striking aspect of the long-range thermal diffusivity is that χ_L is independent of both magnetic field and density. Our experiments are performed over a wide range of magnetic fields, i.e. $1 < B_z < 13$ kG giving a predicted $10^3 < \chi_L/\chi_C < 10^5$.

Over this range, the plasma dynamics exhibit qualitatively different behavior. At high magnetic field, $B > 4$ kG, the plasma expands slowly leading to a negligible Joule heating rate but there is significant cyclotron cooling. At low magnetic fields, $B < 4$ kG, cyclotron cooling is small but the plasma expands rapidly resulting in a large Joule heating rate. The measured thermal

diffusivity is found to be in excellent agreement with the diffusivity predicted from long-range collisions and we verify the magnetic-field-independence of the thermal diffusivity.

As indicated in Table (1.1), long-range heat transport is not expected to be enhanced in the high rigidity regime, that is $\mathcal{R} > 1$. Previous experiments on collisional transport in nonnenutral plasmas have measured an enhanced radial transport for particle diffusion and viscosity in the 2D bounce-averaged regime where the plasma rigidity is large, $\mathcal{R} > 1$. The conceptual reason for the enhanced transport coefficients is that at high rigidity, particles bounce axially many times before completing a drift orbit around the center of charge. Therefore two particles on different magnetic field lines that are separated up to a distance of the Debye length can undergo multiple correlated collisions before being sheared apart by rotation which leads to an enhancement of the radial particle and momentum transport.

Experiments in the 2D bounce-averaged regime on particle diffusion and viscosity are in qualitative agreement with the theoretical perspective however quantitatively there is disagreement especially regarding the enhancement of viscosity. The same theoretical perspective that leads to enhanced particle diffusion and viscosity coefficients in the 2D bounce-averaged regime expects that there is no enhancement to the thermal diffusivity. However, the previous measurements of thermal diffusivity on pure ion plasmas were performed in the low rigidity regime, $\mathcal{R} < 1$, and therefore the thermal diffusivity was not measured in the high rigidity regime. The experiments detailed in this chapter are performed over a range of rigidities from $1 < \mathcal{R} < 60$ and are the first measurements of heat transport in the high rigidity 2D bounce-averaged regime. Our measurements confirm the theory perspective; unlike the enhancement that is exhibited for particle diffusion and viscosity, our measurements indicate that the thermal diffusivity is independent of the plasma rigidity and no enhancement is observed.

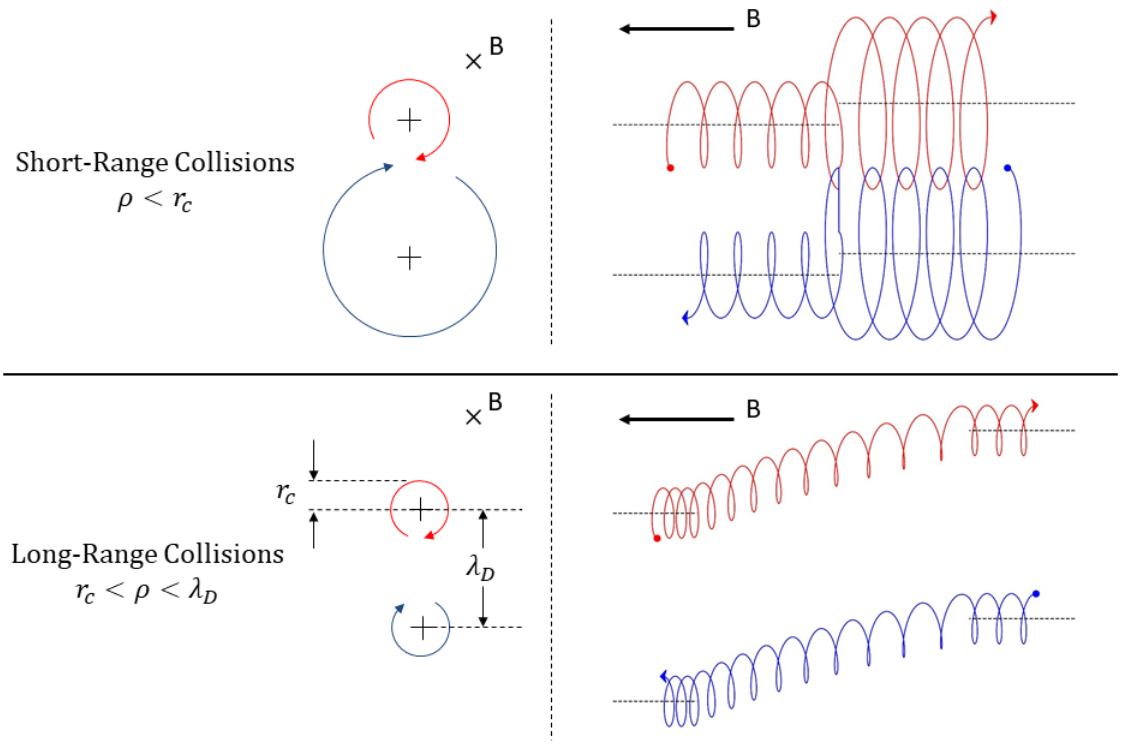

Figure 5.1: Inter-particle short-range collisions occur for impact parameters up to the cyclotron radius $b < \rho < r_c$ and can scatter perpendicular and parallel energy. Long-range collisions occur for impact parameters up to the Debye length $r_c < \rho < \lambda_D$ and cause the exchange of parallel energy only.

5.2 Background

We previously we have mentioned the difference between transport due to classical short-range collisions and long-range collisions which is succinctly embodied in Table (1.1). We now discuss these types of collisions in detail and their application to heat transport. The two different types of collisions are shown conceptually in Fig. 5.1. Classical short-range collisions have collisional impact parameters, ρ, that are between the distance of closest approach and the cyclotron radius, that is $b < \rho < r_c$. Theory treats the short-range collisions as local Boltzmann collisions which scatter the velocity vectors of the particles causing r_c-size diffusive steps and randomization of thermal energy. These collisions are typically dominant when $\lambda_D < r_c$. However, when $r_c < \lambda_D$, then long-range collisions with impact parameters up to the Debye length, $r_c < \rho < \lambda_D$, become the dominate collisional transport mechanism. During a long-range interaction, the mutual electric field E_{12} between the particles causes $E \times B$ drifts in (r, θ), leading to enhanced particle diffusion and viscosity. Also, E_{12} leads to a sharing of axial kinetic energy between particles, causing the thermal diffusivity χ_L of interest here.

The classical thermal diffusivity is given by

$$\begin{aligned} \chi_c &= \nu_{ee} r_c^2 \\ &\approx (9.06 \times 10^{-4}\ \mathrm{cm^2\ s^{-1}}) \left(\frac{T}{1\ \mathrm{eV}}\right)^{-1/2} \left(\frac{B_z}{1\ \mathrm{kG}}\right)^{-2} \left(\frac{n}{10^7\ \mathrm{cm^{-3}}}\right) \\ &\quad \times \left(1 + 0.10 \ln\left[\left(\frac{T}{1\ \mathrm{eV}}\right)^{3/2} \left(\frac{B_z}{1\ \mathrm{kG}}\right)^{-1}\right]\right) \end{aligned} \tag{5.1}$$

Classical collisions can exchange energy in both the perpendicular and the parallel degrees of freedom.

Long-range collisions on the other hand can only exchange energy associated with the parallel degree of freedom. During the long-range collisions the cyclotron action is a preserved

adiabatic invariant because the particles execute many cyclotron orbits in the time it takes for a long-range collision to occur. Referring to the equation for the cyclotron action, Eq. (2.34), the constancy of the cyclotron action in a uniform magnetic field implies that the perpendicular velocity and hence the perpendicular energy remains constant. The long-range thermal diffusivity is given by

$$\begin{aligned} \chi_L &= 0.49\ (n\bar{v}b^2)\ \lambda_D^2 \\ &\approx (0.236\ \mathrm{cm}^2\ \mathrm{s}^{-1})\left(\frac{T}{1\ \mathrm{eV}}\right)^{-1/2} \end{aligned} \tag{5.2}$$

Since the experiments are performed over a wide range of magnetic fields where the dynamics vary considerably, it is useful to compare the expected time scales for thermal diffusion to the other relevant dynamical time scales such as the cyclotron cooling time scale and the radial expansion time scale. The temperature gradients that are created from asymmetry-induced expansion and separatrix-crossing dissipation span the entire radius of the plasma and have a thermal gradient length scale, $L_T^{-1} = (1/T)(\partial T/\partial r)$, that is approximately $L_T = 0.5$ cm. The thermal diffusive time scales are then given by $\tau_C = L_T^2/\chi_C$ for short-range collisions and $\tau_L = L_T^2/\chi_L$ for long-range collisions.

The thermal diffusion time scales are compared with other dynamical time scales in Fig. 5.2 where we have used the empirical result for $\nu_{\langle r^2\rangle}$ (Eq. (2.26)) with $V_a = 1$ V, $T = 1$ eV and $L_p = 35$ cm. At low magnetic field $B_z \approx 1$ kG the radial expansion time $\nu_{\langle r^2\rangle}$ is comparable to τ_L, so the plasma expands rapidly on the time scale for thermal diffusion to relax temperature gradients. At large magnetic field $B_z \approx 10$ kG, the expansion time is slow, but the cyclotron cooling time τ_r is now comparable to τ_L.

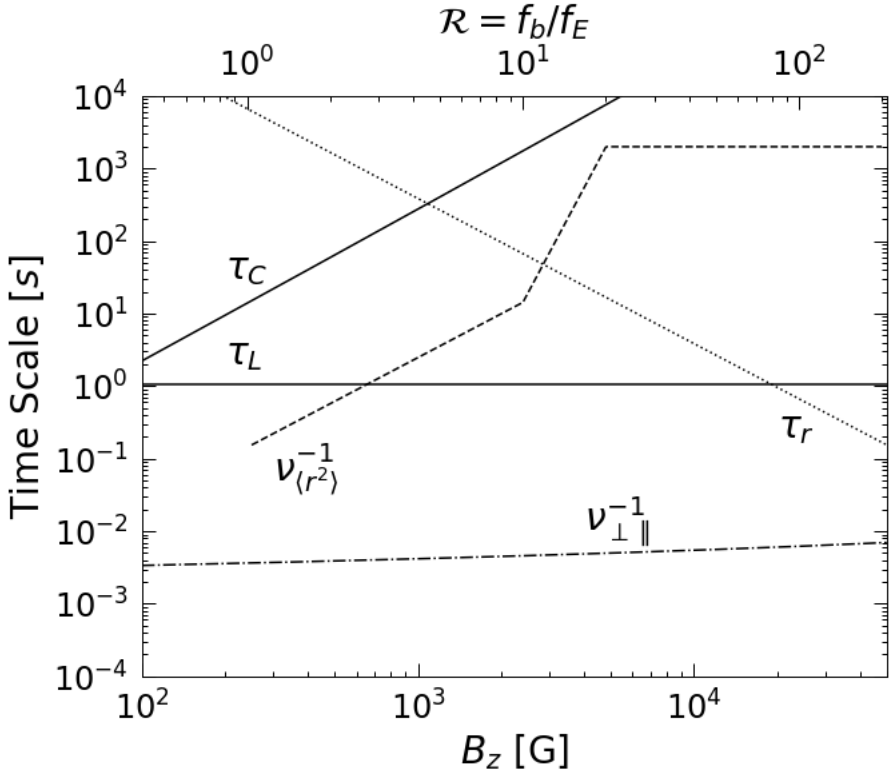

Figure 5.2: Time scales governing the dynamics as a function of the magnetic field B_z and plasma rigidity $\mathcal{R}$. Times scales and $\mathcal{R}$ are evaluated at $T = 1$ eV, $n = 10^7$ cm^{-3}, $L_p = 35$ cm and $L_T = 0.5$ cm. τ_L and τ_C are the thermal diffusion time scales due to long-range and short-range collisions, respectively. $\nu^{-1}_{\perp\parallel}$ is the temperature anisotrophy relaxation time scale, $\nu^{-1}_{\langle r^2\rangle}$ is the radial expansion time scale, and τ_r is the cyclotron cooling time. At low magnetic fields $\tau_L \sim \nu^{-1}_{\langle r^2\rangle}$ whereas at high magnetic fields $\tau_L \sim \tau_r$, and at all magnetic fields $\tau_L < \tau_C$.

5.3 Heat Transport Model

We describe the heat transport using fluid equations consisting of the density continuity equation and the Convection-Diffusion equation [83]

$$\text{Continuity} \qquad \frac{\partial n}{\partial t} + \nabla \cdot (n\mathbf{v}) = 0 \tag{5.3}$$

$$\text{Convection-Diffusion} \qquad \frac{\partial}{\partial t}\left(\frac{3}{2}nT\right) + \nabla \cdot \left(\frac{3}{2}nT\mathbf{v} + \mathbf{\Gamma}_\chi\right) = q_s \tag{5.4}$$

where $\mathbf{v}$ is the fluid velocity, q_s represents the sources and sinks of thermal energy and we identify the particle flux as $\Gamma_m = n\mathbf{v}$ in Eq (5.3). The continuity equation Eq.(5.3) arises from the conservation of particles, and the equation does not include any source or sink terms; if appropriate, these could take the form of a source of electrons from ionization of the background gas or a sink of electrons from loss of particles from the trapping region. The conservation of the total number of particles is verified within the accuracy of the experiment.

The second term on the left-hand side of Eq. (5.4) is the divergence of the heat flux. The heat flux consists of two terms; a convective heat flux and a diffusive heat flux. The convective heat flux, given by $3/2nT\mathbf{v}$, accounts for the transport of energy that is carried by a plasma fluid element as it moves with velocity $\mathbf{v}$. The second term is the diffusive heat flux $\mathbf{\Gamma}_\chi$ which represents the flow of heat down a temperature gradient due to particle collisions causing random exchanges of energy. The convective heat flux is relevant where there is bulk fluid flow of the plasma, whereas the diffusive heat flux is applicable whenever there is a temperature gradient within the plasma.

We have represented the energy density at each point in the plasma as the thermal energy density $\frac{3}{2}nT$, and we have neglected the energy density from the bulk flow of the fluid element. For nonneutral plasmas with densities that are far from the Brillouin density limit, the kinetic energy is negligible compared to the thermal and electrostatic energies [84]. That is, the kinetic

contribution to the total energy can be neglected in the same fashion that the kinetic component of the canonical angular momentum is neglected as in Eq. (2.24).

In many studies of nonneutral plasmas, particularly at high magnetic field, the time scale for plasma expansion $\nu_{\langle r^2\rangle}^{-1}$ is large compared to the time scale of the dynamics that are being studied, i.e. the plasma does not expand radially on the time scale of the dynamics of interest. In this situation, the plasma is well described by $E\times B$ drift dynamics which is incompressible, $\nabla\cdot\mathbf{v}=0$. However, for the experiments that we perform at low magnetic field, $\nu_{\langle r^2\rangle}^{-1}$ is comparable to the predicted long-range diffusive heat transport time scale, τ_L, and therefore the diffusive transport of thermal energy occurs on a similar time scale as the convective heat transport (See Fig 5.2). Therefore the dynamics are not incompressible due to the radial expansion of the plasma.

We do assume that the plasma is azimuthally symmetric, and that there is no axial fluid flow. Futhermore we assume that there is no heat flux in the axial or azimuthal directions. The fluid velocity is then $\mathbf{v}=(v_r(r),v_\theta(r),0)$, the diffusive heat flux is $\mathbf{\Gamma}_\chi=(\Gamma_\chi(r),0,0)$. Eqs. (5.3-5.4) then become

$$\text{Continuity}\qquad \frac{\partial n_p}{\partial t}+\frac{1}{r}\frac{\partial}{\partial r}(rn_pv_r)=0 \tag{5.5}$$

$$\text{Convection-Diffusion}\qquad \frac{\partial}{\partial t}\left(\frac{3}{2}n_pT\right)+\frac{1}{r}\frac{\partial}{\partial r}\left(r\frac{3}{2}n_pTv_r+r\Gamma_\chi\right)=q_s \tag{5.6}$$

where we represent the density as n_p which is the axially averaged density (Eq. (2.5)). The transport equations given by Eq. (5.5) and Eq. (5.6) describe the radial flow of particles and heat. To calculate the thermal diffusivity, we proceed with the ansatz that the diffusive heat flux is locally described by a Fick's law equation [83]

$$\Gamma_\chi=-\kappa\nabla T\equiv-\frac{5}{2}n_p\chi\frac{\partial T}{\partial r} \tag{5.7}$$

where κ is the thermal conductivity defined as $\kappa\equiv\frac{5}{2}n_p\chi$ [24]. The validity of the assumption

that the diffusive heat flux can be represented by Fick's law will be verified during the analysis of the heat transport.

In order to calculate χ using Eq. (5.7) we are required to calculate the temperature gradient $\partial T/\partial r$ and the diffusive heat flux Γ_χ. Calculating the temperature gradient can be accomplished by taking radial derivatives of the measured temperature profiles. We derive an equation for Γ_χ by integrating Eq. (5.6).

$$\Gamma_\chi(r) = -\frac{3}{2} n_p T v_r + \frac{1}{r}\int_0^r r' dr' \left\{ -\frac{\partial}{\partial t}\left(\frac{3}{2} n_p T\right) + q_s \right\} \tag{5.8}$$

The last terms left to specify are v_r and q_s. We calculate v_r by taking the integral of the density continuity equation which gives

$$v_r(r) = \frac{\Gamma_m}{n_p} = -\frac{1}{r}\int_0^r r' dr' \frac{\partial n_p}{\partial t} \tag{5.9}$$

As previously stated, q_s represents the sources and sinks of thermal energy and it consists of two terms, Joule heating and cyclotron radiation,

$$q_s \equiv q_j + q_r \tag{5.10}$$

where q_j is the Joule heating rate and q_r is the cyclotron cooling rate. The Joule heating rate is given by

$$q_j = \boldsymbol{j} \cdot \boldsymbol{E} = e n_p v_r E_r \tag{5.11}$$

where $\boldsymbol{j}$ is the current density and E_r is the radial electric field calculated from Poisson's equation. $q_j > 0$ which causes the temperature of the plasma to increase. The magnitudes of v_r and E_r increase monotonically with radius and therefore we expect the Joule heating rate to increase with radius until it drops off abruptly at the radial edge of the plasma due to the drop off in n_p.

The cyclotron cooling rate is given by

$$q_r = \frac{3}{2} n_p \left(\frac{\partial T}{\partial t} \right)_{\tau_r} = -\frac{3}{2} n_p \frac{T}{\tau_r} \tag{5.12}$$

where $(\partial T/\partial t)_{\tau_r}$ indicates the time derivative of the temperature due to cyclotron cooling and is given by Eq. (2.20). The cyclotron radiation reduces the energy associated with all three degrees of freedom, $\nu_{\perp\parallel}^{-1} < \tau_r$, which accounts for the $3/2$ factor in Eq. (5.12).

5.4 Measurements of Cross-Magnetic-Field Heat Transport

In this section we discuss the density and temperature measurements from which the thermal diffusivity is determined. Experiments are performed at magnetic fields of $B_z = 1, 4, 9, 12$ and 13 kG. Referring to Fig. 5.2, there is a wide range of dynamics that occurs over the experimental range of magnetic fields. Therefore the methods used to create reproducible profiles vary as do the confinement times.

Accurate temperature measurements require excellent shot-to-shot reproducibility. In our experimental device, the shot-to-shot variation is $< 1\%$ for low magnetic fields $B_z \leq 2$ kG. However, the shot-to-shot variations in $n_p(r)$ are larger, at high magnetic fields apparently because the flows are more rigorously incompressible 2D $E \times B$ dynamics with less r_c-scale smoothing. Thus, at high magnetic field, curve fitting is performed to smooth the data and obtain the derivatives required to evaluate the thermal diffusivity using equations Eq. (5.7) and Eq. (5.8). The details of the curve fitting will be discussed at it arises.

5.4.1 Low Field Magnetic Field

We now describe heat transport measurements at a magnetic field of $B_z = 1$ kG, where cyclotron cooling is negligible but radial expansion and thus Joule heating is significant. The plasma is confined between electrodes 1 and 10 with electrodes 2-9 grounded giving a confinement

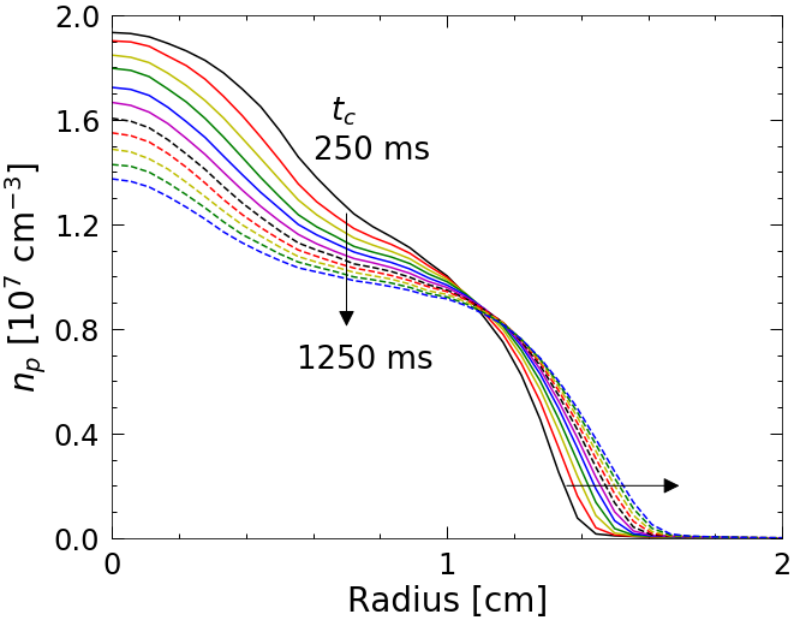

Figure 5.3: Density evolution at $B_z = 1$ kG. The plasma expands rapidly, resulting in an increase of the plasma radius and a decrease in the central density. Time steps between density profiles are 100 ms. Arrows show direction of temporal evolution.

length of $L_c = 52.5$ cm and an effective plasma length of $L_p^* = 48$ cm. No conditioning of the plasma profile is required; the plasma is simply injected into the trap and the ubiquitous $m = 1$ Diocotron mode that accompanies the end of the injection process is feedback damped within the first few milliseconds.

For the large plasma length of this experimental configuration, the rigidity is low in which case the radial expansion time scale is comparable to the thermal diffusive time scale $\nu_{\langle r^2 \rangle}^{-1} \sim \tau_L$ (See Fig. 5.2) . Therefore we expect that the localized Joule heating that results from the fast radial expansion will form radial temperature gradients that will not be immediately relaxed by thermal diffusion. Therefore we do not need to apply any external asymmetries as was the case in Sec. (4.3) where an electrostatic tilt was applied to induce fast radial expansion and create large temperature gradients. For the current experimental configuration we simply rely on the intrinsic trap asymmetries to induce rapid radial expansion and form temperature gradients.

The density $n_p(r,t)$ and temperature $T(r,t)$ evolutions are shown in Fig. 5.3 and Fig. 5.4

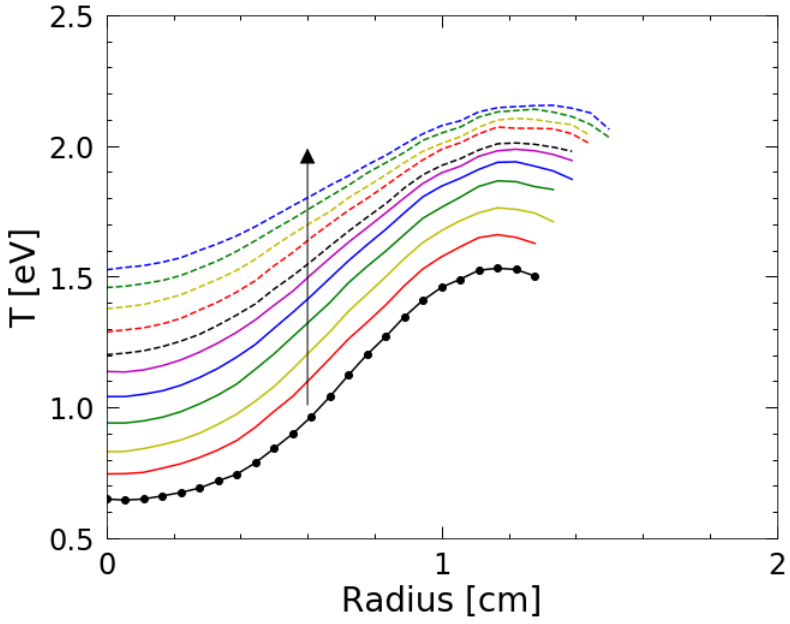

Figure 5.4: Temperature evolution at $B_z = 1$ kG. The temperature of the plasma increases due to Joule heating which is stronger at the radial edge, resulting in the large temperature gradient. Arrow shows direction of temporal evolution.

respectively. Note that in determining $n_p(r,t)$ we have used a Boltzmann-Poisson solver to determine $n(r,z,t)$ from the experimentally measured z-integrated density profiles, $Q(r,t)$. We then calculate the plasma lengths using Eq. (2.12) and finally we calculate the plasma density $n_p(r,t)$ using Eq (2.5).

The lowest curve in Fig. 5.4 exemplifies the grid spacing (circles) at which the temperature is measured using the technique detailed in Chapter 3; the solid lines in the graphs are visual guides, not curve fits. We perform the first density and temperature measurements at a confinement time of $t_c = 250$ ms and then we measure the density and temperature profiles every 100 ms until the final confinement time at $t_c = 1250$ ms.

The profiles show that the plasma expands significantly, and the temperature of the plasma increases strongly during the expansion. Furthermore we observe that there is a large temperature gradient that persists throughout the time evolution, and thereby provides an excellent experimental data set for calculating the thermal diffusivity. Note that the temperature measurement is not

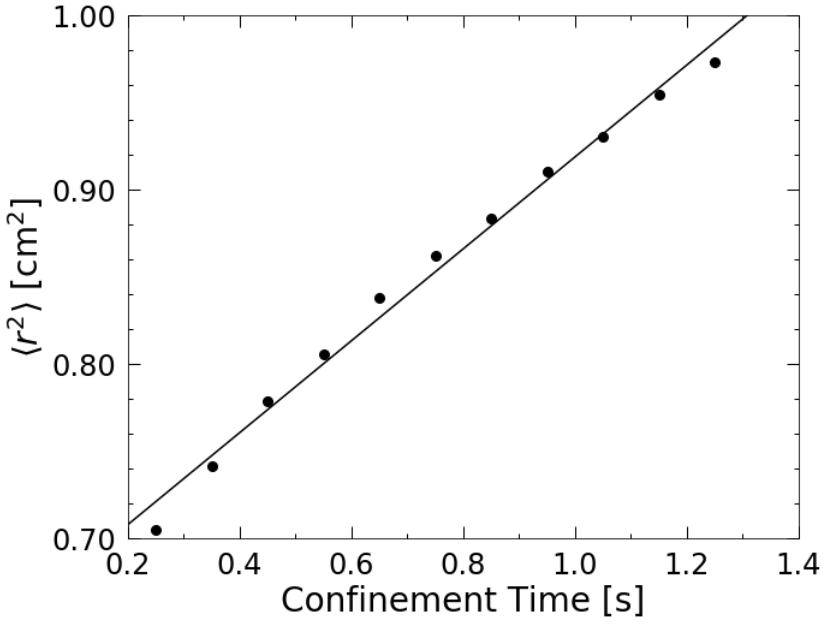

Figure 5.5: Evolution of the mean-square radius at $B_z = 1$ kG. The plasma expands radially resulting in an increase in the mean-square radius, $\langle r^2 \rangle$. The solid line is a linear fit to the data and is used to calculate an average expansion rate of $\nu_{\langle r^2 \rangle} = 0.78$ s^{-1}.

attempted for $n_p \lesssim 10^5$ cm^{-3}, so the radial extent of the measured temperature profiles increases as the confinement time increases.

Fig. 5.5 shows the mean-square radius during the evolution, and we observe that the increase in the mean-square radius is approximately linear. A linear fit to the time evolution of $\langle r^2 \rangle$ (solid line) gives an average expansion rate Eq (2.25) of $\nu_{\langle r^2 \rangle} = 0.78$ s^{-1} which is roughly consistent with the time scaling shown in Fig 5.2 for $\nu_{\langle r^2 \rangle}$.

Fig. 5.6 shows the total number of particles calculated using Eq. (2.4), and the solid line is a linear fit which yields a particle loss rate of $\partial N/\partial t = -2.3 \times 10^7$ s^{-1}. The total number of particles decreases by 1% over the duration of the experiment, barely above the shot-to-shot variations in our density measurements at this magnetic field. The small change in the total number of particles can be reasonably neglected, and we use the continuity equation without any source terms, Eq. (5.5).

Fig. 5.7 shows the energy balance during the expansion, where we have plotted the total

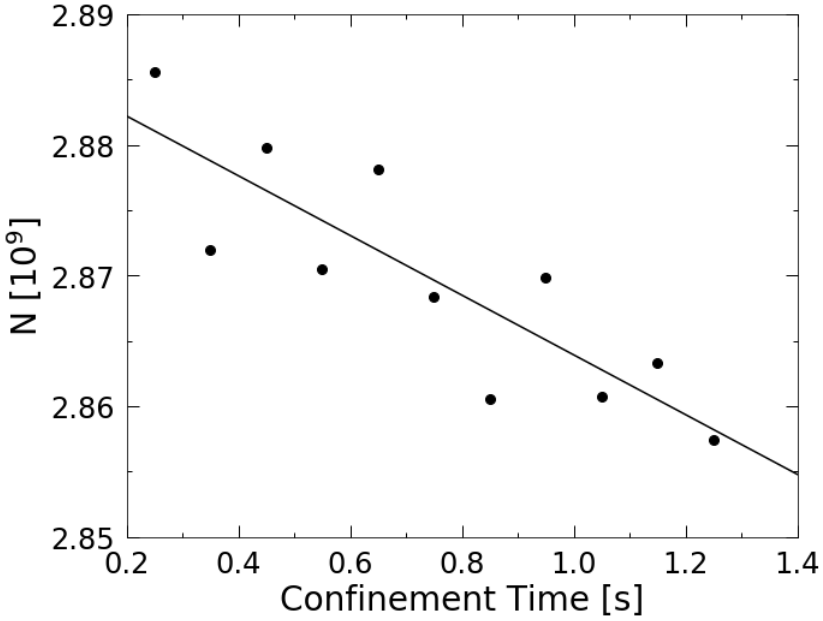

Figure 5.6: Evolution of the total number of particles at $B_z = 1$ kG. We observe a slight decrease of 1% of the total number of particles during the full evolution of the experiment. The solid line is a linear fit to the data and gives a loss rate of $\partial N/\partial t = -2.3 \times 10^7$ s^{-1}.

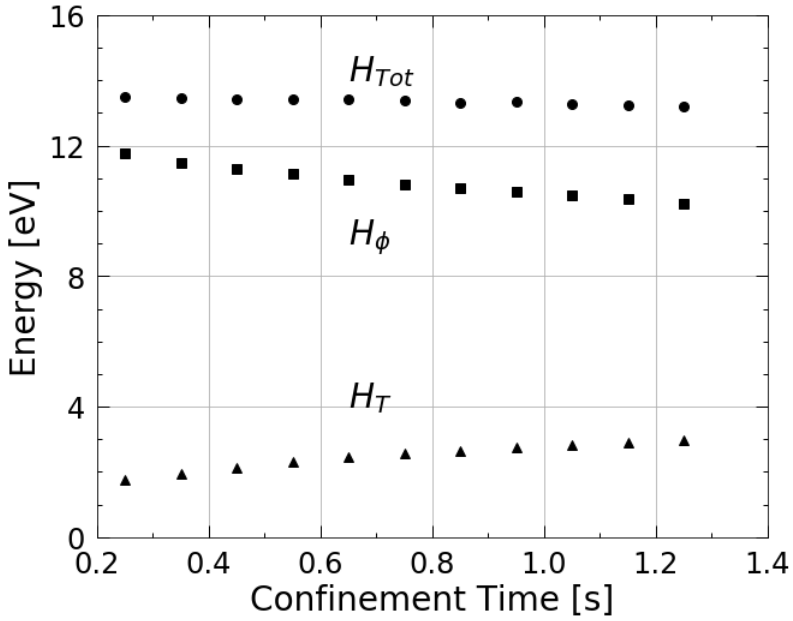

Figure 5.7: Evolution of the total energy per particle, H_{tot}, thermal energy per particle H_T and electrostatic energy per particle H_ϕ.

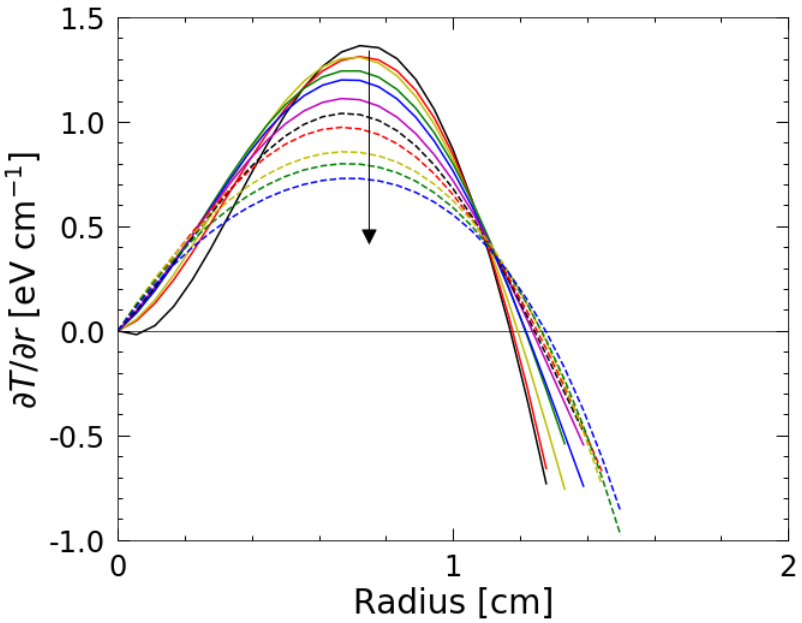

Figure 5.8: Radial temperature derivative determined by performing a polynomial fit to $T(r,t)$ and then taking the derivative of the polynomial with the condition that $\partial T \partial r = 0$ at $r = 0$. Arrow shows direction of temporal evolution.

energy per particle H_{Tot}, the electrostatic energy per particle H_ϕ, and the thermal energy per particle H_T. As expected, H_ϕ drops due to the decrease in the plasma potential while H_T increases due to Joule heating but H_{Tot} remains constant throughout the evolution to an accuracy of 2%. We then conclude that there is no transfer or removal of energy to or from the plasma from external sources. We are then confident that the total number of particles and the total energy are conserved during the evolution and we can proceed to calculate the thermal diffusivity using the model presented in Sec. (5.3).

For temporal derivatives, the data is sufficiently smooth that we use finite difference equations to evaluate $\partial n/\partial t$ and $\partial((3/2)nT)/\partial t$. In evaluating the radial temperature derivative we fit a 5th order polynomial to the $T(r,t)$ profiles and enforce the boundary condition that $\partial T/\partial r = 0$ at $r = 0$ due to symmetry. The polynomial fit is then used to calculate $\partial T/\partial r$ at each time step; $T(r,t)$ retains its original values and is not smoothed using the fit. Fig. 5.8 shows the calculated profiles for $\partial T/\partial r$.

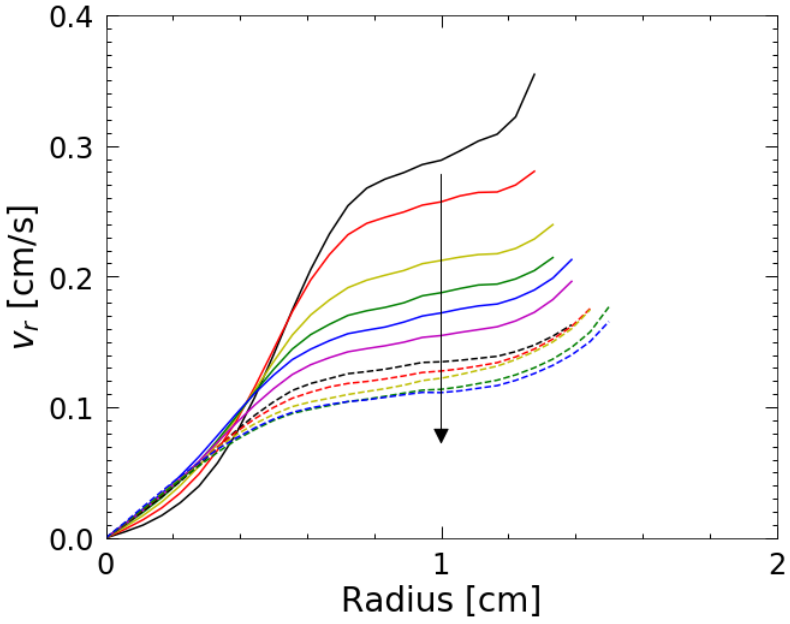

Figure 5.9: Temporal evolution of the radial velocity. Arrow shows direction of temporal evolution.

Fig. 5.9 shows the calculated profiles for v_r using Eq. (5.9). The calculations for v_r is stopped at the same radial extent as the associated temperature profile, since the low density values at large radii causes v_r to grow rapidly and the result is unreliable. The radial electric field is calculated from Poisson's equation and is shown in Fig. 5.10. As the plasma expands, the plasma potential decreases and subsequently the magnitude of the radial electric field decreases as well.

With the radial profiles for $v_r(r,t)$, $E_r(r,t)$ and $n_p(r,T)$, we now calculate the Joule heating rate, $q_j(r,t)$, using equation Eq. (5.11); and the results of the calculation are shown in Fig. 5.11. The Joule heating rate is largest near the outer radius of the plasma and there is no Joule heating near the center of the plasma. Despite the lack of Joule heating at the center of the plasma the temperature at the center of the plasma increases as seen in Fig. 5.4. The increase of the temperature at the center of the plasma is due to the diffusion of heat which flows from larger radii to smaller radii because of the positive temperature gradient.

The final term to calculate before we can calculate the diffusive heat flux is the convective

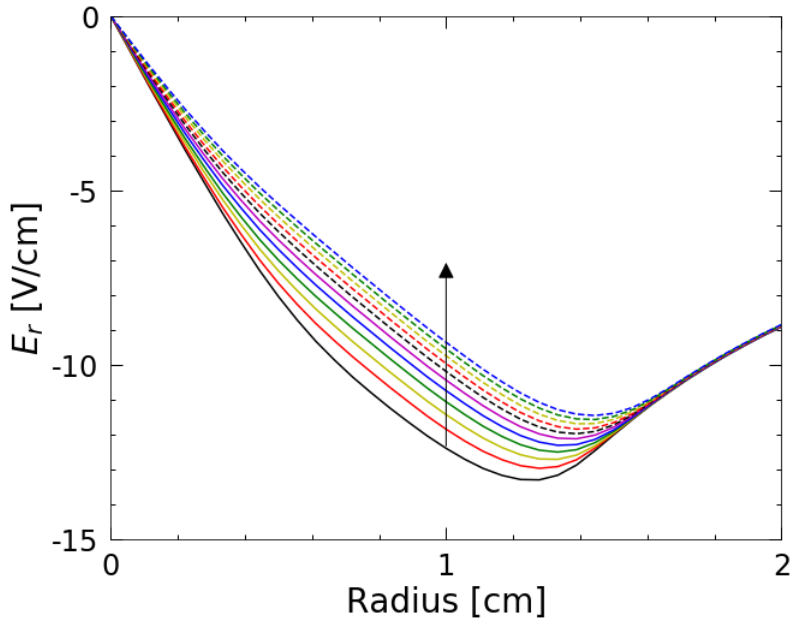

Figure 5.10: Radial electric field calculated from Poisson's equation and the density profiles n_p. Arrows show direction of temporal evolution.

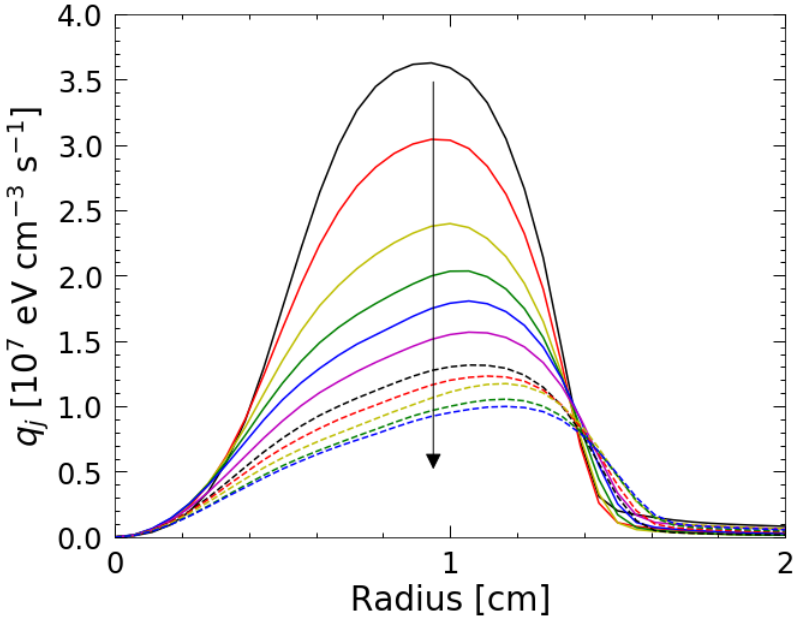

Figure 5.11: Joule Heat rate at $B_z = 1$ kG. The heating rate is largest at the outer radii due to the increase in the radial particle velocity and the radial electric field at the edge of the plasma. Arrow shows direction of temporal evolution.

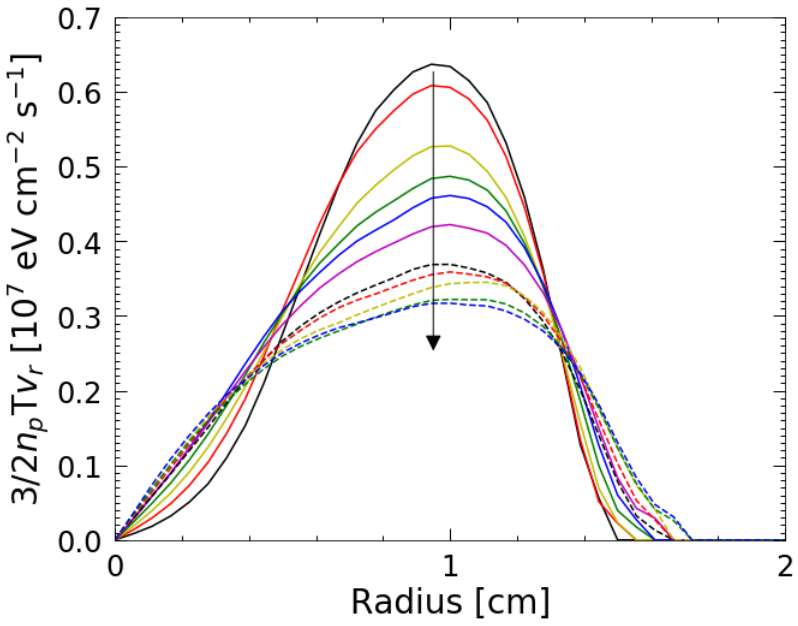

Figure 5.12: Convective heat flux at $B_z = 1$ kG. The largest convective heat flux occurs near the radial edge of the plasma due to the large radial velocity and higher temperature at larger radii. Arrow shows direction of temporal evolution.

heat flux. We calculate the convective heat flux by multiply the energy density by the radial velocity, and the results of this calculation is shown in Fig. 5.12. We now have all of the components required to calculate the diffusive heat flux, Γ_χ, using Eq. (5.8), the results of which are presented in Fig. 5.13.

Before proceeding to calculate the thermal diffusivity we must validate the applicability of the Fick's law equation for Γ_χ. That is, small convective cells in (r,θ) could "mix" the heat radially, even without causing a net v_r characteristic of simple convection. We verify Fick's law by observing the proportionality between the diffusive heat flux and the radial temperature gradient. However the diffusive heat flux is not simply proportional to the radial temperature gradient because the thermal conductivity can have density and temperature dependence, and the radial profiles do not have constant density nor constant temperature. Referring to the theoretical predictions for χ_C and χ_L we see that both diffusivities scale with temperature as $T^{-1/2}$. Furthermore, we note that χ_C scales with density as n^1 and that χ_L is independent of

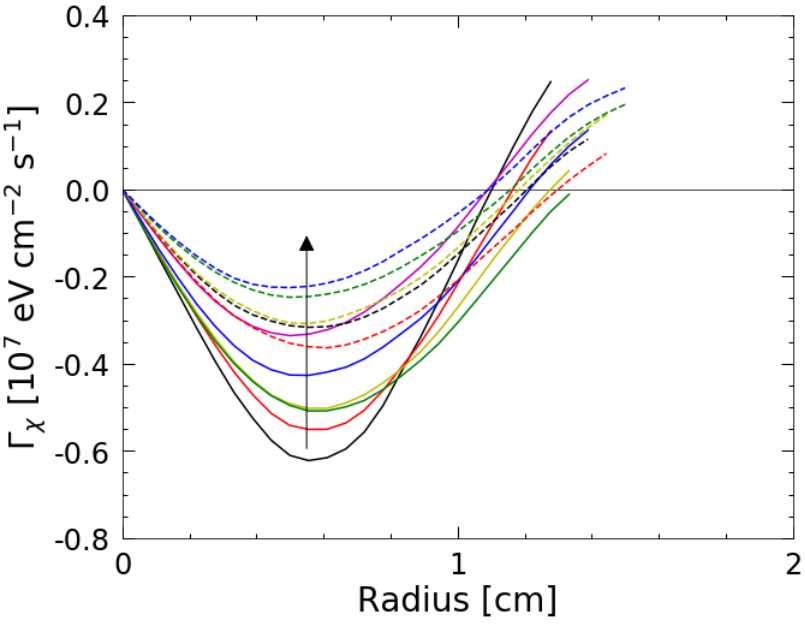

Figure 5.13: Diffusive heat flux at $B_z = 1$ kG. Arrow shows direction of temporal evolution.

density. If we proceed with the prediction that the measured thermal diffusivity is dominated by long-range collisions, then we can express Fick's law in the form $\Gamma_\chi \propto T^{-1/2} n^1 (\partial T/\partial r)$. We can then define the scaled diffusive heat flux as $\Gamma_\chi T^{1/2} n^{-1}$ which we expect to be proportional to the temperature gradient.

To verify the Fick's law relation we have plotted the negative of the scaled heat flux and the temperature gradient at a confinement time of $t_c = 650$ ms as shown in Fig. 5.14. Furthermore we have normalized the scaled heat flux and the temperature gradient to their respective maximum values to highlight the proportionality between the two quantities. The proportionality between the scaled heat flux and the temperature gradients is well-demonstrated in Fig. 5.14 giving credibility to the use of Fick's law to represent the diffusive heat flux.

When calculating the thermal diffusivity we restrict the analysis in radius to those radii in which the temperature gradient and the heat flux have the largest magnitude. This improves the signal-to-noise ratio and enables a more accurate calculation of χ using equation Eq. (5.7). The vertical dotted lines in Fig. 5.14 show the radial limits of the analysis region, i.e. we calculate the

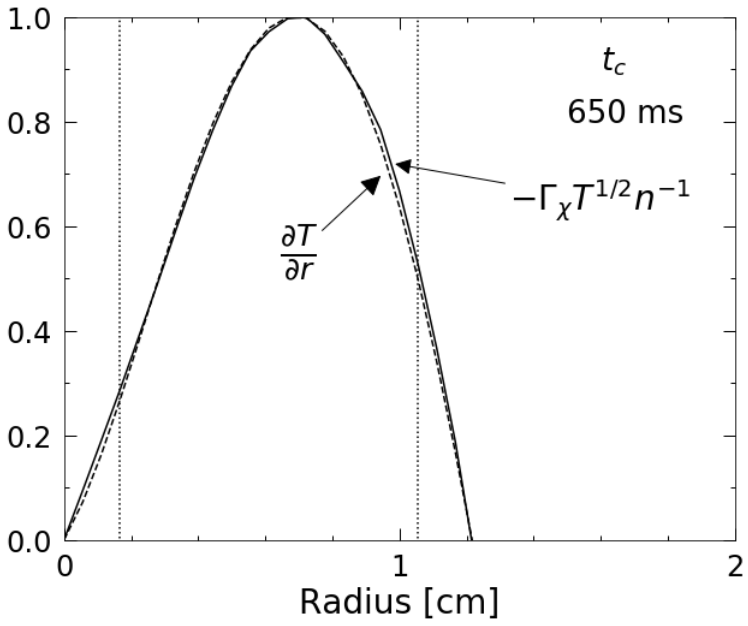

Figure 5.14: Scaled diffusive heat flux (solid) and temperature gradient (dashed) at $B_z =$ 1 kG. Both quantities are normalized to their respective maximum values to highlight the proportionality between the two quantities.

thermal diffusivity only using the radial points between the vertical dotted lines.

As an alternative verification of the applicability of Ficks' law, we plot, in Fig 5.15, the scaled heat flux versus the radial temperature gradient for all confinement times and for all radii in the analysis region, that is, in the region between the two vertical dotted lines in Fig. 5.14. Once again, we expect to see a linear relationship between the scaled heat flux and the temperature gradient. We perform a linear fit to the data in Fig. 5.15, and the fit is not constrained to pass through the origin. Nevertheless, we see that the linear fit does pass very close to the origin. If there was a non-zero intercept this could indicate that there is a non-diffusive heat flux that has yet to be accounted for.

We now proceed with the final step for calculating the thermal diffusivity by using Eq. (5.7). We then average over time at each radius and plot the average along with its standard deviation as the error bars at each radius in Fig 5.16. The diamonds represent points that are within the useful analysis region while the circles represent points outside of the analysis region that will be

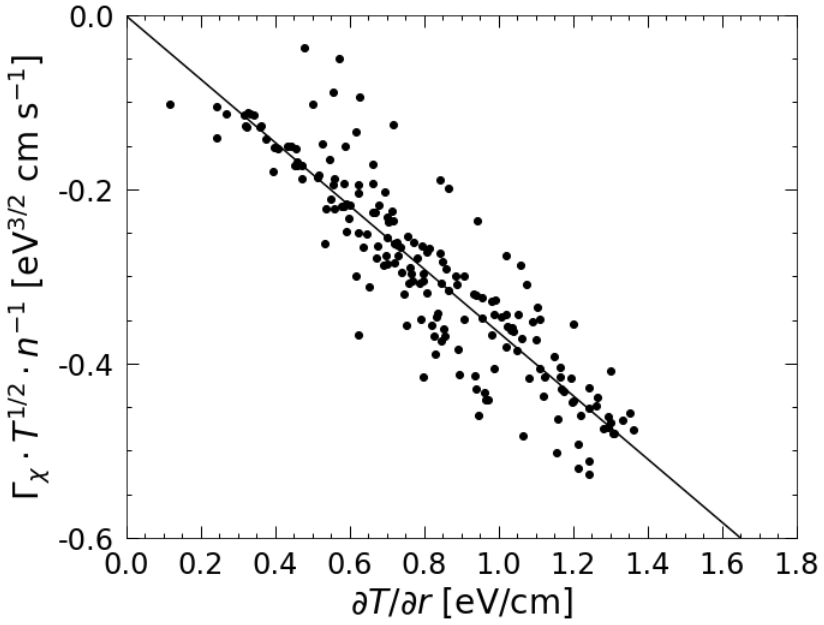

Figure 5.15: Scaled heat flux versus temperature gradient at $B_z = 1$ kG, the points represent all of the time steps at the subset of radii that are used to calculate the thermal diffusivity. The scaling is informed by the theoretical predictions and the scaling parameters are chosen so that the heat flux is proportional to the temperature gradient. The solid line is an unconstrained linear fit.

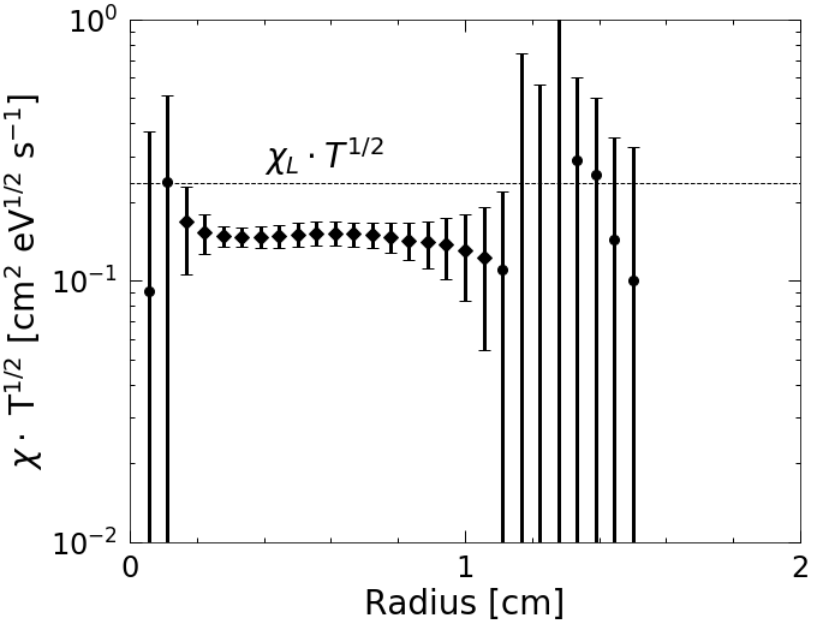

Figure 5.16: Thermal diffusivity as a function of radius at $B_z = 1$ kG. The points (circles and diamonds) represent the scaled diffusivity at that radius averaged over the time steps; the error bars represent the standard deviation associated with averaging over the time steps. The diamonds show the radial points that are averaged to obtain a single value for the diffusivity for this magnetic field. $\chi_L \cdot T^{1/2}$ is the scaled long-range thermal diffusivity prediction.

excluded in the final calculation for the thermal diffusivity. The theoretical prediction for the long range thermal diffusivity is shown by the dashed line in Fig 5.16. We observe that the useful data points indicated by the diamonds are approximately a factor of 2 lower than the prediction. We obtain a single value for the thermal diffusivity for the magnetic field of $B_z = 1$ kG by averaging the thermal diffusivities at all of the time steps and for all of the radii in the analysis region. The final result gives $\chi \cdot T^{1/2} = 0.147 \pm 0.036$ cm^2 eV$^{1/2}$ s^{-1}, which is again about a factor of 2 lower than the predicted long-range thermal diffusivity $\chi_L \cdot T^{1/2} = 0.236$ cm^2 eV$^{1/2}$ s^{-1}.

5.4.2 High Magnetic Field

We now describe the five heat transport experiments performed at larger magnetic fields of B_z =4, 9, 12 and 13 kG, with two of the five data sets being taken at B_z =13 kG. For all these experiments, the initial temperature gradients were produced by sloshing the plasma column through an applied squeeze separatrix region, causing strong heating near the radial center (See Sec. (4.5)).

At these magnetic fields, the radial expansion time scale is much longer than the thermal diffusion time scale, so there is negligible radial expansion during the time it takes for collisional diffusion to relax radial temperature gradients within the plasma. This simplifies the analysis since there is no change in the density profile, $\partial n/\partial t = 0$, and therefore there is no radial velocity, i.e. $v_r = 0$. Consequently, the Joule heating rate is negligible. However at these larger magnetic fields, the cyclotron cooling rate is more important, and for the highest magnetic fields tested, the cyclotron cooling rate is comparable to the expected long-range thermal diffusive time scale (See Fig. 5.2). Therefore we include cyclotron cooling in our heat transport model as a source term in q_s.

There are several practical difficulties that arise when conducting heat transport experiments at higher magnetic fields. Firstly, the shot-to-shot reproducibility is not as good at high field as it is at low field. The origins of the decreased shot-to-shot reproducibility is not entirely

understood, but is attributed to the constrained $E \times B$ drift relaxation with very little viscous smoothing. Typically the reproducibilty increases with longer confinement times (10-50 sec); the reason being that there is more time for diffusion and viscosity to smooth the initial irregularities in the density profile that arise from the injection process. Recalling from Chapter 3 that each temperature profile requires ≈70 experimental cycles (dumps at different V_H) then, if each experimental cycle takes ≈ 50 seconds, a single temperature profile requires about an hour. A complete heat transport experiment consisting of 10 temperature profiles then takes approximately $10-12$ hours of continuous running. We do not observe a coherent monotonic drift of the experimental parameters over the full duration of any given heat transport experiment. However there are fluctuations of the plasma parameters that cause an increase in the error associated with the temperature profiles and we estimate that the temperature profiles have an error of 10%.

Furthermore, the initial plasma profile at high magnetic field often contains a large density spike near $r = 0$ cm. The density spike is approximately an order of magnitude higher in density than the typical density of the rest of the plasma profile and the density spike has significant shot-to-shot variation $\approx 5\%$. The large density spike arises from the turbulent relaxation of the initially filamented density inherited from the spiral filament. The spiral structure is highly unstable to Kelvin-Helmholtz instabilities and the resulting turbulent evolution results in a large density spike at $r = 0$. To remove the density spike, we either apply a strong azimuthally-symmetric squeeze potential to induce radial transport and flatten the density spike or we eject the density spike by briefly reducing the confinement barrier to allow some electrons to escape. When ejecting the particles from the center of the plasma, we are careful to not reduce the confinement barrier so much so that a hole is created in the profile leading to an unstable distribution. Because of the reduction of the shot-to-shot reproducibility and the long duration requirement for a complete heat transport experiment, we require more substantial smoothing of the temperature profiles than was required at $B_z = 1$ kG.

To create the initial temperature gradients the plasma column is axially oscillated through

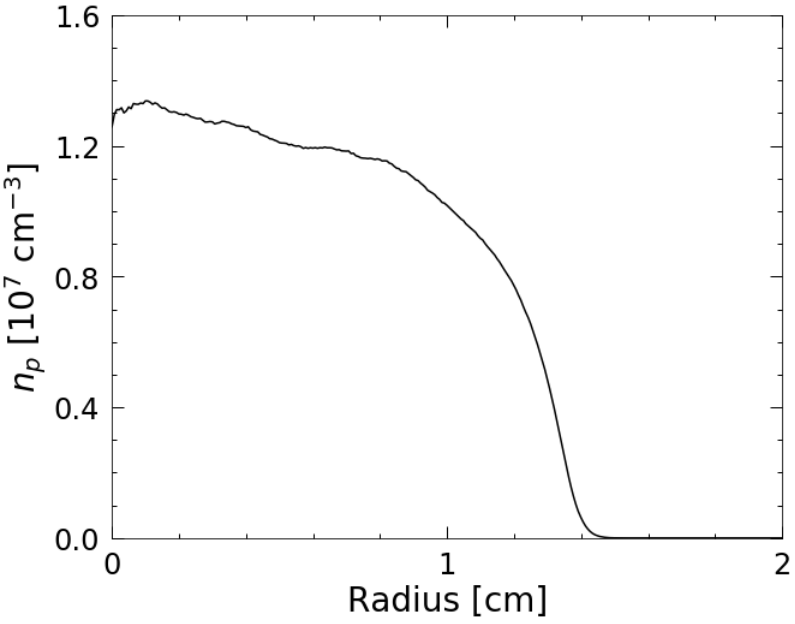

Figure 5.17: Density profile for heat transport experiment at $B_z = 13$ kG

a squeeze potential to create radially localized heating near the radial center of the plasma column [81, 82]. An initial temperature profile is shown in Fig. 5.18.

Here we describe one of the heat transport experiments at $B_z = 13$ kG which exemplifies the five heat transport experiments performed at higher magnetic fields. The plasma is confined between electrodes 2 and 10, giving a confinement length of $L_c = 38.5$ cm and an effective plasma length of $L_p^* = 34$ cm. The plasma is injected into the trap and the profile is shaped and conditioned so that it is relatively close to a Gaussian shape without a density spike near $r = 0$. After the conditioning, the plasma is given enough time for cyclotron radiation to cool the plasma to the wall temperature, $T_w = 0.03$ (i.e. room temperature). With the plasma at a nearly uniform temperature of T_w we apply separatrix-crossing dissipation to the plasma at a time of $t = 49.875$ s. For the separatrix-crossing dissipation parameters, a $V_{sq} = -30$ V squeeze is applied to electrode 6 at the axial midpoint of the plasma column. The squeeze is applied for a duration of $t_{sl} = 125$ ms, during which time the plasma is sloshed though the squeeze by oscillating the voltage on the confinement electrodes at $f_{sl} = 100$ kHz with an amplitude of $V_{sl} = 40$ V.

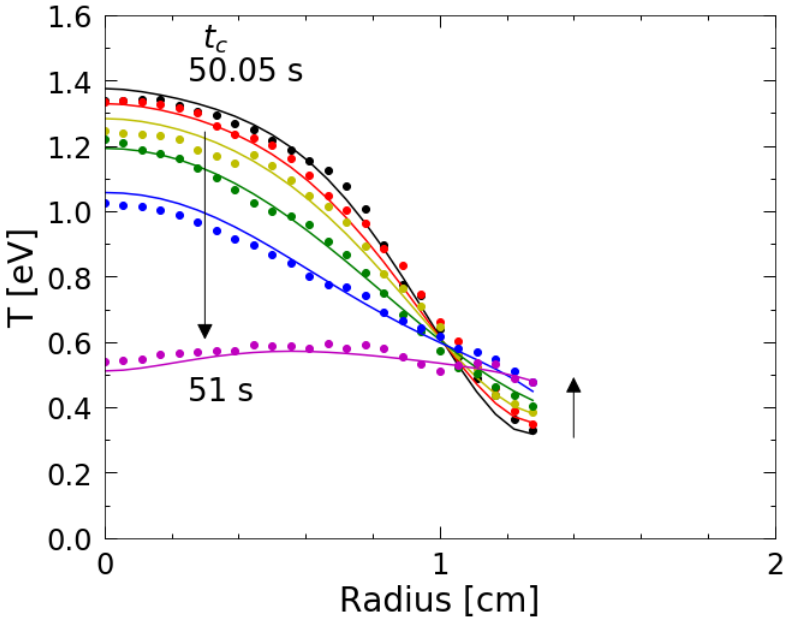

Figure 5.18: Temperature profile evolution at $B_z = 13$ kG. Profiles are shown at confinement times of t_c =50.05, 50.10, 50.15, 50.25, 50.40, 51.00 s. Arrows show the direction of temporal evolution.

The slosh and squeeze are both concluded at a time of $t = 50.000$ s, and the resulting temperature profile is peaked on axis with cooler temperatures at larger radii. We then measure the temperature profile using the technique presented in Chapter 3. We measure the temperature profile at confinement times of $t_c = 50.050$, 50.075, 50.100, 50.125, 50.150, 50.175, 50.200, 50.250, 50.300, 50.400, 50.600, 50.800 and 51.000 seconds. The density profile is unchanged within the measurement error, and a typical density profile is shown in Fig. 5.17. The temperature profile evolution is shown in Fig 5.18, where for purposes of visual clarity we have only shown 6 temperature profiles.

We smooth the temperature profile in radius and in time using 3rd and 5th order polynomials respectively. Once again we apply the constraint that $\partial T/\partial r = 0$ at $r = 0$ due to radial symmetry. In Fig. 5.18 the original temperature profiles are plotted with circles, and the profiles after they have been smoothing in radius and time are shown as solid lines.

We verify that there is negligible radial expansion by plotting $\langle r^2 \rangle$ in Fig. 5.19. We observe

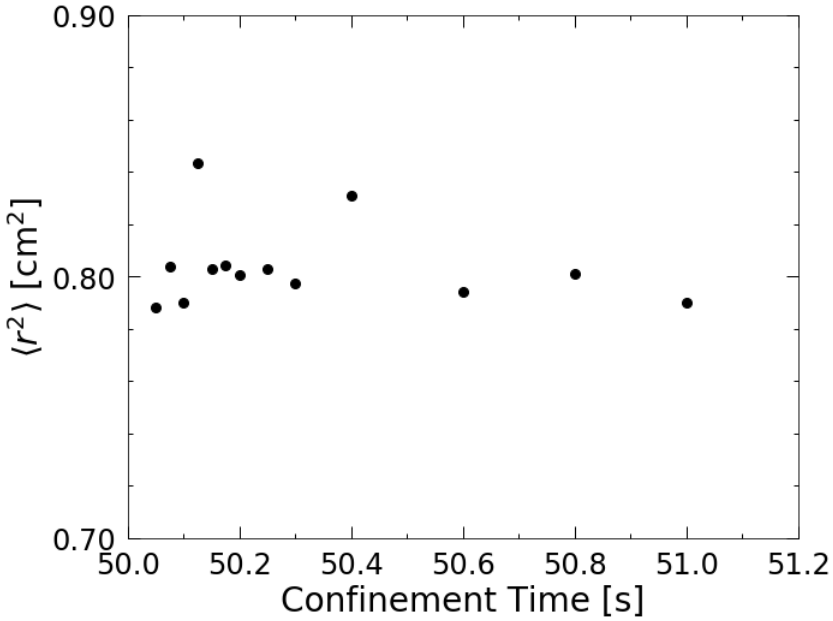

Figure 5.19: Calculated mean-square radius at each confinement time at $B_z = 13$ kG

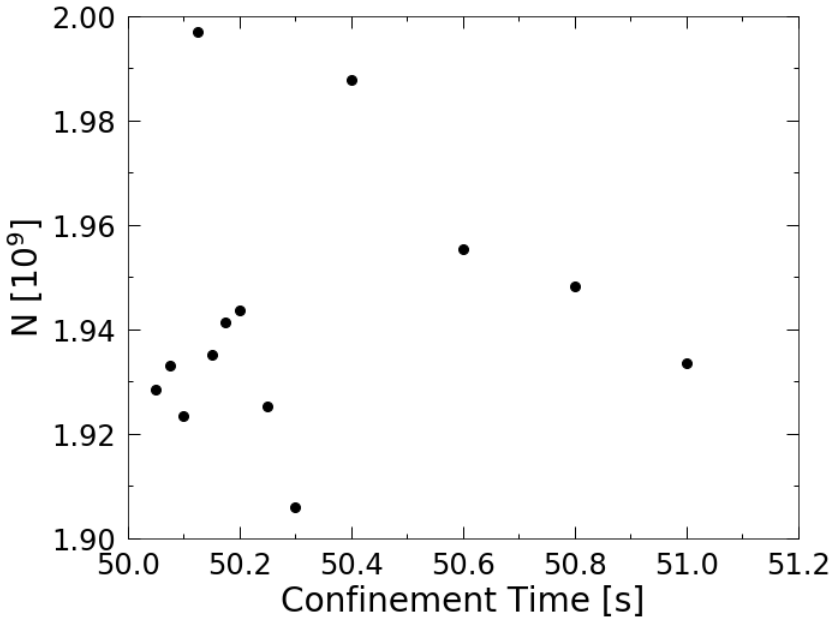

Figure 5.20: Total number of particles at $B_z = 13$ kG. The $\approx 5\%$ fluctuations in the total number of particles is associated with the reduced shot-to-shot reproducibility at higher magnetic field.

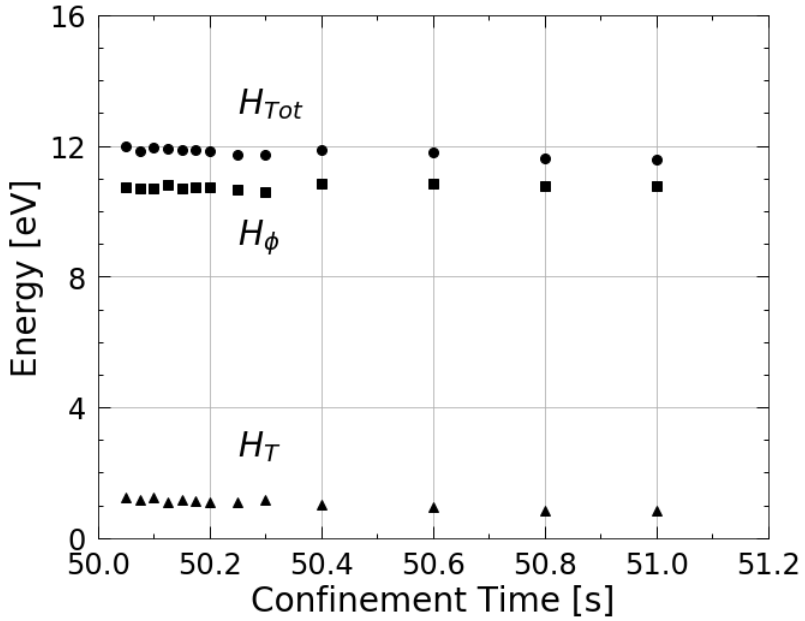

Figure 5.21: The total energy per particle, H_{Tot}, and the thermal energy per particle, H_T, decrease due to cyclotron radiation while the electrostatic energy per particle, H_ϕ, remains constant.

no coherent trend in $\langle r^2 \rangle$ during the duration of the heat transport experiment. Furthermore, we observe no coherent trend in N_{tot} as seen in Fig. 5.20, which indicates that we are not losing particles and we are not gaining particles during the evolution. However, both $\langle r^2 \rangle$ and N_{tot} fluctuate about 5%, which we attribute to the reduced shot-to-shot reproduciblity at high magnetic field.

Since there is no change in the density profile, the electrostatic energy per particle H_ϕ is constant. However, cyclotron cooling causes a significant decrease in the thermal energy per particle H_T, as well as in the total energy H_{Tot}. From Fig. 5.21 we see a slow decrease in H_T and H_{Tot} while there is no change in H_ϕ above the shot-to-shot error. Without Joule heating, the source term in Eq. (5.8) consists solely of cyclotron cooling given by Eq. (5.12).

The inclusion of the cyclotron cooling term requires a measurement of the cyclotron cooling time, τ_r, which we accomplish using the $m = 1$ Diocotron mode frequency f_d. This measurement is accomplished by secondary experiments unrelated to heat transport where

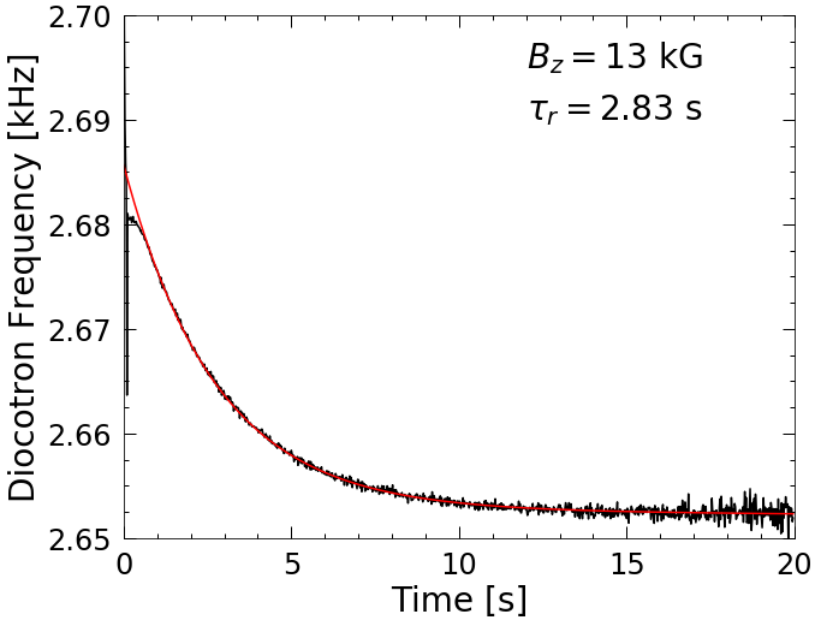

Figure 5.22: Time evolution of the $m_\theta = 1$ Diocotron frequency as the plasma cools towards room temperature. The Diocotron mode is excited to low amplitude at 100 ms. The frequency initially decays exponentially due to cyclotron cooling and then linearly due to a slow radial expansion.

we excite a $m = 1$ Diocotron mode and measure the temporal evolution of the frequency. The frequency of the $m = 1$ Diocotron mode exhibits a temperature dependence as shown in Eq. (2.41). The frequency f_d also depends on R_p and N_L, therefore changes in either of those parameters will also cause changes in f_d. However at high magnetic fields, R_p changes slowly compared to changes in T from cyclotron cooling. Furthermore, N_L changes very slightly due to changes in T because the length of the plasma decreases slightly as the plasma cools. Therefore, on the time scale of cyclotron cooling, the changes to f_d are solely attributed to changes in T. We can determine the cyclotron cooling time by measuring the exponential decay of the $m = 1$ Diocotron mode as the plasma cools. An example of the temporal evolution of the $m = 1$ Diocotron mode is shown in Fig. 5.22 where the black line shows the measured Diocotron frequency and the red line is a fit that consists of an exponential term plus a linear term to account for the cyclotron cooling and the slow radial expansion. The cyclotron cooling time is then determined from fit parameters.

The $m = 1$ Diocotron mode is used to determine τ_r at magnetic fields of B_z =9, 12 and

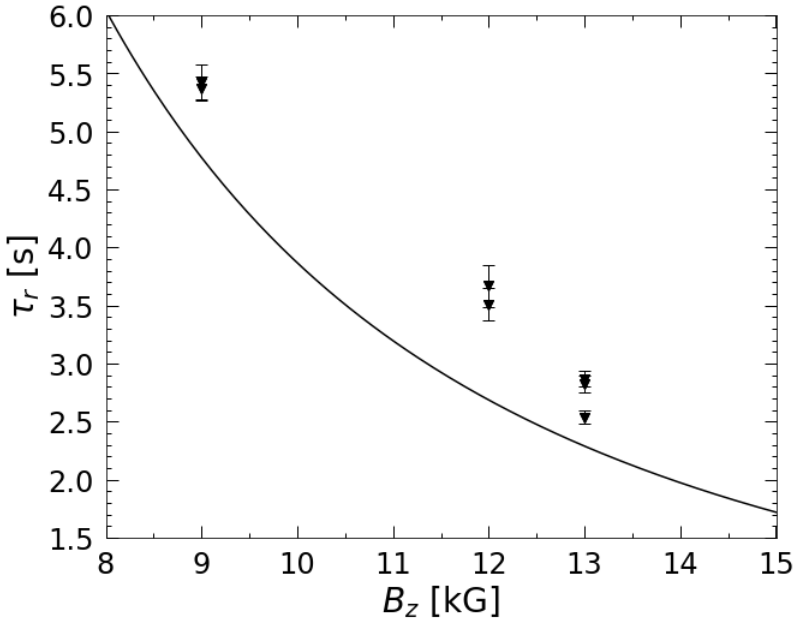

Figure 5.23: Cyclotron cooling times measured from the time evolution of the $m_\theta = 1$ Diocotron frequency. The solid line is the predicted cyclotron cooling time from Eq (2.19). Error bars represent the standard deviation from multiple experimental cycles.

13 kG. The results of these measurements are shown in Fig. (5.23) where the solid line is the predicted cyclotron cooling time from Eq. (2.19). We observe agreement within 10% of the predicted rate with our measured cycltron cooling time being systematically larger than the prediction as is typically seen in Penning-Malmberg trap experiments [52]. The measurement of the cyclotron cooling time is not performed at $B_z = 4$ kG because the radial expansion time is comparable to the cyclotron cooling time, i.e. there is non-negligible Joule heating during the cyclotron cooling process. However, the cyclotron cooling time at a magnetic field of $B_z = 4$ kG is approximately $\tau_r \approx 24$ s from Eq. (2.19), which is much longer than the 1 second duration of the heat transport experiment. The cyclotron cooling rate is negligibly small for the experiment that is conducted at $B_z = 4$ kG and an experimentally measured rate for the cyclotron cooling rate is not required. With the measured cyclotron cooling time we calculate the rate of cyclotron cooling using Eq. (5.12), the results of which are shown in Fig. (5.24).

With the cyclotron cooling rate determined we now proceed to the calculation of the

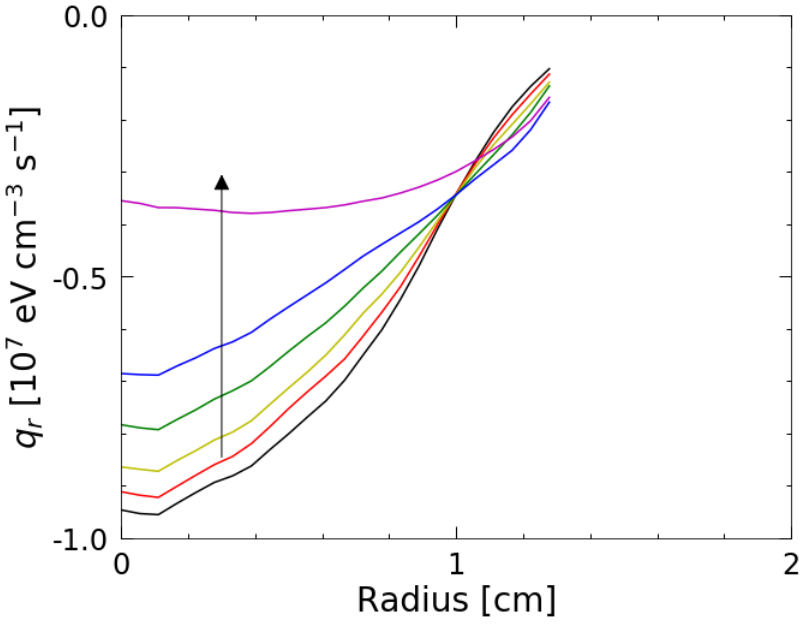

Figure 5.24: Cyclotron cooling rate at $B_z = 13$ kG shown at confinement times of t_c =50.05, 50.10, 50.15, 50.25, 50.40, 51.00 s. Arrow shows the direction of temporal evolution.

diffusive heat flux using Eq. (5.8). Since the density is unchanged during the measurement, the time derivative is given by $(3/2)\partial(n_pT)/\partial t = (3/2)n_p(\partial T/\partial t)$ and the radial velocity is $v_r = 0$ so there is no convective term. The time derivative is calculated from the polynomial fits to the temperature evolution. The diffusive heat flux is shown in Fig. 5.25, where the positive heat flux indicates an outward flow of heat consistent with the negative radial temperature gradient.

The temperature gradients are shown in Fig. 5.26. The magnitude of the temperature gradient is large immediately after the end of the separatrix-crossing dissipation but then the temperature gradient decreases as temperature equilibrium is achieved.

Again, we verify the applicability of Fick's law to describe the diffusive heat flux. In Fig. 5.27 we have plotted the negative of the scaled heat flux and the temperature gradient at a confinement time of $t_c = 50.15$ s and have normalized each of the profiles to their respective maximum values to highlight the proportionality between the two quantities.

As before, the radial region where the thermal diffusivity is calculated is shown by the vertical dashed lines in Fig. 5.27. Furthermore, we will not use the last two time steps at $t_c = 50.80$

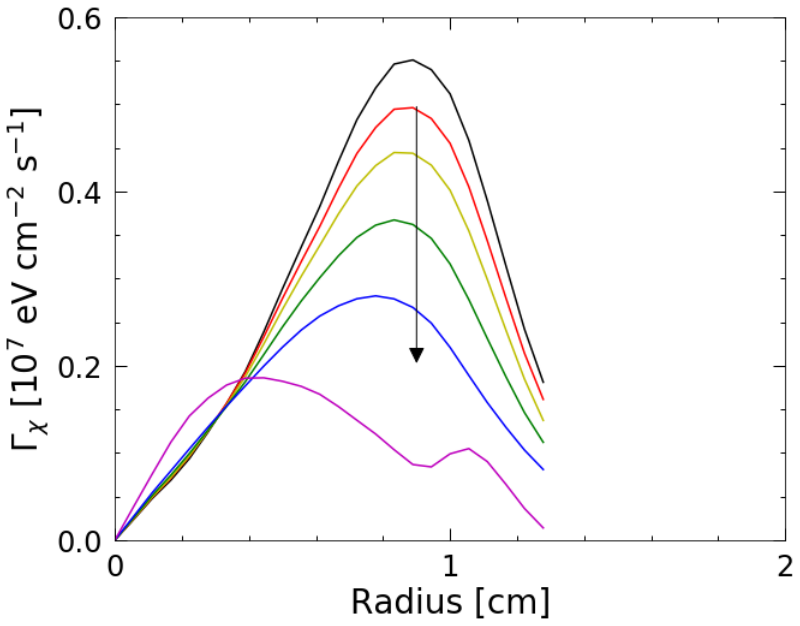

Figure 5.25: Diffusive heat flux at $B_z = 13$ kG shown at confinement times of t_c =50.05, 50.10, 50.15, 50.25, 50.40, 51.00 s. Arrow shows the direction of temporal evolution.

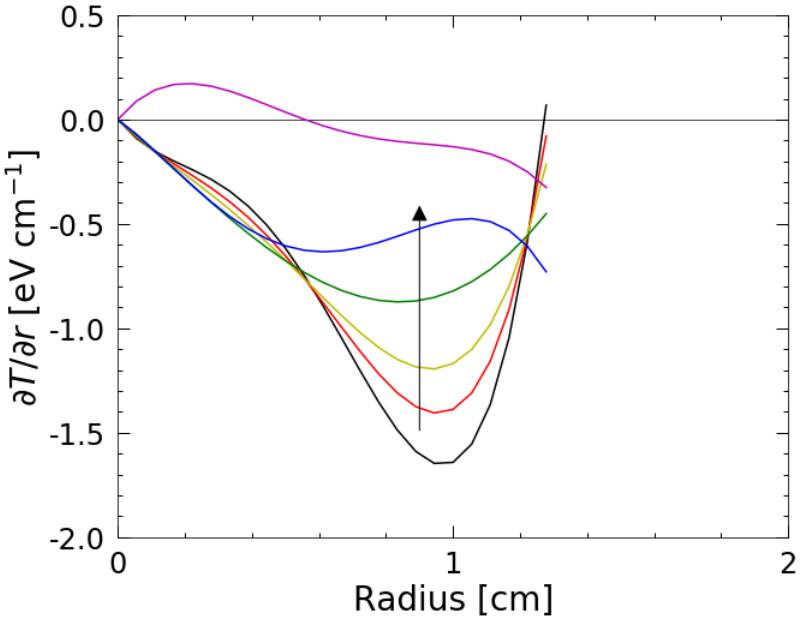

Figure 5.26: Temperature gradient at $B_z = 13$ kG shown at confinement times of t_c =50.05, 50.10, 50.15, 50.25, 50.40, 51.00 s. Arrow shows the direction of temporal evolution.

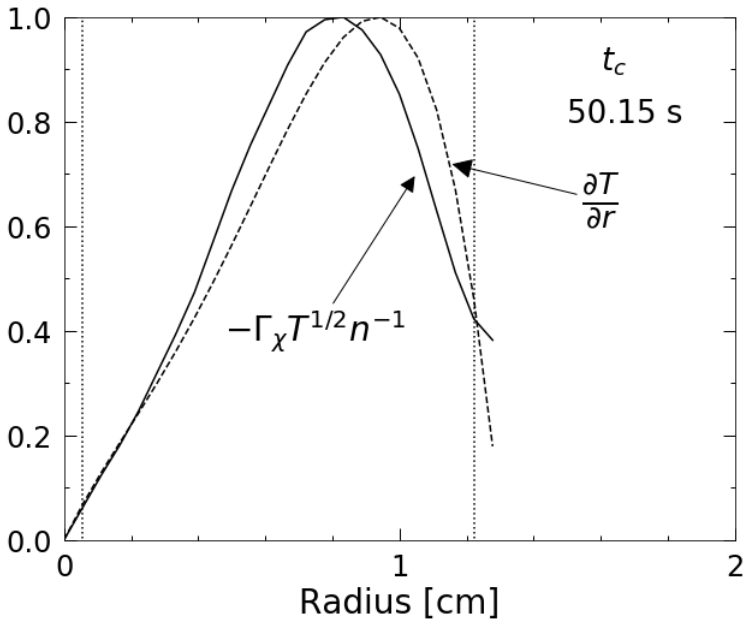

Figure 5.27: Scaled diffusive heat flux (solid) and temperature gradient (dashed) at $B_z =$ 13 kG. Both quantities are normalized to their respective maximum values to highlight the proportionality between the two quantities.

and $t_c = 51.00$ to calculate the thermal diffusivity, since the temperature gradients and the heat flux are small. Note that this issue did not arise in the heat transport experiment at $B_z = 1$ kG because the continuous Joule heating maintained a large temperature gradient and large heat flux at all times throughout the experiment.

Fig. 5.28 shows the scaled heat flux versus the radial temperature gradient for all of the confinements times and radii used in the calculation of thermal diffusivity. The solid line is an unconstrained linear fit, and we see that the data is well represented by a linear relationship between the scaled heat flux and the temperature gradient. We attribute the small nonzero y-intercept offset due to measurement error rather than representing a non-diffusive heat flux that has not been accounted for.

The calculated thermal diffusivity at each radius is shown in Fig. 5.29, the error bars represent the standard deviation from averaging over the time steps. The theoretical prediction for long-range thermal diffusivity is shown as the dashed line in Fig 5.29.

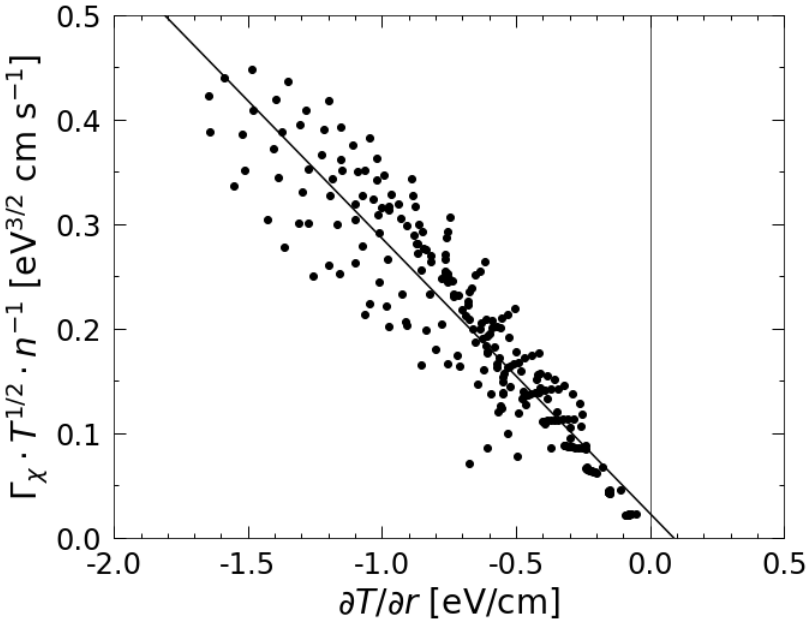

Figure 5.28: Scaled heat flux versus temperature gradient at $B_z = 13$ kG, the points represent all of the time steps at the subset of radii that are used to calculate the thermal diffusivity. The scaling is informed by the theoretical predictions and the scaling parameters are chosen so that the heat flux is proportional to the temperature gradient. The solid line is an unconstrained linear fit

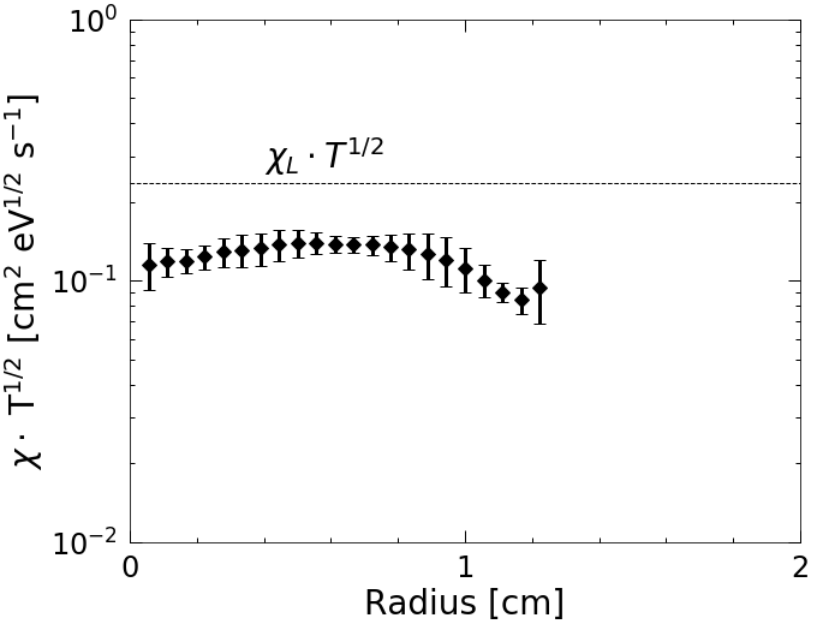

Figure 5.29: Thermal diffusivity as a function of radius at $B_z = 13$ kG. The diamonds represent the scaled diffusivity at that radius averaged over the time steps; the error bars represent the standard deviation associated with averaging over the time steps. The radial points are averaged to obtain a single value for the diffusivity for this magnetic field. $\chi_L \cdot T^{1/2}$ is the scaled long-range thermal diffusivity prediction.

We obtain a single value for the thermal diffusivity for the magnetic field of $B_z = 13$ kG by averaging the thermal diffusivities at all of the usable time steps and for all of the radii in the analysis region. The final result gives $\chi \cdot T^{1/2} = 0.122 \pm 0.020$ cm^2 eV$^{1/2}$ s^{-1}, which is a factor of 2 lower than the predicted long-range thermal diffusivity $\chi_L \cdot T^{1/2} = 0.236$ cm^2 eV$^{1/2}$ s^{-1}.

The previous analysis at a magnetic field of $B_z = 13$ kG is typical for the heat transport experiments performed at B_z =4, 9, 12 and 13 kG. At each magnetic field, a final thermal diffusivity is determined by averaging over the usable range of radii and time steps.

The thermal diffusivity determined for each magnetic field, including the low magnetic field data at $B_z = 1$ kG, is compiled and presented in Fig 5.30. The error bars represent the standard deviation associated with averaging over the usable radii and time steps. The dashed line represents the theoretical prediction for the long-range thermal diffusivity. The solid line represents the theoretical prediction for the classical thermal diffusivity evaluated at a typical

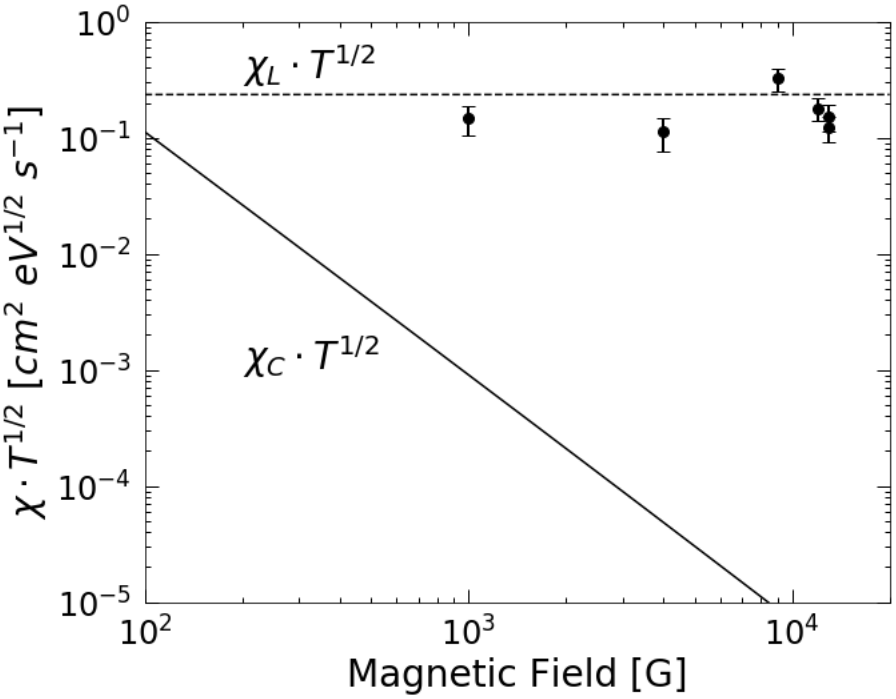

Figure 5.30: Measured thermal diffusivity versus B_z. χ_L is the thermal diffusivity due to long-range collisions and χ_C is the thermal diffusivity due to classical short-range collisions.

density of $n_p = 10^7$ cm^{-3}. In general we observe a factor of 2 agreement between the data points and the prediction for the long-range thermal diffusivity. The experiments also demonstrate and verify the magnetic-field-independence of the thermal diffusivity, which is in stark contrast to the classical thermal diffusivity which decreases by two orders of magnitude over the range of magnetic fields used in these experiments.

5.5 Conclusion

In conclusion we have measured the thermal diffusivity over a range of magnetic fields from $B_z = 1$ kG to $B_z = 13$ kG. We model the heat transport using a Convection-Diffusion equation where the diffusive heat transport is verified to obey a local Fick's law equation. We then calculate the thermal diffusivity using the temporal evolution of the density and temperature profiles. Our measurements show that the thermal diffusivity is independent of the magnetic field

and our measured values are within 50% agreement with the prediction of thermal diffusion due to long-range collisions.

5.6 Acknowledgments

This chapter, in part, is currently being prepared for submission for publication. K. A. Thompson, A. A. Kabantsev, N. Panzeri and C. F. Driscoll. The dissertation author was the primary investigator and author of this material.

Appendix A

Collector Plate Temperature Measurement Corrections

In this appendix we discuss the necessary corrections for processing raw temperature measurement data when measuring the $r = 0$ temperature using the "tail temperature" measurement method, T_{CP}. This method was developed at the University of California San Diego and is described by Hyatt [49, 71], Beck [42, 50] and Egglesston [55]. The relative ease of use of this method has promoted it to the standard temperature measurement technique in nonneutral plasma studies.

Several correction factors need to be determined and applied to the raw data in order to obtain accurate temperature results but the magnitudes of the corrections vary from device to device (and from experiment to experiment within the same device). Hart et. al. [63] performed temperature measurement experiments on an electron plasma confined in a Penning-Malmberg trap where the length of the confinement electrode was smaller than R_w which results in significant curvature of the ends of the plasma column and large correction factors for the raw temperature measurements. Aoki et. al. [64] performed a similar analysis of temperature measurement but on an electron plasma confined in a Penning trap which nominally has a harmonic axial potential

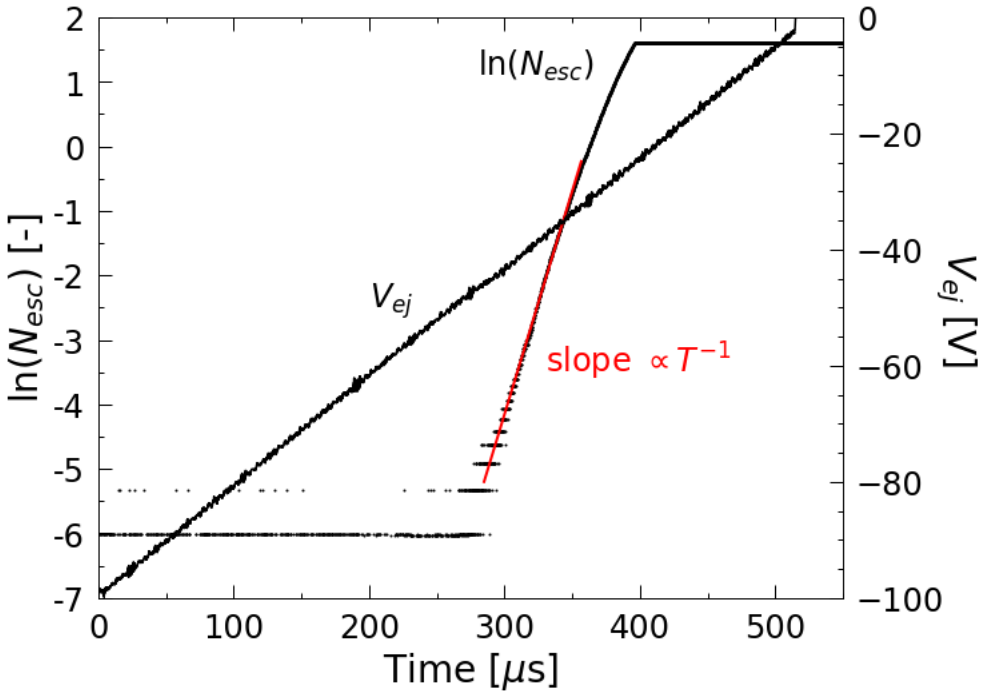

Figure A.1: Example of the measured escape charge as the confinement barrier is reduced. The gain of the signal amplifier circuit is intentionally set so that the signal saturates after the linear region of $ln(N_{esc})$ in order to improve the signal-to-noise ratio for the data of interest. The fit to the linear portion of $ln(N_{esc})$ is shown in red and yields a temperature of 2.8 eV.

well.

Following the method of Eggleston et al. [55], we reduce the confinement barrier created by the eject electrode and measure the first 1-2% of escaping electrons which escape from the vicinity of $r = 0$. Since we are only concerned with the behavior near $r = 0$, the following equations are all evaluated at $r = 0$ and we omit the radial dependence. Assuming that the plasma is Maxwellian, there is a simple relationship between the measured number of escaping electrons, N_{esc}, and the confinement energy, E_c, given by

$$\frac{d\ln(N_{esc})}{dE_c} = -\frac{1.05}{T'} \tag{A.1}$$

We have indicated the temperature with a prime, consistent with the notation from Chapter 3, because the temperature of the plasma when the first electrons begin to escape is lower than

the temperature of the fully confined plasma due to the cooling that occurs during the adiabatic expansion of the plasma column as the eject confinement barrier is reduced.

The basic measurement is the number of electrons which escape as the confinement barrier is reduced in magnitude. That is, we use the collector plate to record the number of escaping electrons as a function of the voltage applied to the eject electrode, V_{ej}, giving $d\ln(N_{esc})/d(qV_{ej})$. However, the relationship in Eq (A.1) requires $d\ln(N_{esc})/dE_c$. Therefore we must determine the relationship between the confinement energy at $r = 0$ and the eject electrode voltage, that is, we need to determine $dE_c/d(qV_{ej})$. Furthermore we include a correction for the cooling that occurs during the adiabatic expansion of the plasma which is given by the square of the ratio of the initial length (fully confined length) to the length when electrons begin to escape.

We defined the term, $\varepsilon = L_p(r)/L'_p(r,V_{ej})$, for the ratio of lengths where $L_p(r)$ is the length of the initial plasma and $L'_p(r,V_{ej})$ is the length of the plasma as a function of the eject voltage. The relationship between T' and T is $T' = \varepsilon^2 T$. Eq (A.1) then becomes

$$T = -\frac{1.05}{\varepsilon^2}\frac{dE_c}{d(qV_{ej})}\left(\frac{d\ln(qN_{esc})}{d(qV_{ej})}\right)^{-1} \tag{A.2}$$

We evaluate E_c by neglecting the axial dependence of the confinement energy in Eq. (3.2) and then we evaluate the second term in Eq. (3.2) at z_{mid} which is the axial center of the plasma column, located far from the confinement electrodes. The derivative of E_c is then given by

$$\frac{dE_c}{d(qV_{ej})} = \left.\frac{d(q\phi)}{d(qV_{ej})}\right|_{z=z_{max}} - \left.\frac{d(q\phi)}{d(qV_{ej})}\right|_{z=z_{mid}} \tag{A.3}$$

We will calculate $dE_c/d(qV_{ej})$ using Eq. (A.3) which requires the model presented in Chapter 3 in order to calculate $q\phi$ as a function of the eject electrode voltage.

Several simplifications to Eq. (A.3) are often made, so that the analysis does not require the calculated (r,z) spatial distribution of $q\phi$. Firstly, it is assumed that the potential at z_{mid} is solely from the plasma potential ϕ_p, with no contribution from the electrode potentials ϕ_c, so that

$q\phi(z=z_{mid}) = q\phi_p(z=z_{mid})$. Furthermore, because we only analyze the first 1-2% of particles that escape from the trap, the assumption is made that ϕ_p is constant so that the second term in Eq. (A.3) is zero. As for the confinement barrier, it is assumed that the potential at z_{max} is entirely attributed to the electrode potential, $q\phi(z=z_{max}) = q\phi_c(z=z_{max})$, therefore the first term in Eq. (A.3) can be calculated as a derivative of the solution to Laplace's equation rather than Poisson's equation because the plasma component to the potential has been neglected.

We solve Laplace's equation to determine α, which we define as the ratio between the confinement potential at $r=0$ and the potential at $r=R_w$, so that $\phi_c(r=0) = \alpha V_{ej}$. Then Eq. (A.3) ultimately reduces to $dE_c/d(qV_{ej}) = \alpha$. For the eject electrodes used in our experiments which have a radius of $R_w = 3.5$ cm and a length of 7 cm, we have $\alpha \approx 0.87$ indicating that the magnitude of the confinement barrier at $r=0$ is 13% less than qV_{ej} at the wall. The benefit of the simplifications are that $dE_c/d(qV_{ej}) = \alpha$ depends only on the geometry of the eject electrode and does not depend on the plasma parameters. With these simplifications, $dE_c/d(qV_{ej})$ is easily determined before experiments are executed, greatly simplifying the numerical post-processing to obtain the temperature. For the geometry of the electrodes used in CamV, where the length of the electrode is larger than R_w, the simplifying approximations to Eq. (A.3) are often reasonable assumptions, as we will see.

Now we return to the full evaluation of Eq. (A.3), which must be accomplished numerically using the model presented in Chapter 3. We demonstrate the calculations on the configuration where the plasma is confined between electrodes 1 and 10 giving a confinement length of $L_c = 52.5$ cm so that the effective length is $L_p^* = 48$ cm and the magnetic field is $B_z = 2$ kG.

In Fig. A.2 we plot $q\phi(z=z_{mid})$ and in Fig. A.3 we plot $q\phi(z=z_{max})$. From the plot of $q\phi(z=z_{mid})$, it is seen that $q\phi(z=z_{mid})$ is nearly constant in the range from $-50 \geq V_{ej} < -40$ V which lends credibility to the previously discussed simplification where it is assumed that $d(q\phi_p(z=z_{mid}))/d(qV_{ej}) = 0$ for the initial escaping particles. For $V_{ej} > -35$ V the potential drops off rapidly due to the increasing number of escaping electrons; and this is the reason that

the T_{CP} temperature measurement method is limited to analysis of only the first 1-2% of escaping electrons.

To obtain the derivatives required for evaluating Eq. (A.3), we do linear fits in the range $-50 < V_{ej} < -45$ V as indicated by the solid lines in Fig. A.2 and Fig. A.3. From the fits we obtain $d(q\phi(z = z_{mid}))/d(qV_{ej}) = 0.019$ and $d(q\phi(z = z_{max}))/d(qV_{ej}) = 0.835$. If the potential at $z = z_{max}$ were entirely due to the confinement electrode with no contribution from the plasma potential then we would expect $d(q\phi(z = z_{max}))/d(qV_{ej}) = 0.87$ as calculated from the Laplace solution. However the calculated $d(q\phi(z = z_{max}))/d(qV_{ej})$ is slightly less than 0.87, which indicates that the plasma contribution to $q\phi(z = z_{max})$ is non-negligible. Using Eq. (A.3) we then obtain $dE_c/d(qV_{ej}) = 0.816$ as shown in Fig A.4. Therefore we see that there is a decrease in $dE_c/d(qV_{ej})$ when using the full model solution for $q\phi$ compared to the result $dE_c/d(qV_{ej}) = 0.87$ obtained from the simplifications of neglecting the $q\phi(z = z_{mid})$ term and using Laplace's equation.

All that remains is to determine the axial expansion correction which is shown in Fig. A.5. We average over ε^2 in the range from $-50 < V_{ej} < -45$ V to obtain $\varepsilon^2 = 0.943$. Note that for $V_{ej} > -35$ V, ε^2 begins to increase, ultimately becoming greater than one which would indicate axial compression and possibly heating of the particles due to the compression. As discussed in Chapter 3, the length of the plasma begins to shrink when the density becomes very small and it is not clear whether or not this increases the temperature of the plasma due to the decrease in the length of the plasma. However, this effect only occurs when the density has become negligible small and ignoring any possible heating associated with a decrease in the length of the plasma does not affect the temperature calculation because even if this heating is included it is a small effect.

The total correction factor to be applied to the raw data is then $(1/\varepsilon^2)dE_c/d(qV_{ej}) = 0.866$. We have calibrated all of our T_{CP} measurements using the method presented in this Appendix. The correction factors for the data shown in Fig. 3.8 are presented in Fig. A.6. The solid line in Fig. A.6

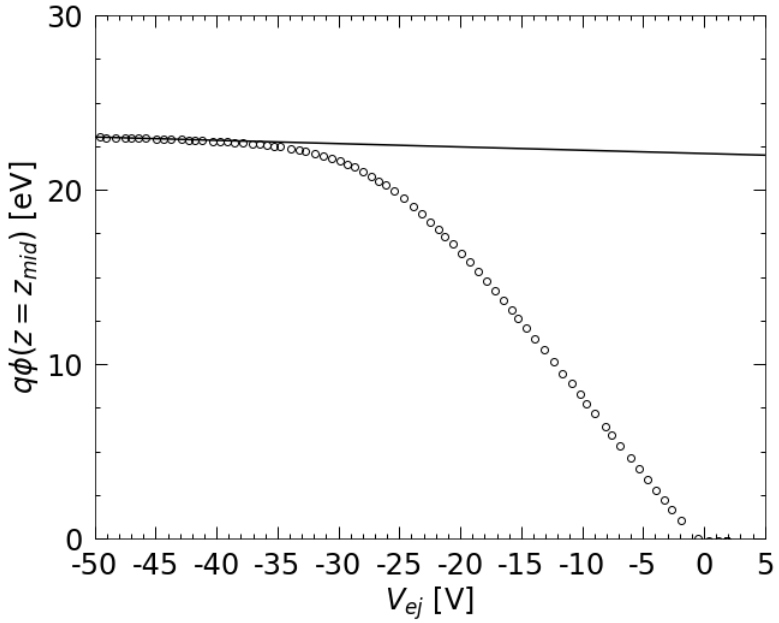

Figure A.2: Plot of the on-axis potential at the axial center of the plasma. The solid line is a linear fit to the data in the range $-50 < V_{ej} < -45$ V.

represents the correction obtained from using the simple relationship $dE_c/d(qV_{ej}) = \alpha = 0.87$ with no correction for adiabatic expansion. The majority of the data points are narrowly scattered around 0.87. The reason for this is that the correction due to the full numerical calculation of $dE_c/d(qV_{ej})$ using Eq. (A.3) results in a correction factor that is less than 0.87. However, the adiabatic expansion correction slightly compensates the $dE_c/d(qV_{ej})$ correction so that the net result is that the total correction factor is very nearly 0.87 for most experimental configurations of CamV.

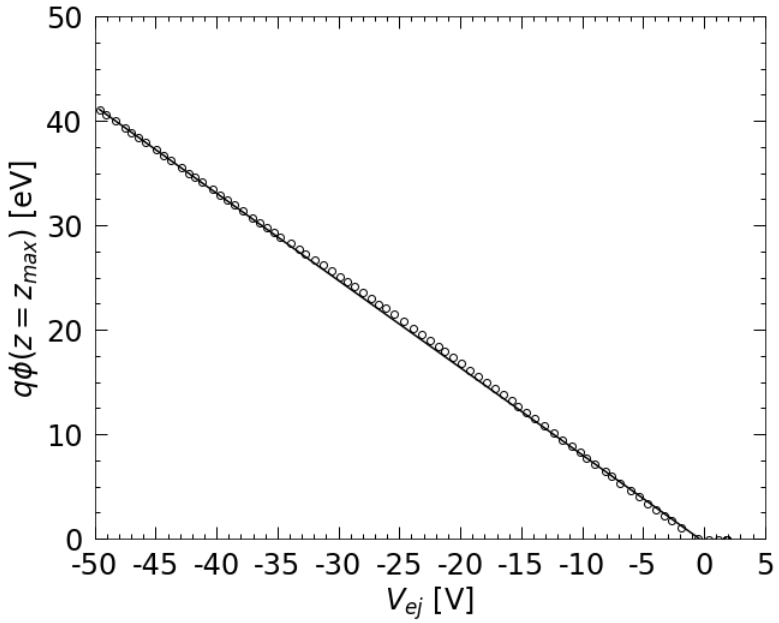

Figure A.3: Plot of the on-axis potential at z_{max} which is the axial position where the maximum confinement barrier is located. The solid line is a linear fit to the data in the range $-50 < V_{ej} < -45$ V.

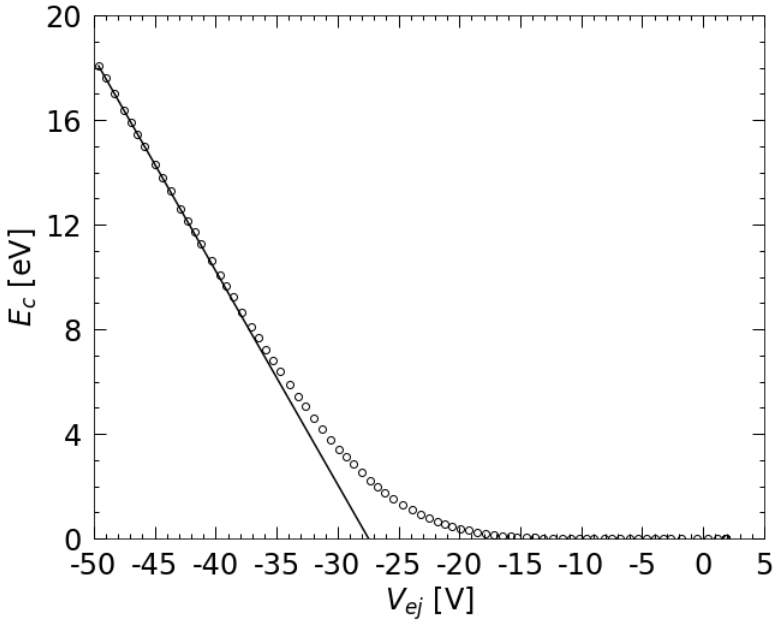

Figure A.4: Plot of the on-axis confinement energy. The solid line is a linear fit to the data in the range $-50 < V_{ej} < -45$ V.

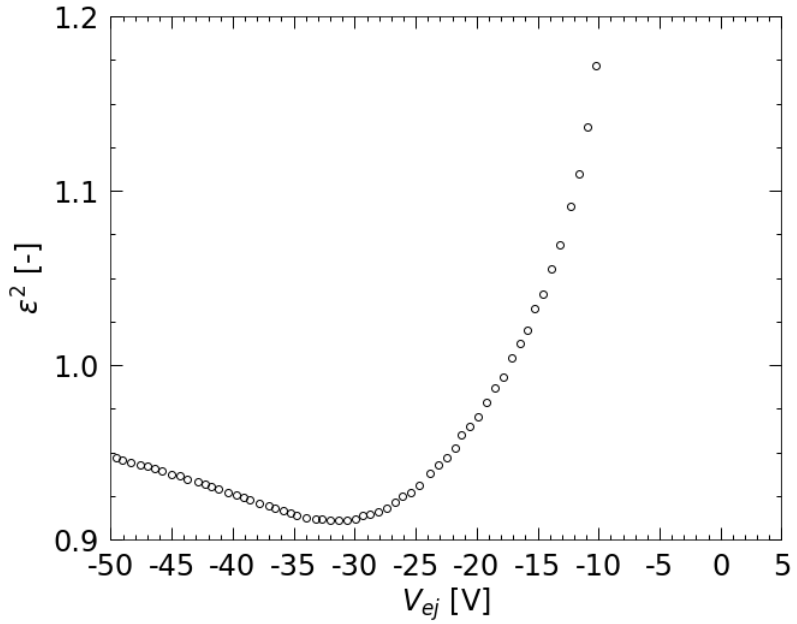

Figure A.5: Plot of the on-axis adiabatic expansion coefficient. $\varepsilon^2 < 1$ initially due to axial expansion as the confinement barrier is reduced. Later, $\varepsilon^2 > 1$ as the significant reduction in the plasma potential causes the plasma length to shrink axially.

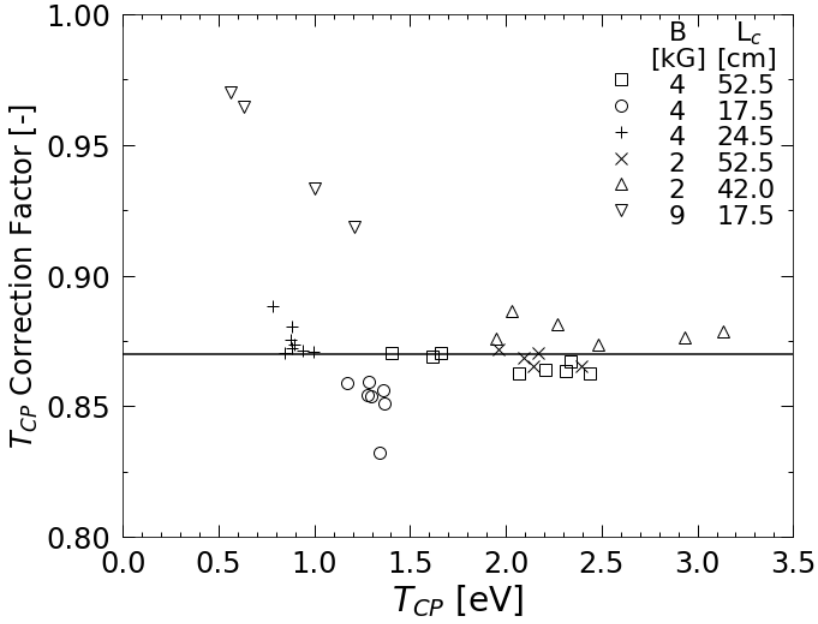

Figure A.6: Plot of the correction factor for adjusting the raw T_{CP} measurements. The solid line at 0.87 represents the Laplace solution correction without the adiabatic cooling correction for an electrode with radius 3.5 cm and length 7 cm.

Appendix B

Separatrix-Crossing Dissipation Calibration

In this appendix we discuss the oscillation of the confinement potentials when heating the plasma column using separatrix-crossing dissipation (See Sec. (4.5) and Fig. 4.5). Separatrix-crossing dissipation is accomplished by applying a squeeze potential to the axial center of the plasma and then oscillating the plasma column axially back and forth through the squeeze potential. The plasma column is repeatedly forced through the squeeze by oscillating the potentials applied to the confinement electrodes.

The squeeze potential creates a separatrix in the plasma that separates between trapped electrons and passing electrons. Due to the axial sloshing of the plasma column, the lengths of the orbits of trapped electrons are repeatedly compressed and expanded whereas the lengths of the orbits of passing particles experience no compression or expansion. A discontinuity is thereby created in the electron distribution function, due to the compression and expansion of the trapped electron portion of the distribution function.

Collisions between the trapped and passing electrons relax the discontinuity, causing irreversible heating which is maximal near the radius where the separatrix energy is equal to the

thermal energy. By varying the strength of the squeeze potentials we can control the location of the peak heating rate which makes separatrix-crossing dissipation a useful method for creating gradients in the radial temperature profile.

Critical to the heating process is that the passing electrons must experience minimal compression or expansion during the sloshing of the plasma column through the squeeze. However simply increasing the potential on one confinement electrode and decreasing the potential on the other confinement electrode by the same amount will result in an unwanted expansion of the plasma column. Therefore a nontrivial oscillation waveform must be used to oscillate the confinement potentials.

For this discussion we assume that both of the confinement electrodes are at $V_c = -100$ V in the unperturbed state, and so an increase in the confinement potential means that the voltage is getting closer to ground. We will calibrate the oscillation of the confinement potentials when no squeeze potential is applied to the plasma.

If we raise the confinement potential on one of the confinement electrodes then the plasma will expand axially towards that confinement electrode. Conversely, if we lower the confinement potential then the plasma will be pushed away from that confinement electrode. To achieve the best results from separatrix-crossing dissipation we are required to increase the voltage on one confinement cylinder and decrease the voltage on the other confinement cylinder in such a way that the plasma column is shifted axially along the trap but without changing the plasma length. Performing this manipulation is complicated by the nonlinear axial dependence of the confinement potentials. This can be seen from the vacuum potential solution for two half-infinite cylindrical electrodes where $z = 0$ is the boundary between the electrodes and one electrode is grounded and the other is at V_c; the potential within the grounded electrode is given by

$$\phi_c(r,z) = V_c \sum_{i=1}^{\infty} \frac{\exp(-j_{0i}\, z/R_w) J_0(j_{0i}\, r/R_w)}{j_{0i} J_1(j_{0i})} \tag{B.1}$$

where J_0 and J_1 are Bessel functions of the first kind and j_{0i} is the ith zero of J_0. Simply increasing

the voltage of one of the confinement electrodes by a certain amount and then decreasing the voltage on the other confinement electrode by the same amount will result in an expansion of the plasma column because of the nonlinear z-dependence of the electrode potential as exhibited in Eq. (B.1).

We prevent the plasma from expanding by using a waveform that is a pure sine wave when decreasing the potential (pushing the plasma) and is a modified sine wave when increasing the potential (expanding the plasma). The modified portion of the waveform is a sine wave with a quadratic modifier that reduces the amplitude of the signal and generates a waveform that is continuous with a continuous first derivative so that there are no discontinuities that could excite plasma waves. The oscillations of the inject electrode potential, V_{inj}, and the eject electrode potential, V_{ej}, are given by the following waveforms

$$V_{inj}(t) = \begin{cases} V_c - A\sin(2\pi f_{sl} t) & 0 \le t \le t_{sl}/2 \\ V_c - \frac{A\sin(2\pi f_{sl} t)}{1+\eta\sin^2(2\pi f_{sl} t)} & t_{sl}/2 \le t \le t_{sl} \end{cases} \tag{B.2}$$

$$V_{ej}(t) = \begin{cases} V_c + \frac{A\sin(2\pi f_{sl} t)}{1+\eta\sin^2(2\pi f_{sl} t)} & 0 \le t \le t_{sl}/2 \\ V_c + A\sin(2\pi f_{sl} t) & t_{sl}/2 \le t \le t_{sl} \end{cases} \tag{B.3}$$

where A is the amplitude of the signal, f_{sl} is the frequency of the oscillation, $t_{sl} = 1/f_{sl}$ is the period of the oscillation, and η is a calibration factor that has yet to be determined. When $\eta = 0$ the waveform reverts to a pure sinusoid. However, when $\eta \neq 0$ the waveform is a pure sinusoid when the potential decreases (pushing the plasma) and a modified sinusoid when the potential increases (pulling the plasma).

We define the slosh voltage as $V_{sl} = V_{pp}/2$, where V_{pp} is the peak-to-peak voltage, and we can derive a relationship between A and V_{sl},

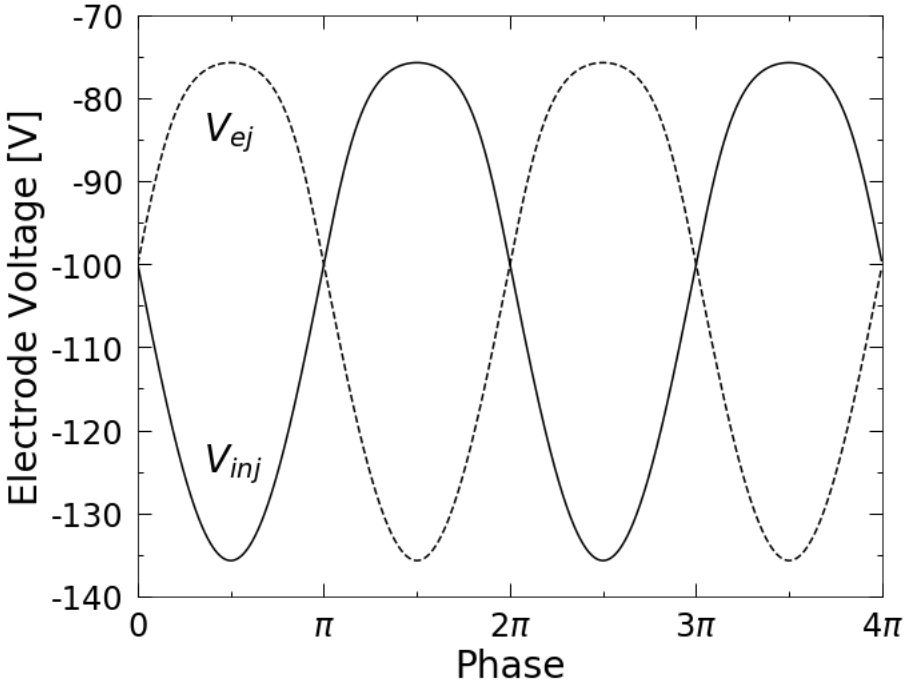

Figure B.1: Waveforms of the oscillations applied to the confinement electrodes to translate the plasma axially without changing the plasma length. The voltage before the oscillations are applied is $V_c = -100$ V. Note the asymmetry in the oscillation; the increase in the voltage is less than the decrease in the voltage which is due to the difference between pulling and pushing the plasma.

$$V_{pp} = \frac{A}{1+\eta} + A \tag{B.4}$$

$$A = 2V_{sl}\left(\frac{1+\eta}{2+\eta}\right) \tag{B.5}$$

Fig. B.1 shows the inject (solid line) and eject (dashed line) potentials using the waveforms given by Eq. (B.2) and Eq. (B.3) with $V_{sl} = 30$ V, $\eta = 0.47$ and $A = 35.7$ V .

Determining the calibration term η requires a diagnostic that gives a measurement of changes in the length of the plasma column when we oscillate the voltage applied to the confinement potentials. The calibration is accomplished by applying the waveforms given by Eq. (B.2) and Eq. (B.3) to the confinement potentials and then varying η until there is minimal change in the length of the plasma during the oscillation of the confinement potentials.

The frequency of the $m_\theta = 1$ Diocotron mode serves as our length change diagnostic because of the dependence of the frequency on the line density, N_L. When the plasma column is compressed or expanded then N_L will increase or decrease accordingly. Therefore a diagnostic that measures changes in N_L can be used to determine if the plasma is being compressed or expanded. We consider the Diocotron mode frequency given by

$$f_d \approx \frac{ceN_L}{\pi B_z R_w^2} = \frac{ceN}{\pi B_z L_p R_w^2} \tag{B.6}$$

where we have neglected the finite-length correction terms. In practice, there are several corrections to Eq. (B.6) that account for finite-length effects as well as a nonlinear shift to the mode frequency when the amplitude of the mode, D, is large as given by Eq. (2.41) [60, 59]. The nonlinear correction term is mitigated by exciting a low amplitude Diocotron mode, $D/R_w \approx 0.01$, such that the nonlinear shift is small and therefore negligible. Furthermore, we perform the η calibration on a large aspect ratio plasma, $R_w/L_p \ll 1$, that has cooled to the wall temperature due to cyclotron radiation. In this scenario the finite-length corrections are a 10% modification to

Eq (B.6) and the finite-length corrections can be neglected for the purposes of the calibration of η.

When the finite-length effects are small, normalized changes in the length of the plasma are approximately proportional to normalized changes in the $m_\theta = 1$ Diocotron frequency as

$$\frac{\delta f_d}{f_d} \approx -\frac{\delta L_p}{L_p} \tag{B.7}$$

which gives a useful relationship between changes in the plasma length and changes in the $m_\theta = 1$ Diocotron frequency. Usage of the $m_\theta = 1$ Diocotron frequency to determine length changes is shown in Fig. B.2 where the eject electrode potential is oscillated using Eq. (B.3) but the inject electrode is held at $V_c = -100$ V. Since only one of the confinement electrodes is oscillated we are guaranteed that the length of the plasma is changing which is observed as a subsequent oscillation in the $m_\theta = 1$ Diocotron frequency.

Referring to Fig. B.2, at $t = 0$ we inject the plasma into the confinement region and we excite a low amplitude Diocotron mode using one of the sectors of electrode 4. The $m_\theta = 1$ Diocotron mode induces a voltage on the other sectors of electrode 4 and we select one of those sectors where we amplify and digitize the voltage signal. We then perform a Fourier transform to the signal to determine the temporal evolution of the mode frequency. Initially, the injected plasma has a temperature of $T \approx 2$ eV but the plasma eventually cools down to the wall temperature due to cyclotron radiation. The cooling is reflected in the exponential decrease in the $m_\theta = 1$ Diocotron frequency between $t = 0$ and $t = 10$ s in Fig. B.2. At $t = 20$ s we oscillate the potential of the eject electrode using the waveform given by Eq. (B.3) with two full cycles at $V_{sl} = 30$ V, $f_{sl} = 0.5$ Hz and $\eta = 0.47$; the inject electrode is held fixed at $V_c = -100$ V and no squeeze potential is applied. The modulation of the plasma length results in a modulation of N_L which in turn results in a modulation of the measured $m_\theta = 1$ Diocotron frequency as seen in Fig. B.2.

Calibrating the values of η for different V_{sl} involves applying the potential oscillations to both the inject and eject electrodes and then varying the value of η until the change in $m_\theta = 1$

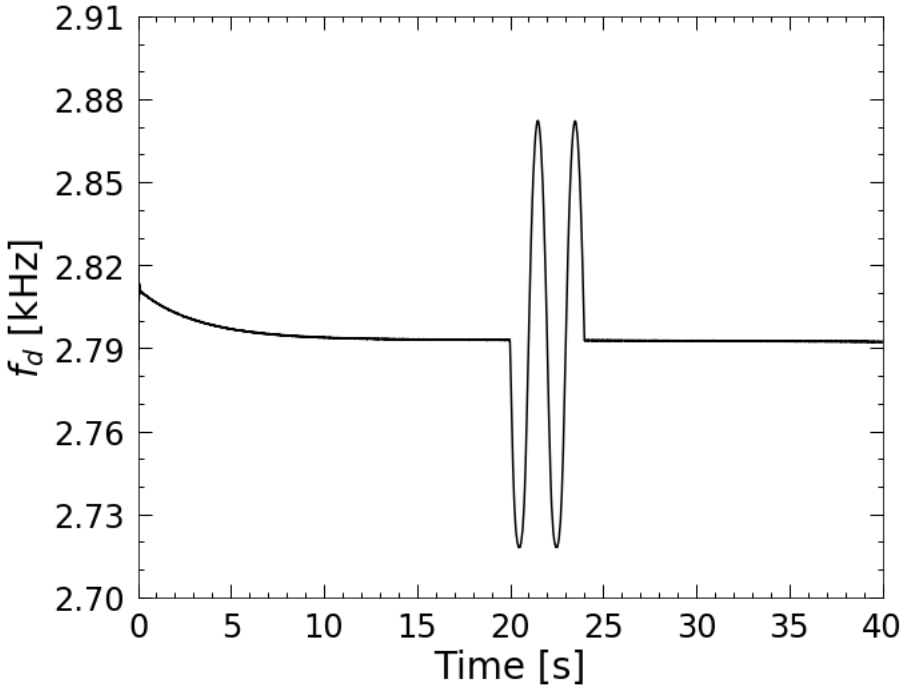

Figure B.2: Time evolution of $m_\theta = 1$ Diocotron Frequency, f_d. At $t = 0$ the plasma is injected into the trap and a low amplitude, $D/R_w \approx 0.01$, $m_\theta = 1$ Diocotron mode is excited. At $t = 20$ seconds we oscillate the voltage on one of the confinement electrodes with two cycles at $f_{sl} = 0.5$ Hz with amplitude $V_{sl} = 30$ V. The modulation of the confinement potential results in the compression and expansion of the plasma which appears as an increase or decrease in f_d due to the change in line density.

Table B.1: Calibration coefficient for separatrix-crossing dissipation.

Slosh Voltage V_{sl} $[V]$	η $[-]$
2.5	0.01
5	0.05
7.5	0.10
10	0.14
12.5	0.17
15	0.20
20	0.30
25	0.38
30	0.47
35	0.635
40	0.74

Diocotron frequency is minimized. Table (B.1) lists the value of η for a range of V_{sl} values where η was calibrated using measurements of the $m_\theta = 1$ Diocotron frequency as discussed in this Appendix.

Appendix C

Symbols and Notations

This appendix lists symbols and notations used in this dissertation. All equations use cgs units with temperature in energy units.

********** **Fundamental Quantities** **********

(r,θ,z)		Cylindrical coordinate system centered on the trap axis
e		Elementary charge
q		Signed charge. $q=-e$ for electrons and $q=e$ for singly ionized ions
m_e		Electron mass
c		Speed of light in vacuum
$\boldsymbol{B}$	$B_z\hat{\boldsymbol{z}}$	Axial magnetic field
B_x, B_y		Perpendicular alignment fields
ϕ		Total electrostatic potential
ϕ_c		Confinement potential
ϕ_p		Plasma potential
$\boldsymbol{E}$	$-\nabla\phi$	Electric field
E_r		Radial component of the electric field
T_w	0.03 eV	Wall temperature
$T_\parallel$		Parallel plasma temperature
$T_\perp$		Perpendicular plasma temperature
T	$\frac{1}{3}T_\parallel+\frac{2}{3}T_\perp$	Plasma temperature
T_{CP}		$r=0$ Temperature measured using the collector plate
$T'(r,V_H)$	Eq. (3.6)	Temperature after adiabatic expansion

********** Density and Particle Number **********

$Q_2(r,\theta,z)$	Eq. (2.2)	z-integrated density
$Q(r)$	Eq. (2.3)	θ-averaged z-integrated density
$Q_{exp}(r,V_H)$		θ-averaged z-integrated density measured at each V_H
$Q_{mod}(r,V_H,T)$		Model predicted θ-averaged z-integrated density at each V_H
$n(r,\theta,z)$		3-dimensional plasma density
$n(r,z)$		θ-averaged density
$n_p(r)$	$Q(r)/L_p(r)$	(θ,z)-averaged density
$n_c(r)$	$Q(r)/L_p^*$	Approximation for (θ,z)-averaged density
$n_{tr}(r,z,V_H,T)$		Trapped particle density
$n_{esc}(r,z,V_H,T)$		Escaping particle density
N	Eq. (2.4)	Total number of particles
N_{esc}		Number of escaping electrons
N_L	N/L_p^*	Line density

********** Lengths **********

ρ		Collision impact parameter
b	e^2/T	Distance of closest approach
r_c	$\bar{v}/2\pi f_c$	Cyclotron radius
r_{ci}, r_{ce}		Ion and electron cyclotron radii (neutral plasma)
λ_D, λ_{De}	$\sqrt{T/4\pi ne^2}$	Debye length
R_w	3.5 cm	Wall radius
D		$m = 1$ Diocotron mode amplitude
$\langle r^2 \rangle$	Eq. (2.10)	Mean-square radius
R_p	$\sqrt{2\langle r^2 \rangle}$	Plasma radius
L_c		Confinement length
L_p	Eq. (2.12)	Plasma length calculated using density weighted average
L_p^*	$L_c - 4.5$ cm	Plasma length estimate

********** Rates and Times **********

ν_c	$n\bar{v}b^2$	Classical collision rate
f_c	$eB_z/2\pi m_e c$	Cyclotron frequency
ω_p	$\sqrt{4\pi ne^2/m_e}$	Plasma frequency
f_b	$\bar{v}/2L_p$	Axial bounce frequency
f_E	$-cE_r/2\pi rB_z$	$E \times B$ drift rotation frequency
ν_{ee}	Eq. (2.15)	Electron-electron collision rate
$\nu_{\perp\parallel}$	Eq. (2.17)	Perpendicular-to-parallel relaxation rate.
$\nu_{\langle r^2\rangle}$	Eq. (2.25)	Expansion rate
f_m	Eq. (2.40)	Infinite-length Diocotron mode frequency with mode number m
f_d	Eq. (2.41)	Finite-length $m = 1$ Diocotron mode frequency
f_{sl}		Slosh frequency for separatrix-crossing dissipation
t_c		Confinement time
τ_r	Eq. (2.19)	Cyclotron radiation time
τ_b	$1/f_b$	Axial bounce period
τ_E	$1/f_E$	$E \times B$ drift rotation period
τ_L	L_T^2/χ_L	Time scale for long-range diffusive heat transport
τ_C	L_T^2/χ_C	Time scale for short-range diffusive heat transport
τ_{RC}		RC circuit time constant
t_{sl}		Slosh duration for separatrix-crossing dissipation

Note that $\omega = 2\pi f$ for all frequencies

********** Energies, Momenta and Velocities **********

(v_r, v_θ, v_z)		Velocities in cylindrical coordinates
v_{z0}		Maximum axial velocity
P_θ	$\approx -(eB_z/2c)\langle r^2\rangle$	Canonical angular momentum
$p_\perp$	$m_e v_\perp$	Perpendicular angular momentum
p_θ	$m_e v_\theta r$	Azimuthal angular momentum
p_z	$m_e v_z$	Axial particle momentum
$\bar{v}$	$\sqrt{T/m_e}$	Thermal velocity
$v_\perp$		Perpendicular velocity
$E_\parallel$	$(1/2)m_e v_z^2$	Parallel kinetic energy
E_c		Confinement energy
H_T	Eq. (4.3)	Average thermal energy per particle
H_ϕ	Eq. (4.2)	Average electrostatic energy per particle
H_{Tot}	$H_T + H_\phi$	Average energy per particle

********** Transport Quantities **********

q_s		Sources and sinks of thermal energy
q_j	Eq. (5.11)	Joule heating rate
q_r	Eq. (5.12)	Cyclotron cooling rate
L_T	≈ 0.5 cm	Thermal gradient length scale
Γ_m	Eq. (5.9)	Particle flux
Γ_χ	Eqs. (5.7), (5.8)	Diffusive heat flux
χ		Measured thermal diffusivity
χ_C	Eq. (5.1)	Classical short-range thermal diffusivity
χ_L	Eq. (5.2)	Long-range thermal diffusivity
κ	$(5/2)n\chi$	Thermal conductivity
$\boldsymbol{j}$		Current density

********** **Miscellaneous** **********

$\mathcal{R}$	f_b/f_E	Plasma rigidity
J	$\oint p_z dz$	Axial bounce adiabatic invariant
μ'		Cyclotron adiabatic invariant
μ		Electron magnetic moment
Φ		Drift-orbit adiabatic invariant
σ	Eq. (2.42)	Geometric factor characterizing the nonlinear shift of f_d
P_{bg}		Pressure of background gas
α		T_{CP} temperature measurement correction factor
ζ		Eject voltage ramp rate
ε		Ratio of plasma lengths
V_c	-100 V	Confinement voltage
V_{ej}		Eject electrode voltage
V_H		Hold voltage for temperature measurements
V_{trim}	$V_H - 3$ V	Trim voltage when ramping to V_H
V_A		Acceleration voltage
V_b		Filament bias voltage
V_f		Filament AC voltage
I_f		Filament AC current
R_f		Outer radius of filament
V_{sl}		Slosh voltage for separatrix-crossing dissipation
V_{sq}		Squeeze voltage for separatrix-crossing dissipation
R		Resistor in collector plate measurement circuit
C		Capacitor in collector plate measurement circuit
C_b		Blocking capacitor
z_{max}		Axial location of the peak confinement barrier from the eject electrode
z_{mid}		Axial midpoint between the inject and eject electrodes
J_0, J_1		Bessel Function of the first kind
j_{0i}	$j_{01} = 2.405$	ith Bessel root of J_0.

Bibliography

[1] D. D. Needelman and R. L. Stenzel. Cross-field electron thermal conductivity in an electron-beam plasma system. *Physical Review Letters*, 58(14):1426–1429, apr 1987.

[2] S. I. Braginskii. Transport Processes in a Plasma. *RvPP*, 1:205, 1965.

[3] F. L. Hinton and R. D. Hazeltine. Theory of plasma transport in toroidal confinement systems. *Reviews of Modern Physics*, 48(2):239–308, apr 1976.

[4] Steven A. Balbus and John F. Hawley. Instability, turbulence, and enhanced transport in accretion disks. *Reviews of Modern Physics*, 70(1):1–53, jan 1998.

[5] J. D. Callen. Transport processes in magnetically confined plasmas. *Physics of Fluids B*, 4(7):2142–2154, mar 1992.

[6] J. D. Callen. Most electron heat transport is not anomalous; It is a paleoclassical process in toroidal plasmas. *Physical Review Letters*, 94(5):055002, feb 2005.

[7] J. P. Matte and J. Virmont. Electron heat transport down steep temperature gradients. *Physical Review Letters*, 49(26):1936–1939, dec 1982.

[8] A. B. Rechester and M. N. Rosenbluth. Electron heat transport in a tokamak with destroyed magnetic surfaces. *Physical Review Letters*, 40(1):38–41, jan 1978.

[9] Z. Lin, T. S. Hahm, W. W. Lee, W. M. Tang, and P. H. Diamond. Effects of collisional zonal flow damping on turbulent transport. *Physical Review Letters*, 83(18):3645–3648, jan 1999.

[10] C. F. Driscoll, J. H. Malmberg, and K. S. Fine. Observation of transport to thermal equilibrium in pure electron plasmas. *Physical Review Letters*, 60(13):1290–1293, mar 1988.

[11] J. S. DeGrassie and J. H. Malmberg. Waves and transport in the pure electron plasma. *Physics of Fluids*, 23(1):63–81, 1980.

[12] J. H. Malmberg and C. F. Driscoll. Long-time containment of a pure electron plasma. *Physical Review Letters*, 44(10):654–657, mar 1980.

[13] C. F. Driscoll and J. H. Malmberg. Length-dependent containment of a pure electron-plasma column. *Physical Review Letters*, 50(3):167–170, jan 1983.

[14] C. F. Driscoll, K. S. Fine, and J. H. Malmberg. Reduction of radial losses in a pure electron plasma. *Physics of Fluids*, 29(6):2015, sep 1986.

[15] C. F. Driscoll, F. Anderegg, D. H.E. Dubin, D. Z. Jin, J. M. Kriesel, E. M. Hollmann, and T. M. O'Neil. Shear reduction of collisional transport: Experiments and theory. In *Physics of Plasmas*, volume 9, pages 1905–1914. American Institute of Physics, may 2002.

[16] C. L. Longmire and M. N. Rosenbluth. Diffusion of charged particles across a magnetic field. *Physical Review*, 103(3):507–510, aug 1956.

[17] M. N. Rosenbluth and A. N. Kaufman. Plasma diffusion in a Magnetic Field. *Physical Review*, 109(1):1–5, jan 1958.

[18] Albert Simon. Diffusion of like particles across a magnetic field. *Physical Review*, 100(6):1557–1559, dec 1955.

[19] E. M. Lifshitz and L. P. Pitaevskii. *Physical Kinetics*. Elsevier, Oxford, 1981.

[20] T. M. O'Neil. New theory of transport due to like-particle collisions. *Physical Review Letters*, 55(9):943–946, aug 1985.

[21] Marshall N. Rosenbluth and C. S. Liu. Cross-field energy transport by plasma waves. *Physics of Fluids*, 19(6):815–818, aug 1976.

[22] Daniel H.E. Dubin. Test Particle Diffusion and the Failure of Integration along Unperturbed Orbits. *Physical Review Letters*, 79(14):2678–2681, oct 1997.

[23] D. H.E. Dubin and T. M. O'Neil. Two-dimensional guiding-center transport of a pure electron plasma. *Physical Review Letters*, 60(13):1286–1289, mar 1988.

[24] D. H.E. Dubin and T. M. O'Neil. Cross-magnetic-field heat conduction in non-neutral plasmas. *Physical Review Letters*, 78(20):3868–3871, may 1997.

[25] F. Anderegg, X. P. Huang, C. F. Driscoll, E. M. Hollmann, T. M. O'neil, and D. H.E. Dubin. Test particle transport due to long range interactions. *Physical Review Letters*, 78(11):2128–2131, mar 1997.

[26] E. M. Hollmann, F. Anderegg, and C. F. Driscoll. Measurement of cross-magnetic-field heat transport in a pure ion plasma. *Physical Review Letters*, 82(24):4839–4842, jun 1999.

[27] E. M. Hollmann, F. Anderegg, and C. F. Driscoll. Measurement of cross-magnetic-field heat transport due to long-range collisions. *Physics of Plasmas*, 7(5):1767–1773, may 2000.

[28] Daniel H.E. Dubin and Dezhe Z. Jin. Collisional diffusion in a 2-dimensional point vortex gas. *Physics Letters, Section A: General, Atomic and Solid State Physics*, 284(2-3):112–117, jun 2001.

[29] Daniel H.E. Dubin and T. M. O'Neil. Two-dimensional bounce-averaged collisional particle transport in a single species non-neutral plasma. *Physics of Plasmas*, 5(5 PART 1):1305–1314, may 1998.

[30] Francois Anderegg. Shear-limited test particle diffusion in 2-dimensional plasmas. In *AIP Conference Proceedings*, volume 606, pages 401–406. AIP Publishing, feb 2002.

[31] J. M. Kriesel and C. F. Driscoll. Measurements of viscosity in pure-electron plasmas. *Physical Review Letters*, 87(13):135003/1–135003/4, sep 2001.

[32] F. Anderegg, X. P. Huang, E. Sarid, and C. F. Driscoll. A new pure ion plasma device with laser induced fluorescence diagnostic. *Review of Scientific Instruments*, 68(6):2367–2377, jun 1997.

[33] T. M. O'Neil. A confinement theorem for nonneutral plasmas. *Physics of Fluids*, 23(11):2216–2218, jul 1980.

[34] J. R. Danielson, F. Anderegg, and C. F. Driscoll. Measurement of Landau damping and the evolution to a BGK equilibrium. *Physical Review Letters*, 92(24):245003, jun 2004.

[35] F. Anderegg, C. F. Driscoll, D. H.E. Dubin, and T. M. O'Neil. Wave-particle interactions in electron acoustic waves in pure ion plasmas. *Physical Review Letters*, 102(9):095001, mar 2009.

[36] D. Durkin and J. Fajans. Experimental dynamics of a vortex within a vortex. *Physical Review Letters*, 85(19):4052–4055, nov 2000.

[37] K. S. Fine, C. F. Driscoll, J. H. Malmberg, and T. B. Mitchell. Measurements of symmetric vortex merger. *Physical Review Letters*, 67(5):588–591, jul 1991.

[38] N. C. Hurst, J. R. Danielson, D. H.E. Dubin, and C. M. Surko. Evolution of a Vortex in a Strain Flow. *Physical Review Letters*, 117(23):235001, dec 2016.

[39] J. R. Danielson, D. H.E. Dubin, R. G. Greaves, and C. M. Surko. Plasma and trap-based techniques for science with positrons. *Reviews of Modern Physics*, 87(1):247–306, mar 2015.

[40] M. Ahmadi, B. X.R. Alves, C. J. Baker, W. Bertsche, A. Capra, C. Carruth, C. L. Cesar, M. Charlton, S. Cohen, R. Collister, S. Eriksson, A. Evans, N. Evetts, J. Fajans, T. Friesen, M. C. Fujiwara, D. R. Gill, P. Granum, J. S. Hangst, W. N. Hardy, M. E. Hayden, E. D. Hunter, C. A. Isaac, M. A. Johnson, J. M. Jones, S. A. Jones, S. Jonsell, A. Khramov, P. Knapp, L. Kurchaninov, N. Madsen, D. Maxwell, J. T.K. McKenna, S. Menary, J. M. Michan, T. Momose, J. J. Munich, K. Olchanski, A. Olin, P. Pusa, C. Rasmussen, F. Robicheaux, R. L. Sacramento, M. Sameed, E. Sarid, D. M. Silveira, C. So, D. M. Starko, G. Stutter, T. D. Tharp, R. I. Thompson, D. P. van der Werf, and J. S. Wurtele. Investigation of the fine structure of antihydrogen. *Nature*, 578(7795):375–380, feb 2020.

[41] J. M. Kriesel and C. F. Driscoll. Electron plasma profiles from a cathode with an r2 potential variation. *Physics of Plasmas*, 5(5):1265–1272, may 1998.

[42] B. R. Beck. *Measurement of the Magnetic and Temperature Dependence of the Electron-Electron Anisotropic Temperature Relaxation Rate*. PhD thesis, University of California San Diego, 1990.

[43] R. H. Levy. Two new results in cylindrical diocotron theory. *Physics of Fluids*, 11(4):920–921, 1968.

[44] S. A. Prasad and T. M. O'Neil. Waves in a cold pure electron plasma of finite length. *Physics of Fluids*, 26(3):665–672, jun 1983.

[45] S. A. Prasad and T. M. O'Neil. Vlasov theory of electrostatic modes in a finite length electron column. *Physics of Fluids*, 27(1):206–213, jun 1984.

[46] A. W. Trivelpiece and R. W. Gould. Space charge waves in cylindrical plasma columns. *Journal of Applied Physics*, 30(11):1784–1793, 1959.

[47] A. J. Peurrung and J. Fajans. Three-dimensional non-neutral plasma shapes. *Physics of Fluids B*, 5(11):4250–4252, nov 1993.

[48] David Montgomery, Glenn Joyce, and Leaf Turner. Magnetic field dependence of plasma relaxation times. *Physics of Fluids*, 17(12):2201–2204, aug 1974.

[49] A. W. Hyatt, C. F. Driscoll, and J. H. Malmberg. Measurement of the Anisotropic Temperature Relaxation Rate in a Pure Electron Plasma. *Physical Review Letters*, 59(26):2975–2978, dec 1987.

[50] B. R. Beck, J. Fajans, and J. H. Malmberg. Measurement of collisional anisotropic temperature relaxation in a strongly magnetized pure electron plasma. *Physical Review Letters*, 68(3):317–320, jan 1992.

[51] T. M. O'Neil. Cooling of a pure electron plasma by cyclotron radiation. *Physics of Fluids*, 23(4):725–731, jul 1980.

[52] B. R. Beck, J. Fajans, and J. H. Malmberg. Temperature and anisotropic-temperature relaxation measurements in cold, pure-electron plasmas. *Physics of Plasmas*, 3(4):1250–1258, apr 1996.

[53] J. M. Kriesel and C. F. Driscoll. Two regimes of asymmetry-induced transport in non-neutral plasmas. *Physical Review Letters*, 85(12):2510–2513, sep 2000.

[54] J. M. Kriesel. *Experiments on Viscous and Asymmetry-Induced Transport in Magnetized, Pure-Electron Plasmas*. PhD thesis, University of California San Diego, 1999.

[55] D. L. Eggleston, C. F. Driscoll, B. R. Beck, A. W. Hyatt, and J. H. Malmberg. Parallel energy analyzer for pure electron plasma devices. *Physics of Fluids B*, 4(10):3432–3439, 1992.

[56] L. D. Landau and E. M. Lifshitz. *Mechanics*. Elsevier, Oxford, 3rd edition, 1976.

[57] R. C. Davidson. *Physics of Nonneutral Plasmas*. World Scientific Publishing Co. Pte. Ltd., Singapore, 2001.

[58] K. S. Fine. *Experiments with the l=1 Diocotron Mode*. PhD thesis, University of California San Diego, 1988.

[59] K. S. Fine. Simple theory of a nonlinear diocotron mode. *Physics of Fluids B*, 4(12):3981–3984, dec 1992.

[60] K. S. Fine and C. F. Driscoll. The finite length diocotron mode. *Physics of Plasmas*, 5(3):601–607, mar 1998.

[61] Thomas M. O'Neil. Criterion for the sign of wave energy. *Physics of Plasmas*, 26(10):102106, oct 2019.

[62] W. D. White, J. H. Malmberg, and C. F. Driscoll. Resistive-wall destabilization of diocotron waves. *Physical Review Letters*, 49(25):1822–1826, dec 1982.

[63] Grant W. Hart and Bryan G. Peterson. Finding the radial parallel temperature profile in a non-neutral plasma using equilibrium calculations on experimental data. *Physics of Plasmas*, 13(2):022101, feb 2006.

[64] J. Aoki, Y. Kiwamoto, and Y. Kawai. Determination of equilibrium density distribution and temperature of a pure electron plasma confined in a Penning trap. *Physics of Plasmas*, 13(11):112109, nov 2006.

[65] L. R. Brewer, J. D. Prestage, J. J. Bollinger, Wayne M. Itano, D. J. Larson, and D. J. Wineland. Static properties of a non-neutral 9Be+-ion plasma. *Physical Review A*, 38(2):859–873, jul 1988.

[66] M R Natisin, J R Danielson, and C M Surko. Positron cooling by vibrational and rotational excitation of molecular gases. *Journal of Physics B: Atomic, Molecular and Optical Physics*, 47(22):225209, nov 2014.

[67] G. Maero, R. Pozzoli, M. Romé, S. Chen, and M. Ikram. Axial heating and temperature of RF-excited non-neutral plasmas in Penning-Malmberg traps. *Journal of Instrumentation*, 11(09):C09007–C09007, sep 2016.

[68] Yukihiro Soga, Tetsuya Mimura, Yasutada Kato, and Youngsoo Park. Mechanisms of E $\times$ B Drift Rotation of a Vortex String in a Pure Electron Plasma. *Plasma and Fusion Research*, 8(0):2401034–2401034, apr 2013.

[69] G. B. Andresen, M. D. Ashkezari, M. Baquero-Ruiz, W. Bertsche, P. D. Bowe, E. Butler, C. L. Cesar, S. Chapman, M. Charlton, J. Fajans, T. Friesen, M. C. Fujiwara, D. R. Gill, J. S. Hangst, W. N. Hardy, R. S. Hayano, M. E. Hayden, A. Humphries, R. Hydomako, S. Jonsell, L. Kurchaninov, R. Lambo, N. Madsen, S. Menary, P. Nolan, K. Olchanski, A. Olin, A. Povilus, P. Pusa, F. Robicheaux, E. Sarid, D. M. Silveira, C. So, J. W. Storey, R. I. Thompson, D. P. Van Der Werf, D. Wilding, J. S. Wurtele, and Y. Yamazaki. Evaporative cooling of antiprotons to cryogenic temperatures. *Physical Review Letters*, 105(1):013003, jul 2010.

[70] G. Gabrielse, W. S. Kolthammer, R. McConnell, P. Richerme, R. Kalra, E. Novitski, D. Grzonka, W. Oelert, T. Sefzick, M. Zielinski, D. Fitzakerley, M. C. George, E. A. Hessels, C. H. Storry, M. Weel, A. Müllers, and J. Walz. Adiabatic cooling of antiprotons. *Physical Review Letters*, 106(7):073002, feb 2011.

[71] A. W. Hyatt. *Measurement of the Anisotrophic Temperature Relaxation Rate in a Magnetized Pure Electron Plasma*. PhD thesis, University of California San Diego, 1988.

[72] C. F. Driscoll. Observation of an unstable l=1 diocotron mode on a hollow electron column. *Physical Review Letters*, 64(6):645–648, feb 1990.

[73] J. R. Danielson. *Measurement of Landau Damping of Electron Plasma Waves in the Linear and Trapping Regimes*. PhD thesis, University of California San Diego, 2002.

[74] Daniel H.E. Dubin and T. M. O'Neil. Trapped nonneutral plasmas, liquids, and crystals (the thermal equilibrium states). *Reviews of Modern Physics*, 71(1):87–172, jan 1999.

[75] B. P. Cluggish and C. F. Driscoll. Transport and damping from rotational pumping in magnetized electron plasmas. *Physical Review Letters*, 74(21):4213–4216, may 1995.

[76] Ira B. Bernstein, John M. Greene, and Martin D. Kruskal. Exact nonlinear plasma oscillations. *Physical Review*, 108(3):546–550, nov 1957.

[77] A. A. Kabantsev, Daniel H.E. Dubin, C. F. Driscoll, and Yu A. Tsidulko. Chaotic transport and damping from θ-ruffled separatrices. *Physical Review Letters*, 105(20):205001, nov 2010.

[78] Daniel H.E. Dubin, A. A. Kabantsev, and C. F. Driscoll. Enhanced superbanana transport caused by chaotic scattering across an asymmetric separatrix. *Physics of Plasmas*, 19(5):056102, may 2012.

[79] A. A. Kabantsev, C. F. Driscoll, T. J. Hilsabeck, T. M. O'Neil, and J. H. Yu. Trapped-particle asymmetry modes in single-species plasmas. *Physical Review Letters*, 87(22):225002/1–225002/4, nov 2001.

[80] T. J. Hilsabeck, A. A. Kabantsev, C. F. Driscoll, and T. M. O'Neil. Damping of the trapped-particle diocotron mode. *Physical Review Letters*, 90(24):245002/1–245002/4, jun 2003.

[81] Daniel H.E. Dubin. Superbanana transport in the collisional heating of a plasma column forced across a squeeze potential. *Physics of Plasmas*, 24(11):112120, nov 2017.

[82] F. Anderegg, M. Affolter, D. H.E. Dubin, and C. F. Driscoll. Plasma Heating due to Cyclic Diffusion across a Separatrix. *Physical Review Letters*, 123(10):105002, sep 2019.

[83] L. D. Landau and E. M. Lifshitz. *Fluid Mechanics*. Elsevier, Oxford, 2nd editio edition, 1987.

[84] Leon Brillouin. A theorem of larmor and its importance for electrons in magnetic fields. *Physical Review*, 67(7-8):260–266, apr 1945.